1-1-1993

# Polymer concentration profiles and methods of surface modification/

Todd L. Mansfield
*University of Massachusetts Amherst*

# POLYMER CONCENTRATION PROFILES AND METHODS OF SURFACE MODIFICATION

A Dissertation Presented

by

TODD L. MANSFIELD

Submitted to the Graduate School of the
University of Massachusetts in partial fulfillment
of the requirements for the degree of

DOCTOR OF PHILOSOPHY

September 1993

Polymer Science and Engineering Department

# POLYMER CONCENTRATION PROFILES AND METHODS OF SURFACE MODIFICATION

A Dissertation Presented
by
TODD L. MANSFIELD

Approved as to style and content by:

Richard S. Stein, Chair

William J. MacKnight, Member

Scott W. Barton, Member

Russell J. Composto, Member

Paul D. Garrett, Member

William J. MacKnight, Department Head
Polymer Science and Engineering Department

To my parents, for always giving me love, opportunities and encouragement.

# ACKNOWLEDGEMENTS

The author wishes to thank Dr. Kenneth Shull for assistance with FReS measurements on selected polystyrene samples, and Dr. Barry Wilkins for assistance with DSIMS measurements on selected SAN copolymer blends. The author has also benefitted from discussions with the members of his dissertation committee, as well as Dr. John Ankner, Dr. C.F. Majkrzak, Dr. Sushil Satija, Dr. Miriam Rafailovich, and Dr. Jon Sokolov. Figure 1.3 was reproduced with the permission of Prof. Jakob Klein.

ABSTRACT

POLYMER CONCENTRATION PROFILES AND METHODS OF SURFACE MODIFICATION

SEPTEMBER 1993

TODD L. MANSFIELD, B.S., UNIVERSITY OF UTAH

Ph.D., UNIVERSITY OF MASSACHUSETTS AMHERST

Directed by: Professor Richard S. Stein

The behavior of miscible polymer mixtures at surfaces depends to a large extent on the thermodynamics of mixing in the bulk. The relative importance of bulk and surface interactions has been investigated for polymer blends and solutions using neutron reflection. Segregation in miscible blends of SAN copolymers is driven by surface tension differences between the two components, which arise from AN content differences. The extent of demixing at the surface is found to depend strongly on the Flory-Huggins interaction parameter, $\chi$. For dilute solutions of terminally carboxylated polystyrenes in contact with an $SiO_2$ wall, polymer adsorption is dominated by the $SiO_2$/COOH interaction. Even under these "strong wall" conditions, the extent of adsorption is found to be sensitive to $\chi$.

TABLE OF CONTENTS

# LIST OF TABLES

# LIST OF FIGURES

# CHAPTER 1

# MEASUREMENT OF CONCENTRATION PROFILES

The unifying theme of this dissertation is the behavior of binary miscible mixtures in the presence of perturbing objects, i.e. surfaces or interfaces. This dissertation discusses two problems: terminally-functionalized polymers at the solution/solid interface and binary miscible polymer blends near interfaces. The common theme underlying these problems is that the state of demixing of two miscible components near a surface depends strongly on the thermodynamics of mixing in the bulk.

## 1.1 Polymer Segregation and Adsorption: Physical Phenomena

While driving forces toward demixing, such as surface tension, or special interactions with the surface are specific to the polymer/wall pair, the ultimate extent of segregation or adsorption is profoundly influenced by the thermodynamics of the bulk, and is therefore characterized by conventional molecular parameters including the degree of polymerization and the bulk interaction parameter $\chi$.

Pandit and coworkers published a systematic classification of adsorption (or segregation, as we shall call it in this dissertation) phenomena near "attractive" substrates developed from a picture of a gas in contact with a wall,[1] as shown schematically in Figure 1.1.

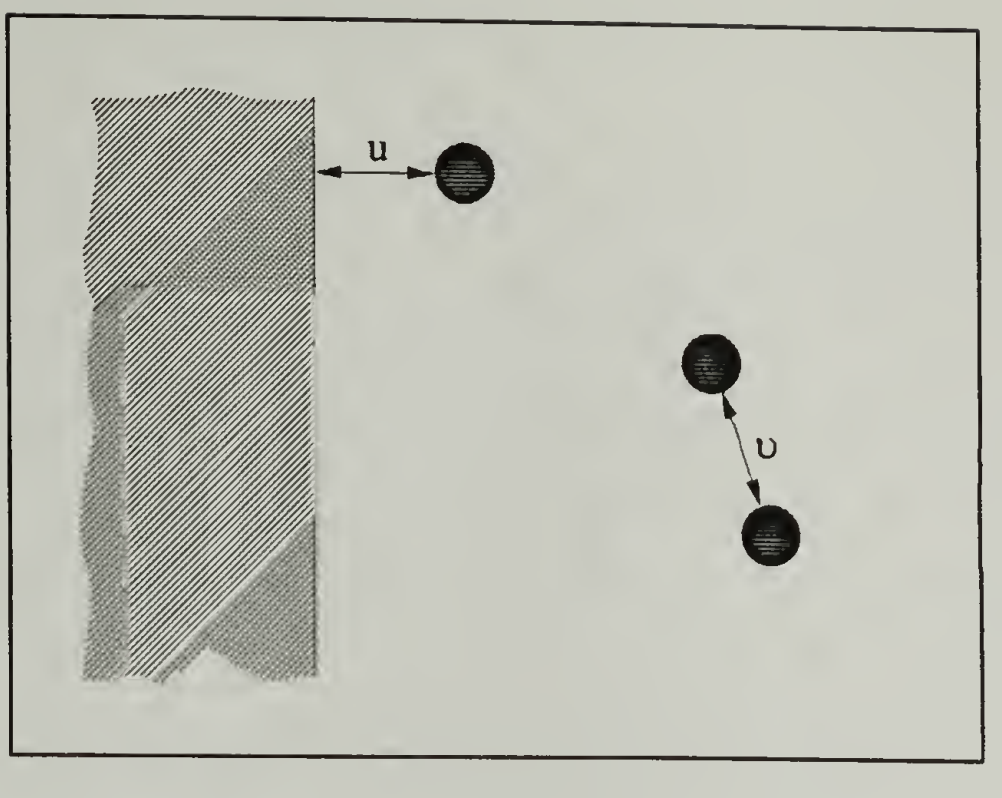


Figure 1.1 Schematic diagram of a gas in contact with a wall. The gas/wall and gas/gas interaction energies are characterized by the parameters u and υ respectively.

The case of interest is when attractive forces exist between the gas molecules and the wall *and* between the gas molecules mutually. These forces are characterized by the parameters u and υ respectively, with negative values of u and υ corresponding to attractive forces. In understanding the surface segregation of the gas at the wall, it is worthwhile to first consider a collection of molecules far away from walls.

Here, under conditions of $\upsilon < \upsilon_c$, the mutual attraction between gas molecules causes the formation of a condensed phase. For $\upsilon_c < \upsilon < 0$ the tendency toward condensation is overcome by the thermal energy of the gas molecules. This is analogous to a symmetric polymer blend when $\chi > 0$ or to a polymer solution having $\chi > 0.5$, where increasing $\chi$ produces the same qualitiative effect as decreasing υ. For these polymer mixtures, the analog of condensed phase formation is the demixing of the two components into phases having distinctly differing compositions at $\chi = \chi_c$. In this dissertation, most of the discussion will be limited to polymer mixtures where $\chi < \chi_c$.

In considering the role of interactions at the surface in adsorption and segregation at surfaces, it is often useful to compare the quantity $\frac{u}{\upsilon}$ with unity to understand the role of the bulk interactions in the surface behavior of the gas. When $\frac{u}{\upsilon} >> 1$ (strong substrate) segregation is driven primarily by the interactions between the gas molecules and the wall. When $\frac{u}{\upsilon} << 1$ (weak substrate) segregation is driven primarily by the mutual interactions between the gas molecules. Under these conditions, the bulk thermodynamics are the primary determinant of the adsorption behavior of the gas. By analogy, the same is true for polymers. The form of the adsorbed layer is often dictated by the by the binary interactions in the bulk.

## 1.2 Motivation and Applications to Polymer Engineering

The study of polymer-polymer interfaces is being pursued for both theoretical and practical reasons. As in other areas of polymer science, many theories of polymer interfaces preceeded the development of experimental techniques with sufficient sensitivity and resolution to test theoretical predictions. For example, although Helfand and Tagami calculated[2] the interfacial profile between two immiscible polymers in 1971, rigorous experimental support did not appear until the recent application of neutron reflection to polymer interface problems. The characterization of the polymer-polymer interface also has technological interest in areas such as impact modification, welding, crack healing, injection molding, and other polymer adhesion problems. As a particular example, accurate data on the diffusion coefficients helps the technologist calculate the optimum process conditions, e.g. temperature and time, for the friction welding of automobile parts.

One particularly dramatic example of the importance of polymer interfaces is their effect on the mechanical properties of immiscible polymer blends. Fayt and Teyssie[3] have shown that the locus of failure of blends of high-density polyethylene (HDPE) and polystyrene (PS) is largely confined to the interfacial regions. They also show that the addition of a small amount of styrene/HDPE diblock copolymer greatly increases the fracture toughness as well as modifies the locus of failure. Thus, a fundamental understanding of the fracture energy of this blend demands a precise characterization of the molecular interpenetration across the HDPE/PS interface. Characterization of the amount and location of the copolymer at the interface is necessary if we are to understand how the copolymer anchors the HDPE and PS phases together.

An example of the role of polymers in surface modification is the stabilization of colloids, an important aspect of such diverse industrial applications as paints and coatings, as well as the processing of such diverse products as ceramics and foods. The goal of this and the following sections is to summarize some of the current techniques and experiments, providing a perspective for the work in this dissertation. We shall do this by selecting several interface problems of current interest followed by examples of appropriate characterization technique(s).

## 1.3 Techniques for Measurement of Concentration Profiles in Polymer Melts

In choosing the appropriate technique, the main considerations are the spatial resolution required for the particular interface problem and contrast between polymers. In general, the higher resolution techniques are more complex (and costly) than lower resolution ones. For example, because neutron reflection experiments require high neutron fluxes, experiments must be performed at national laboratories such as Brookhaven, NIST, ANL, Oak Ridge, or LANSE. In this chapter, the depth resolution of the selected techniques range from 1 to 10000 Ångstroms. Because most polymers contain primarily

carbon and hydrogen, contrast between polymers may require labeling of chains by deuteration, staining or photochromic tagging. Although not always possible, labels should be chosen to maximize contrast while minimizing the perturbation of the system. In the best situations, contrast is inherent. For example, in blends of PS with deuterated PS (DPS), the deuteration of (some) chains provides not only contrast but slight chemical differences which can drive such phenomena as partial demixing near surfaces, or phase separation in the bulk, phenomena of considerable interest. Most of the techniques discussed require samples of planar geometry, where the volume fraction $\phi$ of the component of interest is a function of z only, as shown in Figure 1.2.

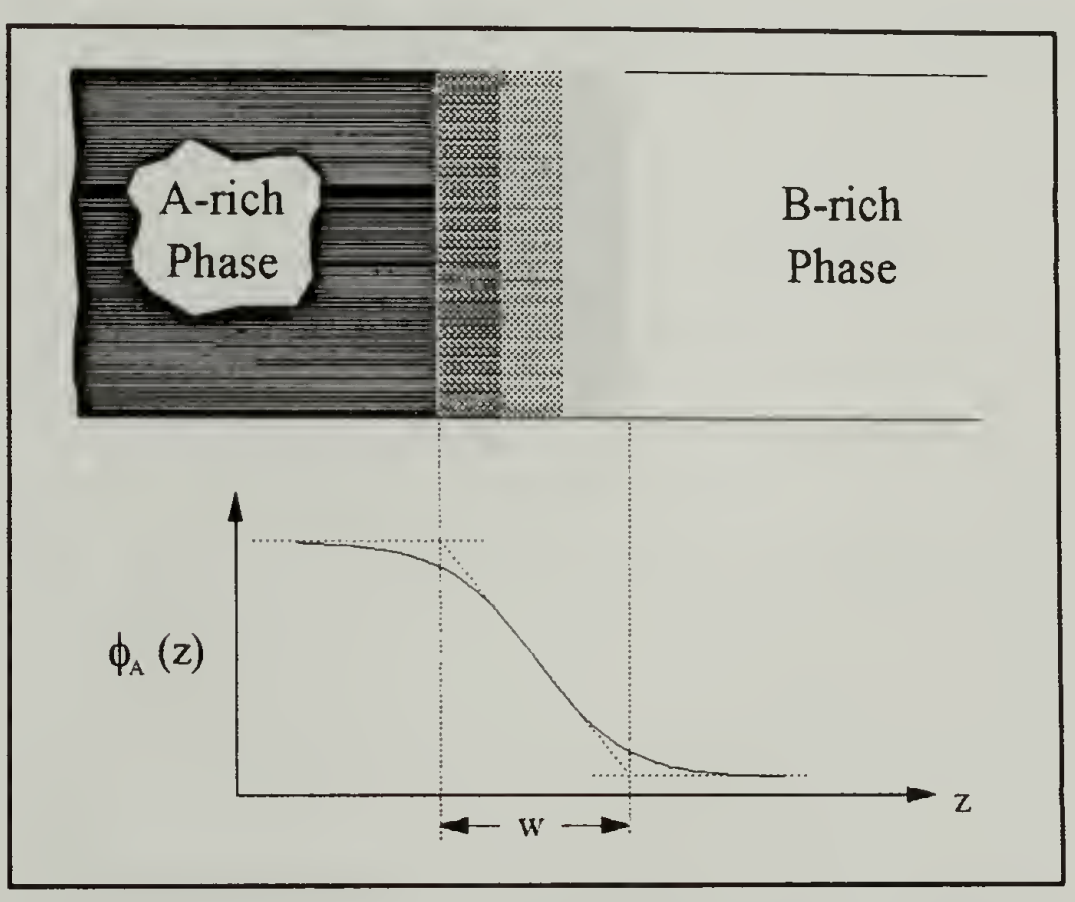


Figure 1.2 Schematic diagram of the planar geometry used most often for interfacial studies. A graphical definition of the interfacial width w between the coexisting phases is shown at the bottom.

The interfacial width w is the most relevant experimental size scale. If the schematic profile of Figure 1.2 is the interdiffusion profile of two miscible components, w is determined by the diffusion coefficient, and the diffusion temperature and time. If instead

the profile is the equilibrium interface between two immiscible polymers, w depends primarily on the interaction parameter $\chi$, according to $w \sim \chi^{-1/2}$.

The thickness of A and B depends on the spatial resolution and penetration depth of the technique. The lateral sample dimension depends on the probe and its footprint on the sample. Although consistent with many coating and microelectronics applications, the geometries of Figure 1.2 are not of obvious relevance to many three-dimensional problems (for example, the examination of fracture surfaces). While postmortem analysis of the fracture surface is possible, premortem characterization of the interfacial profile is needed to provide a molecular interpretation of the measured properties such as fracture energy. In most cases, the three-dimensional problem, such as in the HDPE/PS example, can be modeled by the planar geometry.

### 1.3.1 Techniques for Measuring Interdiffusion Distances Much Larger than the Molecular Size (w >>100 Å)

For a pair of semi-infinite solids separated by an interface, the volume fraction profile $\phi(x,t)$ of component A is given[4] by:

$$\phi_a(x,t) = \frac{\phi'}{2}\left[1 + \mathrm{erf}\left(\frac{x}{w}\right)\right] \qquad (1.1)$$

where $w = 2(Dt)^{1/2}$ is the characteristic diffusion distance, D is the mutual diffusion coefficient, and t is the annealing time. The mutual diffusion coefficient for polymer blends is given by:

$$D = \left[\phi_b D^*_a N_a + \phi_b D^*_b N_b\right] \Omega \qquad (1.2)$$

where $D^*_i$ and $N_i$ are the tracer diffusion coefficient and degree of polymerization of component i respectively, and $\Omega$ represents a thermodynamic driving force for diffusion. For systems with a negative excess free energy of mixing ($\Omega$ greater than 1), as is the case for blends of PS with poly(xylenyl ether)[5], D is increased relative to systems where the driving force is purely entropic. For systems like PS and deuterated PS, the excess free energy is small but positive and therefore diffusion is retarded[6,7].

The theory of polymer dynamics is an evolving and expansive topic. Although dated, Graessley's review of the dynamics of entangled systems is excellent[8]. More recently, Doi and Edwards[9] published a detailed account of the dynamical behavior of solids and solutions, and Kausch and Tirrell[10] published a review of diffusion in polymer blends. For long polymer chains, molecules diffuse by the reptation mechanism and thus the D* can be related to microscopic properties[11],

$$D^* = D_{rep} = \left[\frac{4}{15} M_o M_e \frac{k_b T}{\zeta_o}\right] M^{-2} \qquad (1.3)$$

where M, $M_o$ and $M_e$ are the polymer, monomer and entanglement molecular weights respectively, $\zeta_o$ is the monomeric friction coefficient, while $k_b$ and T have their usual meanings. It is important to note that the parameters which dictate D*, and also D, are *temperature, molecular weight, and chain structure* (through the monomeric friction coefficient). For high molecular weight polymers annealed ~70 degrees above the glass transition temperature, diffusion coefficients typically range from $10^{-10}$ to $10^{-15}$ $cm^2sec^{-1}$. For annealing times of 60 minutes, the expression for w (the characteristic diffusion distance) predicts that the interfacial thickness will range from 38μm to 38nm respectively. This simple calculation shows that techniques with high spatial resolution (100 Å) are necessary if experiments are to be conducted over a convenient time period. Nevertheless,

many lower resolution yet simple techniques can be used to study polymer-polymer diffusion.

Infra-red (IR) microddensitometry is a simple and direct technique for measuring diffusion distances on size scales of tens of μm. Figure 1.3 describes the experimental procedure[12].

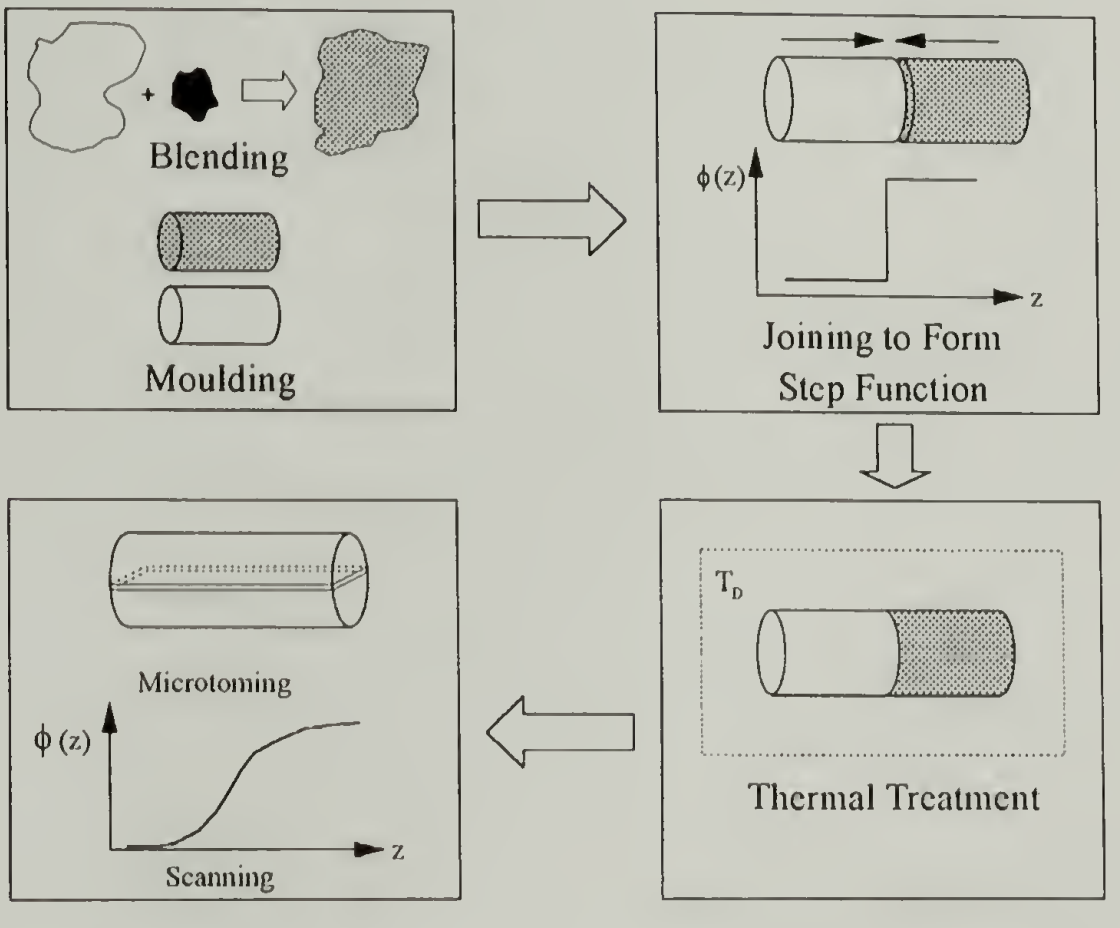


Figure 1.3 Schematic flowchart showing the stages involved in the experimental procedure of an IR microprobe experiment for the measurement of concentration profiles of $w > \sim 200$ μm. Adapted from Reference 12.

The IR beam used for the scanning is tuned to the frequency of interest, and passes through a set of slits with spacing of ~ 90μm. The concentration profile is measured by stepping the sample across the beam in small increments. Contrast is provided by the different vibrational frequencies of the bonds. For example, if one of the components is deuterated, one could use the C-D (~2200cm$^{-1}$) and C-H (~3000cm$^{-1}$) stretching frequencies. Similar to IR, the modified optical Schlieren technique (MOST) relies on a refractive index difference between polymers. In MOST, visible light is deflected as the

beam passes through a refractive index gradient. The diffusion coefficient is determined by measuring the angular deflection of light, which in turn is inversely proportional to the concentration gradient. Using MOST, Ye et. al. measured the D in a series of PS and poly(vinyl methyl ether) blends[13]. IR microdensitometry and MOST are attractive because they can be set up in-house. Moreover, IR provides the concentration profile directly, without any inverting of spectra. However, because polymers diffuse slowly, long annealing times are required to achieve significant interfacial broadening. Therefore, sample degradation and temperature fluctuations during annealing can be significant problems.

Energy dispersive x-ray analysis, also called electron microprobe, has better spatial resolution than IR and is a direct profiling technique. Also called the electron microprobe because of its 1μm spot size, this technique makes use of the characteristic x-rays from atoms excited by energetic electrons. Hence, contrast must by provided by an element of moderate to high atomic number such as chlorine. A scanning electron microscope directs a ~1μm electron beam onto a microtomed or fractured surface and scans the beam across the surface.[14] Upon encountering the sample, the electrons deviate strongly from their initial direction due to large angle and multiple elastic scattering. This scattering limits the resolution to about 3μm. For comparison, the range of 20keV electrons in polymers is approximately 10μm[15]. The characteristic x-ray counts are detected by a Si(Li) solid state detector and converted to concentration by normalizing with respect to the x-ray count far from the interface. Because the fluorescence signal is weak, the scanning speed of the microprobe is slow, resulting in radiation damage to the sample. Degradation can be reduced by scanning parallel to the interface to increase the signal, allowing for faster scan rates and therefore less radiation damage.

In recent years, the application of ion beam techniques to investigate the interfacial behavior of polymers has become increasingly popular. Because Rutherford backscattering (RBS) has been developed for semiconductor analysis, several excellent text books are

available on this subject[16]. Although RBS has been extremely useful for several polymer interface studies[17,18], we discuss the analogous techniques for probing the depth distribution of light elements, namely forward recoil spectrometry (FReS) and nuclear reaction analysis (NRA). A recent review by Shull[19] presents a detailed account of FReS.

In a FReS experiment, a beam of helium ions with an energy Eo = 3.0MeV strikes the sample at a glancing angle, usually 15 degrees, as shown in the schematic diagram of FReS geometry in Figure 1.4.

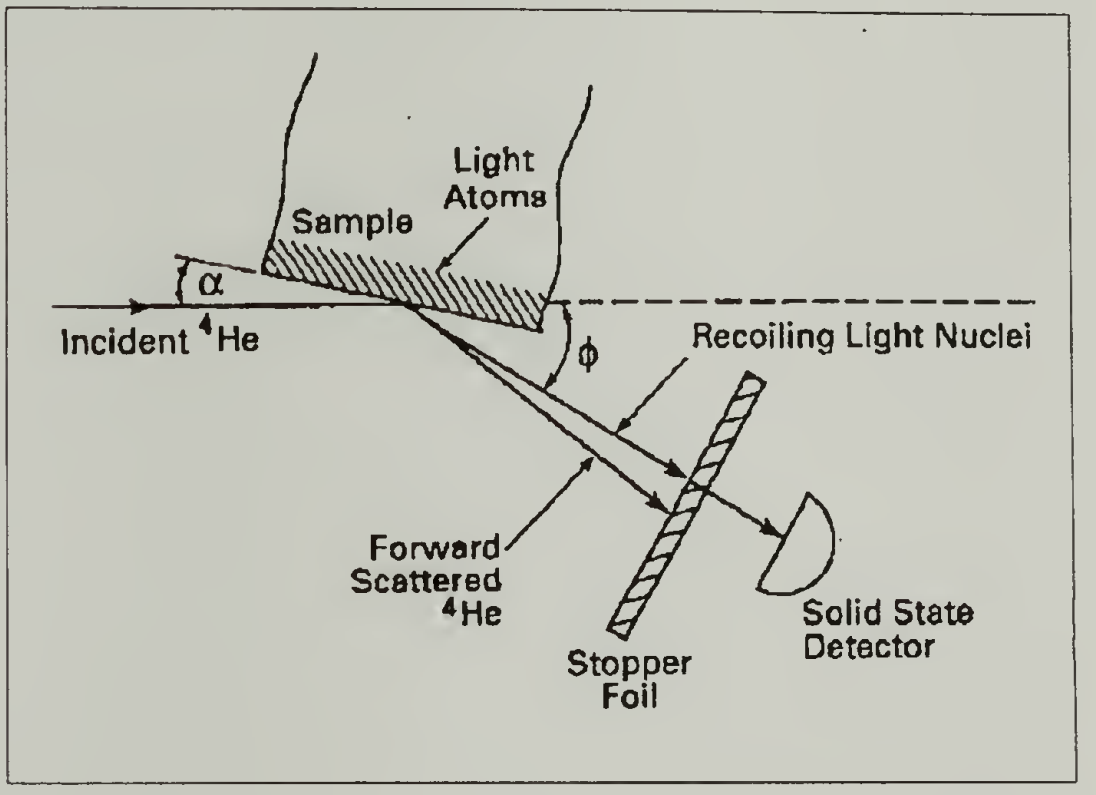


Figure 1.4 Schematic view of a FReS experiment. See text for details.

Deuterium and hydrogen nuclei from the sample are recoiled out of the sample due to elastic collisions with the incident He. If the incoming He ion collides with a target nucleus at the surface of the sample, the target receives a constant fraction of the energy of the incident ion: 0.67 for deuterons and 0.48 for protons. Thus, deuterons and protons recoiled from the surface are well-separated in energy. In practice, a stopper foil (typically a 10μm mylar film) is placed in front of the detector to filter the forward-scattered He.

Deuterons and protons recoiling from beneath the surface are detected at lower energies because the incoming incident and outgoing target particles lose energy due to inelastic collisions with electrons in the sample.

Figures 1.5a and 1.5b show a FReS spectrum and concentration profile[20] for a thin film of DPS on a PS:poly(xylenyl ether) matrix after the DPS layer has diffused about 3000 Å into the matrix.

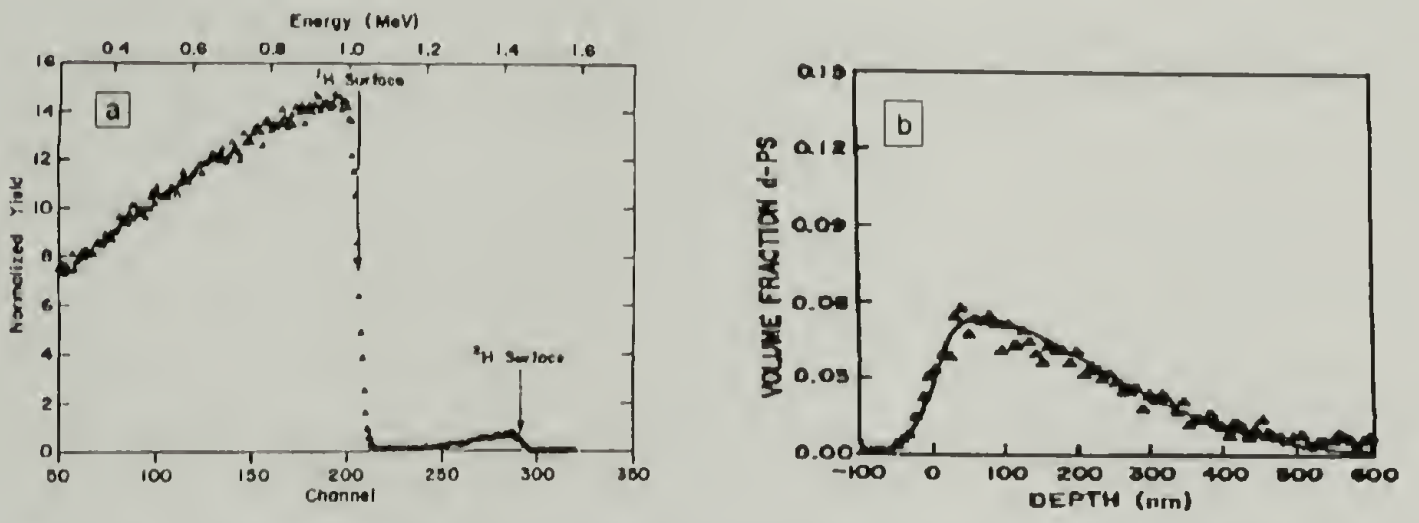


Figure 1.5 FReS spectrum of a PS : PXE blend into which DPS has diffused about 3000 Å. 1.4a shows both the H and D signals while 1.4b shows the corresponding depth profile.

The DPS can diffuse about 7000 Å beneath the surface before its signal (deuterium) begins to overlap the signal from hydrogen at the surface. The depth resolution (discussed below) is about 800 Å and is most apparent at the front edge, (z =0 Å) of the sample. Note that the energy of the recoiled particles is directly related to their initial position in the sample. Hence, a properly-designed FReS experiment can yield the concentration profile of a D-or H- containing component directly and unambiguously. Another advantage of FReS is its sensitivity--volume fractions as low as 0.01 can usually be detected.

One can best understand the depth resolution of FReS in terms of the energy spread of the detected particles.[21] If z is a spatial coordinate normal to the surface, the depth resolution $\Delta z$ is given as

$$\Delta z = \frac{dE_t}{\left(\frac{dE}{dz}\right)} \tag{1.4}$$

where $\frac{dE}{dz}$ is the stopping power of protons (or deuterons) in the sample and the total spread in energy $\delta E_t$ is given by

$$\delta E_t^2 = \delta E^2_{\text{detector}} + \delta E^2_{\text{geometry}} + \delta E^2_{\text{stopper foil}} + \delta E^2_{\text{straggling}} \tag{1.5}$$

Here, $\delta E_{\text{detector}}$ is the inherent energy resolution of the detector, and $\delta E_{\text{geometry}}$ results from finite beam divergence and detector acceptance angles. As the recoiled particles traverse the stopper foil, their energies are spread in such a way that if they are mono-energetic upon entry, they have a (nearly) Gaussian distribution of energy upon exit–they straggle. $\delta E_{\text{stopper foil}}$ is proportional to the thickness of the stopper foil, and is usually the dominant term in the expression for $\delta E_t$. Straggling can also occur in the sample itself, which gives rise to the last term, $\delta E_{\text{straggling}}$, though this term is usually small. As mentioned above, the typical depth resolution for FReS is about 800 Å. Recently, the resolution of FReS has been improved[22] to about 300 Å by replacing the stopper foil with a time-of-flight filter, which electronically prevents the detection of forward-scattered He particles (TOF FReS). The main disadvantages accompanying time-of-flight analysis are decreased detector sensitivity and the complexity of incorporating TOF instrumentation into the FReS sample chamber.

### 1.3.2 Techniques for Measuring Concentration Profiles on the Order of the Molecular Size (w = 1-100 Å)

Consider a partially-miscible binary blend of two homopolymers of the idealized geometry shown in Figure 1.2. For $\chi > \chi_c$, the two coexisting phases are separated by an interface of finite width. The volume fraction profile is given by

$$\phi(z) = \frac{1}{2}\left((\phi_1 + \phi_2) + (\phi_2 - \phi_1)\tanh\left(\frac{z}{w}\right)\right) \qquad (1.6)$$

where w is the interfacial width, and

$$w \sim \chi^{-1/2} \qquad (1.7)$$

Because w depends on $\chi$, the interfacial widths exhibited by high polymers range from tens of Ångstroms (for, example, the PS/polybutadiene interface)[23] to several hundred Ångstroms (for the PS/DPS immiscible interface). Correspondingly, the resolution required to measure concentration profiles at these interfaces is FWHM 200 Å and less. In this section, we present several examples of immiscible polymer interfaces to introduce the ion beam techniques of NRA and SIMS, and Neutron Reflection (NR). A detailed discussion of NR shall also be presented in Chapter 2.

Though miscible at low and moderate molecular weights, the PS : DPS system exhibits partial miscibility[24,25] at high molecular weights ($N > 10^4$, where N is the degree of polymerization). From Equation 1.7, the small $\chi$ value for this system leads us to expect rather large interfacial widths between the PS-rich and DPS-rich coexisting phases. Indeed, this system has proven amenable to investigation using higher-resolution ion beam

techniques, NRA (nuclear reaction analysis) and DSIMS[26] (dynamic secondary ion mass spectroscopy).

The experimental geometry for an NRA experiment is similar to the FReS experimental geometry (shown in Figure 1.4) with the exception that the stopper foil is replaced by a magnetic field. The incident particles, typically a collimated beam of ~700 keV $^{3}He$ ions, enter the deuterium-labeled polymer sample, and lose energy (due to inelastic electronic collisions) as they traverse the sample. Deuterons in the sample can react with these incident $^{3}He$ particles according to the reaction

$$^{3}He + ^{2}H \rightarrow ^{4}He + ^{1}H, \quad Q = 18.352 \text{ MeV} . \qquad (1.8)$$

The $^{4}He$ particles produced in the nuclear reaction traverse the sample (again losing energy in the process) and are separated from the incident $^{3}He$ particles by the magnetic field and then detected using an energy-sensitive detector. The energy spectrum of the detected $^{4}He$ particles is then analyzed in terms of the calibrated energy loss and reaction cross-section to yield the deuterium depth profile.[27,28] A significant advantage of NRA is its depth resolution, typically FWHM 14 -200 Å, which can be satisfactorily described using Equations 1.4 and 1.5, setting $\delta E_{\text{stopper foil}} = 0$. (Recall that $\delta E_{\text{stopper foil}}$ was the primary contributor to the energy spread for FReS.) The primary disadvantage of NRA is that the cross section for the nuclear reaction is lower than the recoiling cross section for FReS, leading to longer data collection times and greater potential for sample damage during data collection.

So far we have focused our attention on light ions in the MeV range traversing polymer samples. In these cases, the stopping power of most polymers arises predominantly through electronic interactions between the ions and the material. However, for ions of higher mass ($Ar^{+}$ or $Cs^{+}$, for example) at lower energies (in the 1 to 10 keV range) the nature of the stopping power of most polymers changes. Stopping

occurs via nuclear processes[11] , and its cross section is orders of magnitude higher than the cross sections for the FReS and NRA processes mentioned in the preceding paragraphs. Under these conditions, the polymer sample is sputtered, creating a crater and a collection of secondary ions (and neutral particles). The ion beam can be rastered over a small area (~0.2 $mm^2$) of the sample and, as the crater deepens, the ions of interest can be extracted and detected with a mass spectrometer[29]. Named dynamic secondary ion mass spectroscopy (DSIMS), this process has proven useful for depth profiling in polymers and their blends.

The material at or near the base of the crater undergoes mixing during the sputtering process via two mechanisms: re implantation of sputtered particles by collisions with primary ions, and cascade mixing, caused by secondary recoil events set off by the primary ions entering the sample. For polymers, cascade mixing is usually the more important of these two factors and limits the depth resolution of DSIMS to FWHM~130 Å. The advantages of DSIMS are its high depth resolution and the ability to profile a wide variety of chemical species ($^1H$,$^2H$ , O, N, and others). The primary disadvantage of DSIMS is that the sputtering rates of most samples are very sensitive to the sputtering conditions and also depend on local composition, making DSIMS data difficult to analyze quantitatively.

Figure 1.6 shows $D^-$ and $CN^-$ ion traces for a ~900Å film of a d-styrene-2vinyl pyridine triblock copolymer (VP-S-VP) on a silicon substrate.[30] While DSIMS lacks the spatial resolution to resolve features of the concentration profile on the order of the interfacial width (probably 40–70Å), the oscillations in these data sets provide dramatic evidence for the orientation of the lamella with respect to the surfaces.

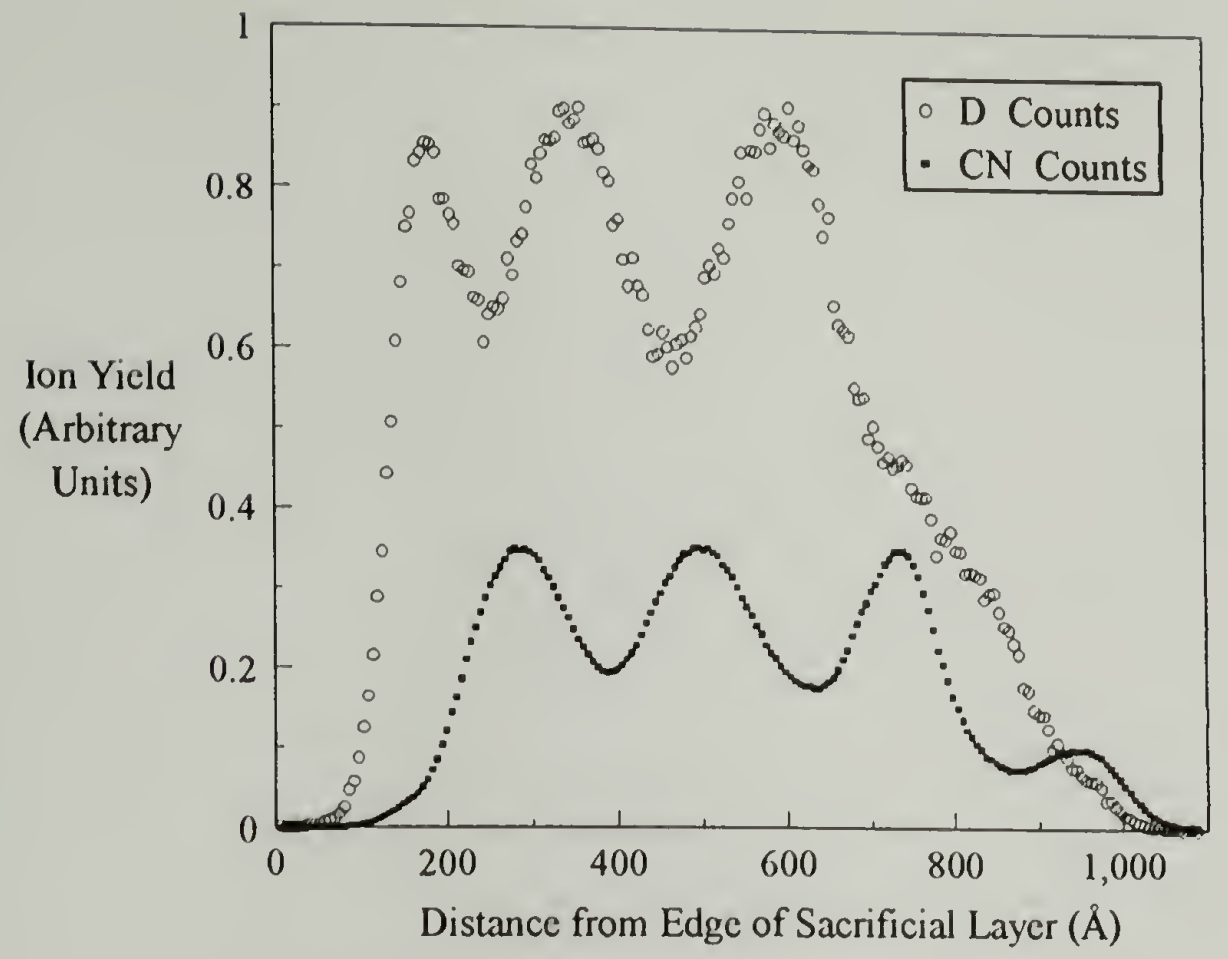


Figure 1.6 DSIMS $D^-$ and $CN^-$ ion traces for a ~900Å film of 2 vinyl pyridine - d-styrene- 2 vinyl pyridine triblock copolymer. The lamellar period (~215Å) and the orientation of the lamella normal to the surface are clearly evident.

In the example discussed in the previous paragraphs, we saw that DSIMS was useful for investigating lamellae (~400 Å in size), but not the interfaces between lamella (~50 Å in size, the range of many polymer interfaces). To investigate features such as these immiscible interfaces, the technique of choice is neutron reflection. The strengths of NR are its high spatial resolution (~10 Å), good penetration in many polymers (typically ~2000 Å) and its non-destructive nature. On the other hand, one important limitation of NR is that it does not provide a direct measure of the scattering length density profile. Just as a color on a thin oil film may correspond to more than one order of reflection (and therefore more than one thickness/refractive index pair), an NR spectrum does not necessarily correspond uniquely to a single scattering length density profile. Further,

because neutron sources possess low flux, one must usually use a "large" beam, and therefore, large samples (~5 - 10 cm) to obtain suitable results. Nevertheless, NR can be invaluable in measuring concentration profiles on small size scales or near "buried" interfaces, especially when used in conjunction with direct techniques (albeit lower resolution) such as FRES or SIMS.

### 1.3.3 Summary of Techniques for "Buried" Interfaces

In this section, we have presented polymer interface problems and, in that context, concentrated on characterization techniques for investigating "buried" interfaces. Table 1.1 summarizes these techniques in terms of size scale, contrast, probe particles. It is worthwhile to bear in mind that the best route to characterizing polymer interfaces usually involves capitalizing on the synergism between two or more different experimental techniques. Often a direct technique (of moderate depth resolution) can be used in conjunction with an indirect one (of high spatial resolution) to provide as complete a picture of the interface(s) as possible. Techniques not directly applicable to buried interfaces (contact angle, XPS, ATIR, etc.) can also play roles in multi-technique approaches to polymer interfaces.

Table 1.1 Summary of techniques for the study of interfaces of polymer melts and solids.

| Technique | depth resolution | probe radiation | contrast |
|---|---|---|---|
| IR microdensitometry | 90μm | Infra-red | IR absorption bands |
| MOST | 0.5mm | visible radiation | refractive index |
| Electron Microprobe | 3μm | electron beam | electron density |
| FReS | 800 Å | ~3Mev $He^{+}$ or $He^{++}$ | hydrogen/deuterium |
| TOF FReS | 300 Å | ~3Mev $He^{+}$ or $He^{++}$ | hydrogen/deuterium |
| NRA | 150-200 Å | ~700kev $^{3}He$ ions | hydrogen/deuterium |
| DSIMS | 130 Å | ~10 kev ions (Ar+,Cs+,O+,etc.) | H, D, C, O, others |
| Neutron Reflection | 10 Å | neutrons, λ=1.5 - 15Å | hydrogen/deuterium |

## 1.4 Techniques for Characterizing Polymers at the Solution/Solid Interface

Ellipsometry is based on the principle that a film on a substrate can change the state of polarization of light reflected from the substrate. One type of ellipsometry experiment is shown in Figure 1.7, in which an elliptically–polarized beam of light encounters a reflective substrate bearing an adsorbed polymer.

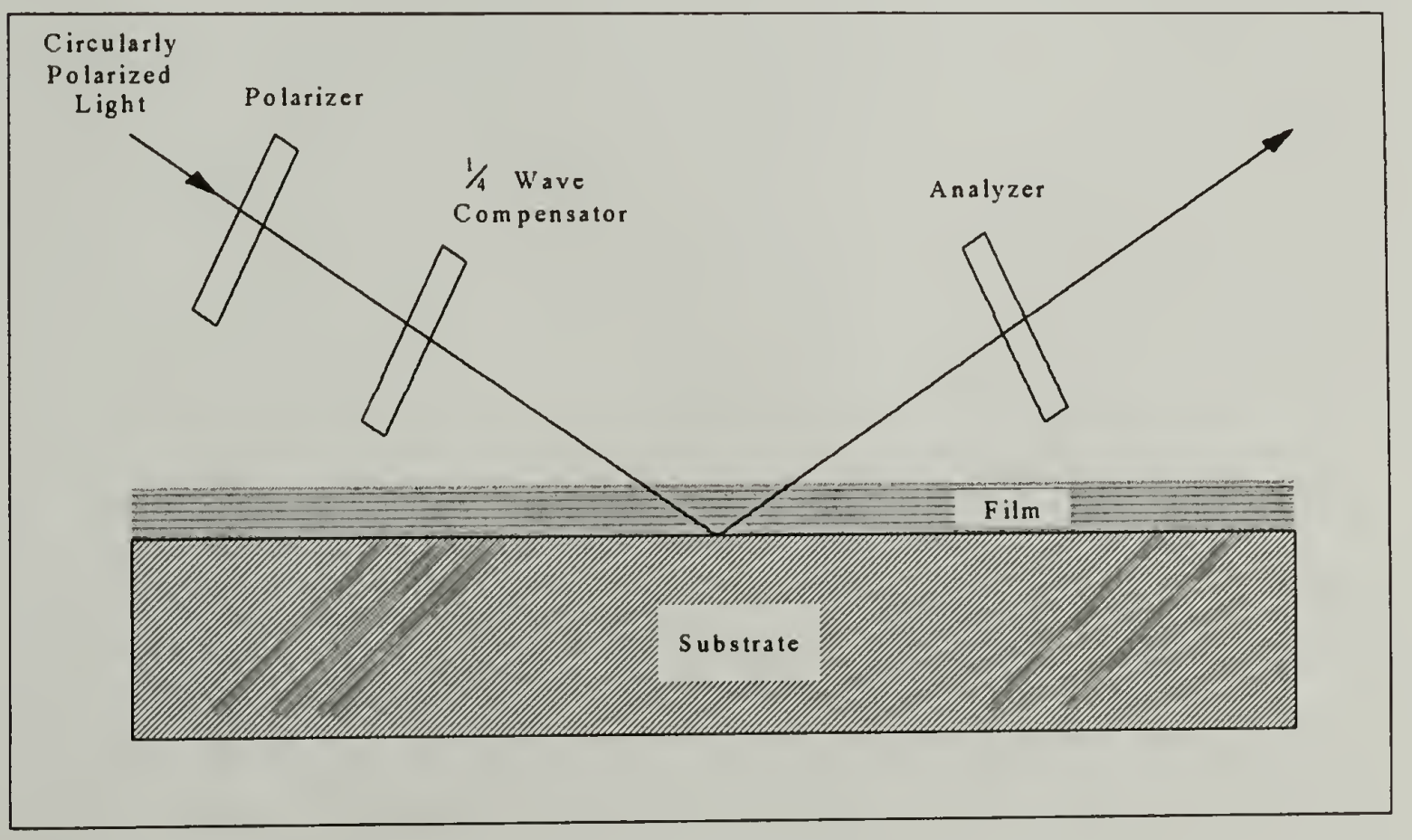


Figure 1.7 Schematic diagram of an ellipsometry measurement.

For a given compensator angle, there is a polarizer azimuth at which the elliptically polarized light becomes linearly polarized upon reflection. The analyzer can be then rotated 90° to obtain true extinction, which is accomplished by alterternatively rotationg the polarizer and analyzer. The azimuth of the polarizer at null is a measure of $\Delta$ and the analyzer azimuth is a measure of $\Psi$. It can be used to provide very accurate measurements the adsorbed amount of polymer. However, this technique cannot provide explicit information about the polymer concentration profile.

Motschmann and coworkers have investigated the kinetics of adsorption of block copolymers of styrene and ethylene oxide onto silicon from toluene.[31] They used ellipsometry to measure the amount of polymer (typically less than 4 $mg \cdot m^2$) adsorbed as a function of time, and reported two regimes, an initial diffusion–controlled regime followed by a period of slower growth toward saturation.

Another example of a technique capable of providing a measure of the adsorbed amount of polymer is ATR-FTIR. Unlike the ellipsometry technique, FTIR is capable of distinguishing between two or more components potentially capable of adsorbing at the substrate on the basis of their vibrational spectra. In an ATR-FTIR experiment, the IR beam enters a silicon probe immersed in the polymer solution. The beam is internally reflected several times as it propagates through the probe, accumulating information about the local polymer concentration with each reflection. The spatial resolution is limited by the relatively large wavelength of IR (on the order of several μm). Thus, while IR can be used to measure adsorbed amounts of one or more polymers at the substrate, it provides no other details about the polymer concentration profiles.

Taunton and coworkers have demonstrated that polymer chains attached to two mica surfaces prevents them from coming into contact under conditions where they would otherwise exhibit overwhelming mutual attractive forces.[32] Several groups have observed

significant repulsive forces at separations of more than 10 times the "normal" dimensions of the polymers in solution, evidence of strong stretching of "grafted" polymer chains These results are a direct and graphic illustration of the role polymers can play in the modification of surfaces. While the force balance technique can provide a measure of the of the adsorbed layer's thickness, no other explicit details of the concentration profile are available.

Finally, small angle neutron scattering (SANS) has been used to investigate polymers terminally-attached to a porous silica substrate.[33] SANS has the advantage of allowing measurement of polymer concentration profiles on size scales smaller than typical polymer chains (20Å or less). In a SANS experiment of this type, the polymer is grafted to the porous silica substrate (which is a pore size of ~4000Å). These particles are placed in a solvent (good or poor) which refractive index matches the substrate. The scattered neutron intensity of the suspension is then measured as a function of q, which is given by $q = \frac{4\pi}{\lambda}\sin(2\theta)$, where $\theta$ is the scattering angle. Under these conditions, the adsorbed amount of polymer and the thickness of the adsorbed layer can be obtained from the scattered intensity at low q from

$$Iq^2 = 2\pi \frac{S}{V}(\rho_{np} - \rho_{ns})^2\Gamma^2 \left(1-q^2\frac{h^2}{\alpha}\right) \qquad (1.9)$$

where $\frac{S}{V}$ is the specific surface area, $\rho_{np}$ and $\rho_{ns}$ are the scattering length densities of the polymer and solvent respectively (see Section 2.1.5), $\Gamma$ is the grafted amount of polymer, L is the thickness of the polymer layer, and $\alpha$ is a constant on the order of unity. One attractive feature of this technique is that the polymer can be observed in situ. This technique can also be sensitive to the shape of the polymer concentration profile, allowing one to distinguish between "steplike" concentration profiles and those where the polymer concentration profile decays gradually. Like neutron reflection, SANS is an indirect technique. Therefore, SANS results are subject to more or less the same uniqueness

limitations as NR. Unlike NR, however, the experimental geometry of a SANS experiment prohibits the use of complimentary (direct) techniques such as SIMS or FRES for the verification of SANS results (see section 1.3.2).

## 1.5 Summary

Techniques for the measurement of polymer concentration profiles have been presented in this chapter. While the set of techniques discussed in this chapter is by no means complete, the reader can certainly gain an appretiation of the experimental evaluation of polymer interfaces (especially buried interfaces) from the above sections. Because each technique offers its own strengths for the characterization of polymer interfaces, the best experimental approaches are designed to capitalize on the synergy between two or more of them. Indeed, the best approaches are multi-technique approaches.

## References


[1]R. Pandit, M. Schick, M. Wortis *Phys. Rev. B* **26** 5112 (1982).

[2]E. Helfand, Y. Tagami, *J. Chem. Phys.* **56**(7), 3592 (1972).

[3]R. Fayt, P. Hadjiandreou, P.H. Teyssie, *J. Polym. Sci. Polym. Chem.* **23** 337-342 (1985.

[4]P.G. Shewmon, *Diffusion in Solids*; McGraw Hill, 1963.

[5]R.J.Composto,E.J. Kramer, D.M. White; *Macromolecules* **21** 2580 (1988).

[6]P.F.Green, B.L. Doyle, *Macromolecules* **20** 2471-74.

[7]P.F.Green, B.L. Doyle, *Phys. Rev. Lett.* **57** 2407-10.

[8]W.W. Graessley, *Adv. Polym. Sci.* **16**, 1 (1974).

[9]M. Doi, S.F. Edwards, *The Theory of Polymer Dynamics*, Clarendon Press, Oxford, 1986.

[10]H.H. Kausch, M. Tirrell, *Annu. Rev. Mater. Sci.* **19**, 341-377 (1989).

[11]P.G. de Gennes; *J. Chem Phys.* **55**, 572 (1971).

[12]J. Klein, B.J. Briscoe, *Proc. R. Soc. Lond.* **365**, 53 (1979).

[13]M. Ye, R.S. Stein, R.J. Composto *Macromolecules* **23** 1990, Ye Ph.D. thesis, Univ. of Massachusetts.

[14]F.P. Price, P.T. Gilmore, E.L. Thomas, R.L. Laurence *J. Polym. Sci. Polym. Symp.* **63**, 33-44 (1978).

[15]L.C. Feldman and J.W. Mayer, *Fundamentals of Surface and Thin Film Analysis*, Elsevier Science, NY,1986.

[16]W.K. Chu, J.W. Mayer, M.A. Nicolet, *Backscattering Spectrometry*; Academic Press, NY, 1978.

[17]R.J. Composto and E.J. Kramer, *J. of Materials Science* **26** 2815 (1991).

[18]P.F. Green et.al *Macromolecules* **18** 501 (1985).

[19]K. Shull, *Physics of Polymer Surfaces and Interfaces*; ed. I. Sanchez, Butterworth-Heinimann and Manning, 1992.

[20]R.J.Composto, E.J. Kramer, D.M. White; *Macromolecules* **21** 2580-2588 (1988).

[21]Turos et.al. *A. Nucl. Inst. Meth.* B4, **92** (1984).

[22]M.H. Rafailovich, J. Sokolov, X. Zhao, R.A.L. Jones, E.J. Kramer, *Hyperfine Interactions* **62**, 45-53 (1990).

[23]J. Genzer, APS Bulletin.

[24]F.S. Bates, G.D. Wignall, W.C. Kohler, *Phys. Rev. Lett.* **55**, 2425 (1985).

[25]F.S. Bates, G.D. Wignall, *Phys. Rev. Lett.* **57**, 1429 (1986).

[26]S.J. Whitlow, R.P. Wool, *Macromolecules*. **22** 2648-2652 (1989).

[27]U.K. Chaturvedi et.al. *Phys. Rev. Lett.* **63**(6) 616-619 (1989).

[28]Steiner et.al. *Makromol. Chem. Macromol. Symp.* **45** 283-288 (1991).

[29]A. Benninghoven, F.G. Rudenaur, H.W. Werner, *Secondary Ion Mass Spectroscopy, Chemical Analysis Series*; John Wiley: New York, 1987; Vol.86.

[30]M.H. Rafailovich and J. Sokolov, Private Communication.

[31]H. Motschmann, M. Stamm, Ch. Toprakcioglu *Macromolecules* **24** 3681 (1991).

[32]H.J. Taunton, C. Toprakcioglu, L.J. Fetters, and J. Klein *Nature* **332** (21) 712 (1988).

[33]P. Auroy, L. Auvray, and L. Léger Phys. Rev. Lett. 66 719 (1991).

# CHAPTER 2

# NEUTRON REFLECTION AND POLYMERS AT SURFACES

As discussed in the previous chapter, several techniques can provide direct information about polymer interfaces on size scales of ~150Å or larger. However, to investigate features such as the interface between two immiscible polymers, one often turns to neutron reflection. In Section 2.1, some basic principles of neutron reflection are developed, often using analogies with reflection of visible radiation. These principles include total reflection and refraction (section 2.1.2), expressions for the intensity of reflected radiation (sections 2.1.3 and 2.1.4), and mechanisms of contrast (section 2.1.5). In section 2.2, a specific description of methodology for NR data analysis of polymers is presented.

## 2.1 Physical Principles of Reflection

Although the (Latin and Greek) roots of the word *optics* are related to seeing and the eyes (and hence to visible radiation), modern usage of this word is often more general. The term *optics* can be applied in the context of many types of radiation, including x–rays, electrons and neutrons. Because much of the work presented in this thesis is closely related to the reflection of neutrons, the principles presented in this chapter will be presented in the context of neutrons, often via analogy with optics in the classical sense.

### 2.1.1 Similarities Between Optical and Other Types of Radiation

While the nature of visible radiation differs substantially from that of neutrons, the physical relationships governing their reflection and refraction are often identical and can be readily applied to other kinds of radiation as well, if one allows for differences in the

mechanisms of the matter/radiation interactions. For example, the refractive index of any given material for visible radiation, x–rays, and neutrons depends on the polarizability, electron density, and scattering length density of that material respectively. In terms of their interaction with matter, the neutron 's de Broglie wave is analogous to the electromagnetic wave.

### 2.1.2 Total Reflection and Snell 's Law

The simplest case of reflection is that of radiation encountering a sharp, flat boundary separating two homogeneous optical media, as shown in Figure 2.1.

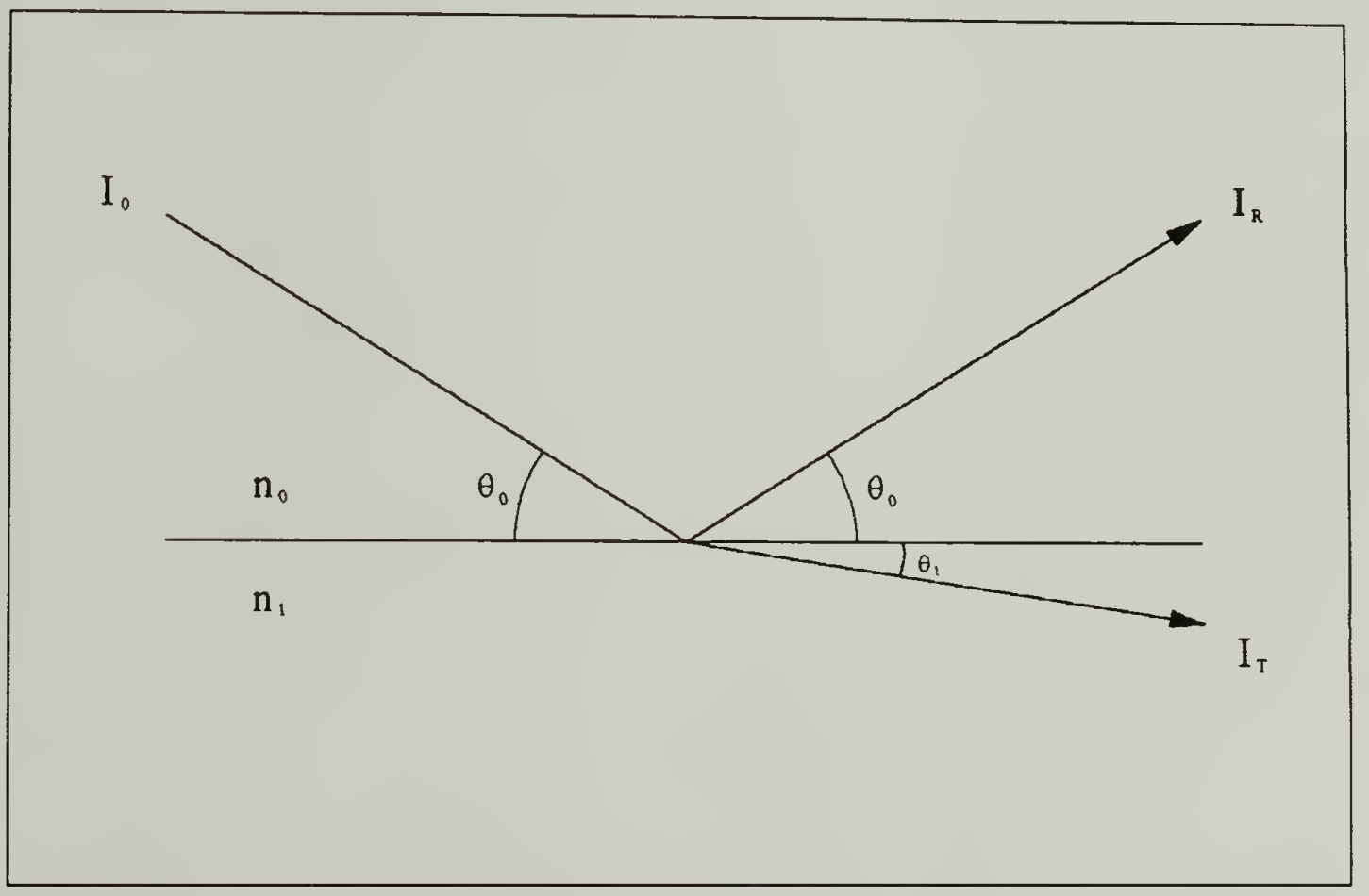


Figure 2.1 Schematic diagram of reflection at a single sharp boundary separating two optical media of refractive indices $n_0$ and $n_1$ where $n_0 > n_1$. The angles of incidence and refraction are $\theta_0$ and $\theta_1$ respectively. The critical angle $\theta_c$ is the $\theta_0$ value corresponding to $\theta_1 = 0$.

In this situation, the radiation, incident in medium 0 can enter medium 1 (refraction) or it can be reflected. One can calculate the intensity of the reflected radiation and discern the path taken by the refracted beam. These are the topics of this and the next sections. Note the particulars of the experimental situation. The refractive indices of media 0 and 1 are $n_0$ and $n_1$ respectively. The radiation encounters the boundary at an angle $\theta_0$, and the angle between the boundary and the refracted beam is $\theta_1$. The relation between the values n and $\theta$ is given by Snell 's law:

$$n_0 \cos\theta_0 = n_1 \cos\theta_1 \qquad (2.1)$$

Figure 2.1 is drawn such that $n_0 > n_1$. The refracted beam is "bent" away from the normal. In such a case there exists a critical angle $\theta_c$ corresponding to $\theta_1 = 0$.

$$\theta_c = \mathrm{Cos}^{-1}\left(\frac{n_1}{n_0}\right) \qquad (2.2)$$

At $\theta_0$ values less than $\theta_c$, the reflectivity R ($R = \frac{I_R}{I_0}$) is unity. At $\theta_0$ values greater than $\theta_c$, R decreases rapidly with increasing $\theta_0$, and can be calculated over the interval $0 < \theta_0 < \frac{\pi}{2}$ using the Fresnel equation, which is discussed in section 2.1.3. A particularly instructive example of this phenomenon is a mirage, which occurs when light propagating in cool air (medium 0) encounters a layer of warm air, (medium 1) usually next to a heated surface such as a road on a sunny day. Note that the "detector" (the observer 's eye) is situated in the cool air (which is "optically denser" than warm air). Let us assume that the boundary between the cool and warm air is sharp (a reasonable assumption for the calculation of $\theta_c$, but not for the magnitude of R). If the temperatures of the cool and warm air differ by 5°C, the refractive indices would differ by a few parts per million, corresponding to a

critical angle of ~0.1°, a "ballpark" value for a mirage. The physical picture for this example is qualitatively similar to neutrons (incident in air) encountering a typical polymer (say, Plexiglas), provided that $n_0 > n_1$. Hence, for neutrons, Plexiglas is "optically rarer" than air, whereas for light it is "optically denser" than air (see section 2.1.5). This is a good example of how the physical principles governing the reflection of many kinds of radiation are identical, even though the particular radiation/matter interactions can give rise to significantly different optical behavior. It is also worthwhile to note that the refractive indices of Plexiglas and air for neutrons differ from the refractive indices of warm and cool air for light to about the same extent–by a few parts per million.

### 2.1.3 The Fresnel Equation

In section 2.1.2, we calculated the critical angle for reflection from the boundary between two media of refractive indices $n_0$ and $n_1$ using Snell 's law. If the boundary is sharp and flat, the Fresnel equation can be used to calculate the reflection amplitude r of this boundary[1] in terms of its wave vector $k_0$ in the incident medium.

$$r = \frac{k_0 - k_1}{k_0 + k_1} \tag{2.3}$$

where

$$k_0 = \frac{2\pi}{\lambda}\sin(\theta) \tag{2.4}$$

and

$$k_1 = (k_0^2 - 4\pi\rho_n)^{1/2} \tag{2.5}$$

$\lambda$ is the wavelength of the neutron, and $\rho_n$ is the scattering length density (see section 2.1.5) of medium 1. The reflectance, r, and reflectivity R are related according to:

$$R = |r|^2 \tag{2.6}$$

### 2.1.4 Extension of the Fresnel Equation to Arbitrary Profiles of Refractive Index

The formalisms presented in sections 2.1.3 and 2.1.4 can be readily extended to the case of n+1 optical media separated by n sharp boundaries[2]. In this section, we show results for the case of n = 2, which would correspond to a thin film of oil on water (media 0, 1, and 2 being air, oil, and water respectively) or a thin d–polystyrene film on a quartz substrate. The Fresnel equation can be extended to this situation according to

$$r = \frac{r_{0:1} + r_{1:2}\exp\left(\frac{2ik_1}{d}\right)}{1 + r_{0:1}r_{1:2}\exp\left(\frac{2ik_1}{d}\right)} \tag{2.7}$$

where $r_{i:j}$ is the reflectance given by equation 2.3 of the boundary between media i and j and $k_i$ is given by equation 2.5 for medium i. Upon the addition of a second boundary, interference between neutrons reflected at the first and second boundaries becomes possible, as depicted schematically in Figure 2.2 for the case of a DPS film.

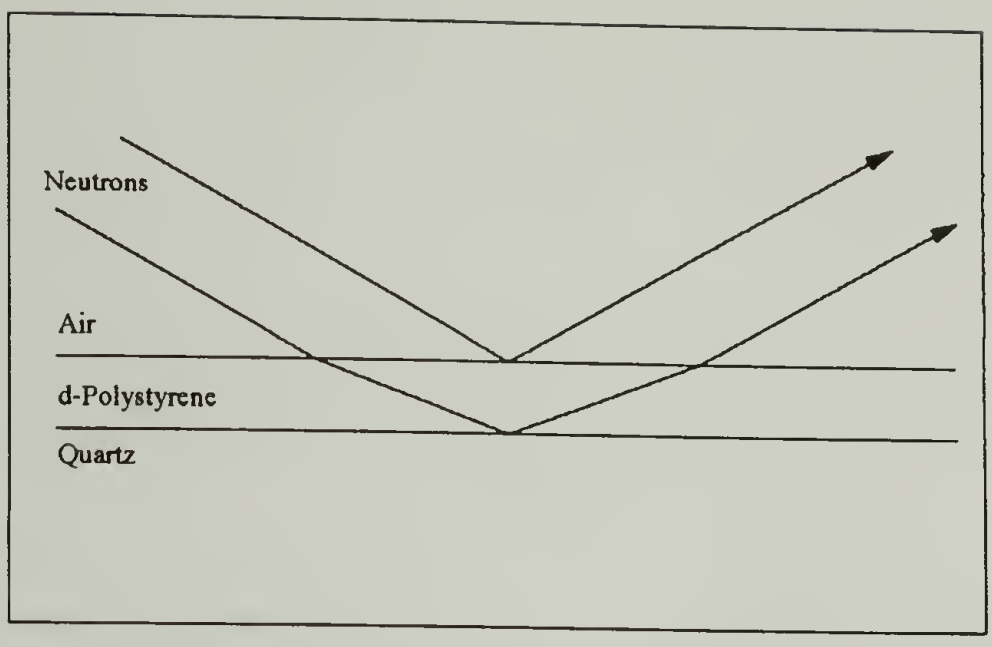


Figure 2.2 Schematic of two optical paths for neutrons encountering a polymer film on a quartz substrate. Because air is optically denser than d–polystyrene (i.e. $n_{air} . n_{DPS}$), the neutrons entering the polymer are "bent" away from the normal.

The exponential factor in equation 2.7 arises to account for the phase difference between neutrons reflected at different positions in the sample. Such interference is the origin of the colors present in thin oil films on water – the color one sees on the oil film possesses the wavelength satisfying the condition of constructive interference. Such interference can be readily observed experimentally for neutrons. Figure 2.3 shows the calculated neutron reflectivity of a 1000 Å DPS film on a silicon substrate using just such an extension (n= 2). Shown also, for reference, is the calculated neutron reflectivity of air/DPS boundary only. The profile of scattering length density (as a function of z, a spatial coordinate oriented normal to the surface, with the origin at the air/polymer boundary) is shown at the inset.

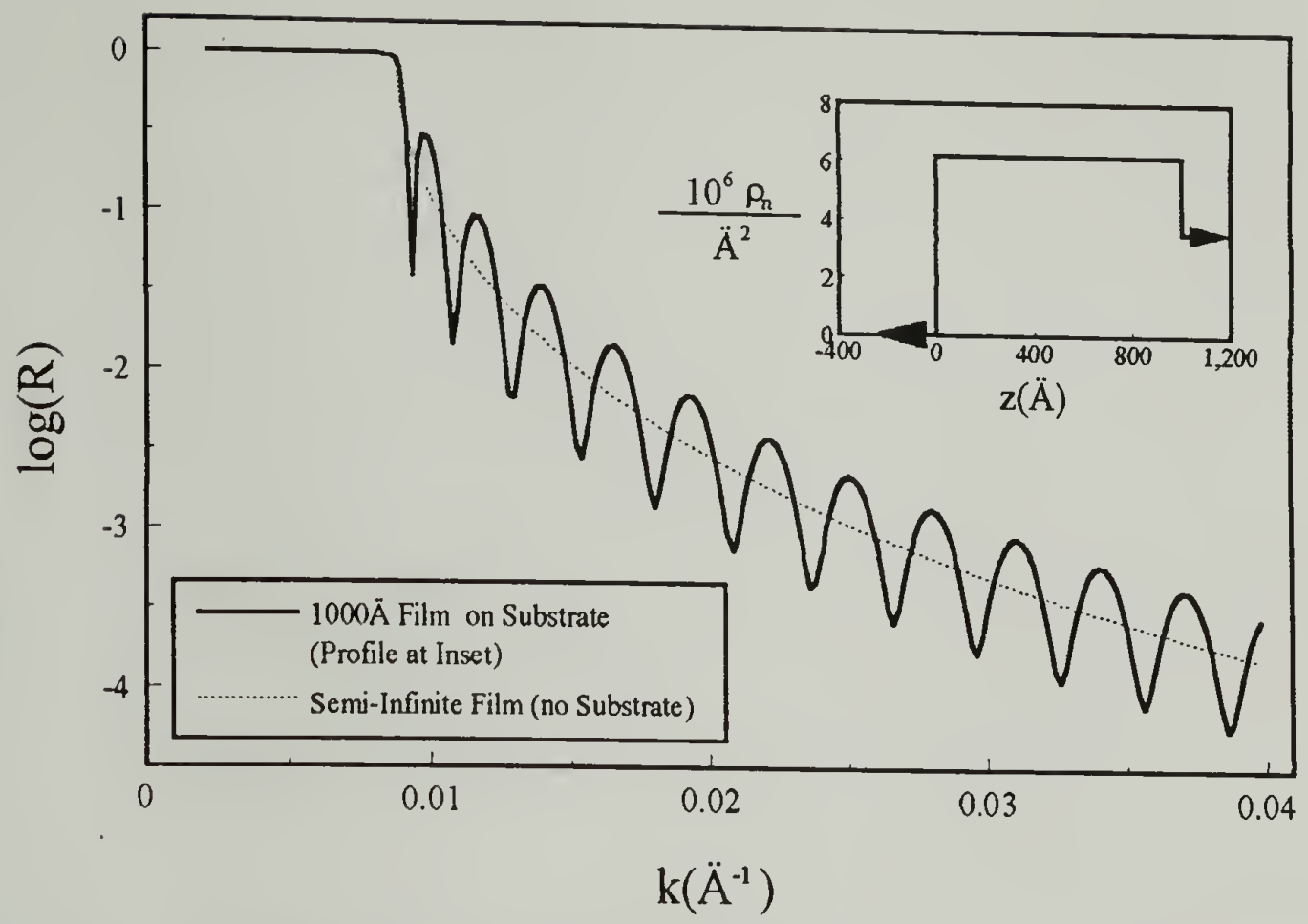


Figure 2.3 Calculated neutron reflectivity as a function of wave vector for a 1000Å film of DPS on a quartz substrate. The data were calculated from the profile of scattering length density shown at the inset. The dashed line is the calculated neutron reflectivity of a semi infinite DPS film. The maxima and minima in the reflected intensity of the 1000Å film manifest many orders of constructive and destructive interference between the beams reflected from the air/polymer and polymer/substrate boundaries.

Three features are worth noting: the critical k value, $k_c$, the rapid decrease in the reflectivity above $k_c$, and the oscillations superimposed on the reflectivity at $k > k_c$ , which arise from many orders of constructive and destructive interference between the neutrons reflected at the air/polymer and polymer/substrate boundaries. The periodicity $\Delta k$ of these oscillations is related to the thickness d of the polymer film by

$$\Delta k = \frac{\pi}{d} \qquad (2.8)$$

This type of interference is a dramatic indication of the wave like nature of the neutron, and is the key to the utility of neutron reflection in the investigation of polymers at

surfaces. The oscillations in the neutron reflectivity data from the DPS film contain the same kind of information as the color of the light reflected from the oil film–information about the thickness and refractive index of the sample.

The formalism expressed in Equation 2.7 can be used iteratively to calculate the reflectivity over any finite k range of a profile of $\rho_n(z)$ of arbitrary shape by creating a sufficiently fine histogram approximating $\rho_n(z)$. The condition which must be satisfied to obtain satisfactory precision is

$$\Delta z << \frac{\pi}{k_{max}} \tag{2.9}$$

where $\Delta z$ is the thickness of the layers in the histogram (assuming each layer has the same thickness) and $k_{max}$ is the largest value of k for which the reflectivity is calculated.

### 2.1.5 Neutron Potentials: Mechanisms for Contrast

For a given medium, the refractive index n for neutrons can be written as

$$n = \sqrt{1 - \frac{V_0}{E}} \tag{2.10}$$

where $V_0$ is the neutron 's potential in that medium, and E is the kinetic energy of the neutron. $V_0$ is determined by the interactions between the neutrons and the nuclei in the medium. In turn, the scattering length density $\rho_n$ depends on $V_0$ according to

$$\rho_n = V_0 \frac{2\pi h^2}{m} \tag{2.11}$$

where h is Planck 's constant and m is the mass of the neutron.

As a trend, $V_0$ increases with increasing nuclear radius. However, some significant resonances do exist, with the result of markedly different $\rho_n$ values for some nuclei even though they do not differ greatly in radius. An important example of such a pair is hydrogen and deuterium. One can significantly increase the value of $\rho_n$ for polystyrene by substituting deuterium for hydrogen–$(\rho_n)_{PS} = 1.35 \times 10^{-6}$ Å$^{-2}$ while $(\rho_n)_{DPS} = 6.2 \times 10^{-6}$ Å$^{-2}$. Thus, isotopic substitution of hydrogen in polymers offers a powerful way to obtain contrast for neutron scattering and reflection experiments.

### 2.1.6 Obtaining Concentration Profiles from NR Data

An important limitation of NR is that it does not provide a direct measure of the scattering length density profile. Just as a color on a thin oil film may correspond to more than one order of reflection (and therefore more than one thickness/refractive index pair), an NR spectrum does not necessarily correspond uniquely to a single scattering length density profile. In the analysis of neutron reflection data, one must (carefully) proceed with as much independently obtained information as possible.

## 2.2 Specific Description of NR Data Analysis for Polymers

While many of the examples in section 2.1 were presented in terms of polymers, most of the principles of reflection were discussed in general terms. The emphasis of this section is to focus on the application of NR to real polymer samples. Preparation of polymer samples for NR (and other surface analysis techniques) is presented in section 2.2.1. Section 2.2.2 addresses the application of the principles outlined in section 2.1 to real life experiments using non–ideal samples and radiation sources. Finally, chapter 2 ends with a discussion of specific strategies used to obtain information about polymer surfaces

from the experimental data, including the source code used for the case of a single polymer film (made of a miscible polymer blend) on a silicon substrate.

### 2.2.1 Sample Preparation

Like many other experimental techniques for surface analysis, NR requires smooth, flat, laterally homogeneous samples. Because present day neutron sources possess limited flux, the sample size usually required for NR measurements is large–20 to 80 $cm^2$ in area. The sample must usually be uniform in thickness over its entire area. The roughness of one or more of its surfaces can significantly affect its reflectivity. In short, sample preparation can be a very important (and sometimes frustrating) part of NR experiments. In the paragraphs below, methods for preparation of suitable samples will be outlined in order of increasing complexity. Two families of samples have been investigated in this dissertation: those which are liquids during measurement (solutions of polystyrenes or terminally–functionalized polystyrenes at the solution/solid interface), and those which are solids (one or more amorphous polymer films on a rigid substrate).

#### 2.2.1.1 Polymer Solutions at the Solution/Solid Interface

Figure 2.4 shows a schematic diagram of the solution cell, designed by S.K. Satija and C.F. Majkrzak, which was used for the polymer solutions presented in this dissertation.

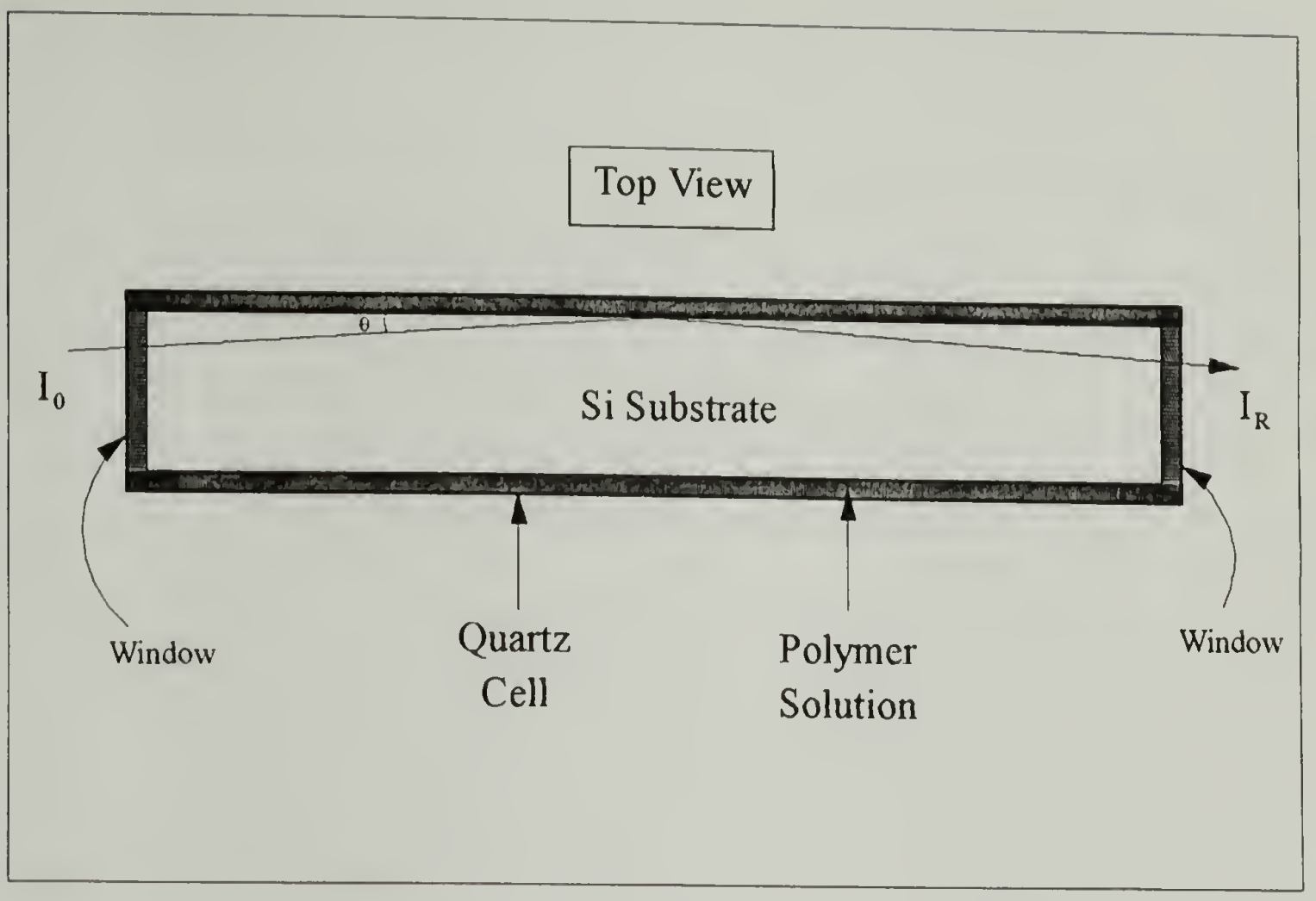


Figure 2.4 Schematic of cell used for in situ NR measurements of solution/solid interface. The incident beam enters the substrate (which is transparent to neutrons) and encounters the interface, avoiding most of the otherwise necessary traverse through the polymer solution. The angle of incidence θ typically ranges from 0.05° to 2.25°. The heights of the substrate and beam are both approximately 10 cm.

The substrate is a 20 cm x 10 cm x 2.5 cm single crystal of Si (n–type) with one face optically flat and polished to about 12Å FWHM roughness. This substrate rests inside a quartz cell with polished windows on each end, and occupies about 95% of the total cell volume, leaving ca. 25 $cm^3$ for the polymer solution, which is simply pipetted into the cell at the appropriate time. As shown in Figure 2.4, the interface is oriented vertically, corresponding to the cross section of the collimated neutron beam.

The collimated, monochromatized neutron beam passes through the cell window and approximately 1.5 mm of polymer solution, and then enters the substrate, where it

encounters the solution/solid interface at an angle of θ. Hence, a ~15 cm path through the polymer solution is avoided, resulting in significantly reduced incoherent scattering (which contributes to background) and attenuation of the main beam.

#### 2.2.1.2 Single Polymer Films on Flat Substrates

The study of polymer blends at surfaces and interfaces usually requires the formation of a polymer film supported by a smooth, flat substrate. To obtain satisfactory NR measurements, the polymer film must be smooth and uniform in thickness over its entire surface area. Spin casting is one of the few techniques available for forming such films. The general description of the spin casting process is simple. A polymer solution is pipetted onto the substrate, which is then spun at a speed on the order of 2000 rpm until the final film thickness is reached. If spinning continues until the polymer vitrifies, the final film thickness depends on the initial concentration of the polymer solution and the spinning speed.

Silicon wafers 5 mm in thickness and 5 or 10 cm in diameter (for experiments done at POSY II and BT–7 respectively) were used for all of the NR experiments presented in this dissertation. The substrate thickness (5 mm or more) is important so as to avoid bending of the substrate during spin casting and while the sample is mounted in the NR apparatus. To avoid scattering and absorption of neutrons, all substrates were single crystals of n–type silicon (p–type silicon is often doped with boron, an absorber of neutrons). Finally, the native oxide of all substrates (with the exception of the solution cell) was removed immediately before spin casting using an HF etch. This procedure provided clean substrates for spin casting with only small amounts of oxide re–formation during subsequent sample preparation and processing.

NR experiments of polymer blends usually requires smooth films (FWHM roughness on the order of 20Ä or less) uniform in thickness over the entire sample area.

Perhaps the most common imperfections in spin cast polymer films (aside from pinholes or pockmarks caused by dust) are variations in thickness: undulations (lateral fluctuations in thickness on size scales of a few millimeters or more) and wrinkles (lateral fluctuations in thickness on size scales of a few μm). Both of these problems can be lessened or eliminated by judicious choice of casting solvent and control of evaporation during spin casting. For example, while polystyrene can be spin cast suitably with many solvents (toluene or chloroform, for example) other polymers such as SAN or PC cannot (even though they are soluble in chloroform). 1,2 dichloroethane (DCE) or methyl isobutyl ketone (MIBK) are among the few suitable solvents for SAN copolymers, while DCE is one of the only suitable solvents for PC films of any thickness. The evaporation conditions during spin casting can be modified by covering the substrate with a small crystallizing dish (under which the air is nearly saturated with solvent vapor) during spin casting.

#### 2.2.1.3 Polymer Bilayers on Flat Substrates

The procedure for preparing samples with two (or more) layers is the same as outlined in the previous section for the layer next to the substrate. The upper layers can be added by spin casting them onto glass, lifting them from the glass in a small, clean pool of distilled water, and picking up the floating layer with the substrate and bottom film. After lifting the floating film, the sample should be partially covered (to allow for slow evaporation of water) and allowed to stand until the water evaporates and the films achieve intimate contact (typically 4 – 12 hours). If the lifting and re–deposition of the upper film are successful, it will have few or no wrinkles or striations when it dries. While the description of this procedure is simple, the actual task requires a steady hand and much patience, especially for larger (i.e., 10 cm) samples.

### 2.2.2 Complications Arising from Non–Ideal Samples and Radiation Sources

The schemes outlined in sections 2.1.2 – 2.1.4 were presented in the context of ideal radiation sources and samples. In any practical experimental situation, these idealized conditions cannot be realized. Neutron beams are imperfectly collimated and monochromatized. Because of limited neutron flux, the beams are often rather large–typically 4 –9 cm in height, and thus require large samples. The best substrates possess FWHM 12 – 20 Å roughness and may also posses undulations on larger size scales. The best polymer films possess similar roughnesses and vary in thickness by only a few percent over their overall area. While these departures from ideality usually do not make NR experiment impossible, they do have to be accounted for during the data analysis. In the following sections, practical methodologies for these experimental realities will be presented.

Imperfect collimation or monochromatization of the incident beam can cause features of the reflectivity spectrum (such as $k_c$ or maxima and minima in the reflected intensity) to become less distinct. Consider the case of a monochromatic but diverging neutron beam encountering a flat sample as shown in Figure 2.5.

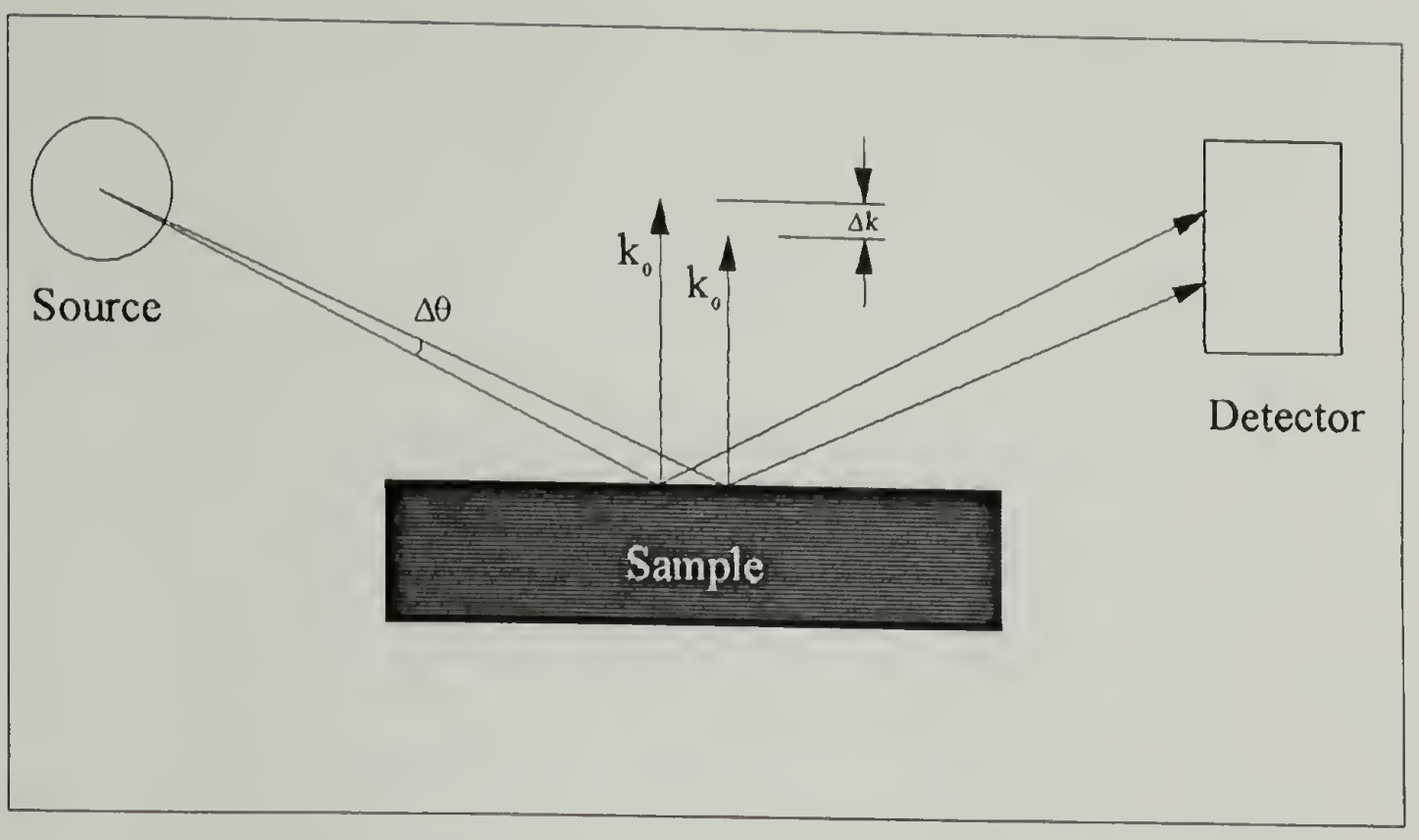


Figure 2.5 Schematic depiction of the effect of a diverging beam, incident on a flat sample. The angular spread leads to a spread in the $k_0$ values detected at any given experimental angle.

At a given experimental angle, the detector "sees" a distribution of k values $\Delta k$ reflected from the sample. The result is that reflectivity measured at a wave vector k is a "weighted average" of the sample 's reflectivity at all wave vector values adjacent to k. This weighted average can be quantified by a convolution integral

$$R(k) = \int_{-\infty}^{\infty} d\alpha \, g(\alpha) \, R(k-\alpha) \qquad (2.12)$$

where $\alpha$ is a dummy variable and $g(\alpha)$ is the resolution function at k, usually taken as a Gaussian function

$$g(\alpha) = \frac{1}{2\pi^{1/2}} \exp\left(-\frac{\alpha^2}{2\Delta k^2}\right) \qquad (2.13)$$

where $\Delta k$ is proportional to the divergence of the beam. For practical calculations, the resolution function is truncated at $\frac{g(\alpha)}{g(0)} \approx 0.02$. In practice, the resolution function depends on k, usually with $\Delta k$ increasing with increasing k.

In the absence of substrate bending, one can write the total wave vector spread $\Delta k$ as

$$\frac{\Delta k}{k} = \frac{\Delta \lambda}{\lambda} + \frac{\Delta \theta}{\theta} \qquad (2.14)$$

where $\lambda$ and $\theta$ are the wavelength and angle of incidence respectively. In practice, the beam divergence $\Delta\theta$ usually dominates this expression. The functional form of the terms in Equation 2.14 and the relative contributions to the total spread depends on the particular instrument. Analysis for an instrument at a pulsed source (POSY2) and a fixed wavelength source (BT–7) are presented below.

Equation 2.4 states that one can vary k by varying either $\theta$ or $\lambda$. At pulsed neutron sources, the neutron beam contains a distribution of wavelengths which impinge on the sample in pulses approximately 30 times per second. The most natural way to make NR measurements over a range of k values is to select an angle of incidence and allow all wavelengths: to impinge on the sample and measure the wavelength of the reflected neutrons by measuring their time–of–flight. At POSY 2, the usable neutrons range in wavelength from about 2 Å to 16 Å, corresponding to flight times of about 4 to 33 microseconds respectively. The time measurements are binned[3] in such a way that $\frac{\Delta t}{t} = A$ where $A \approx 0.009$. Because a neutron's wavelength is inversely proportional to its momentum (and hence velocity), one can write $\frac{\Delta \lambda}{\lambda} = \frac{\Delta t}{t} = A$.

To write the contribution of beam divergence, one must simply recognize that $\theta$ and $\Delta\theta$ are fixed and constant for a given data set: $\frac{\Delta \theta}{\theta} = B$ where B is a constant

determined by the collimation and the angle of incidence. Thus, for a given angle of incidence, one can write Equation 2.14 as

$$\frac{\Delta k}{k} = C \qquad \text{(POSY 2)} \tag{2.15}$$

where $C = A + B$.

The collimation of the BT–7 reflectometer, on the other hand, can be controlled independently of $\theta$. Typically, one increases $\Delta\theta$ with increasing $\theta$, providing more incident flux at large wave vectors (where the reflectivity is low) in such a way that $\Delta\theta = A' + B'\theta$ where A' and B' are constants. Thus, $\frac{\Delta\theta}{\theta}$ has the form $\frac{\Delta\theta}{\theta} = \frac{C_1}{k} + C_2$. Because the wavelength is selected using a monochromator, $\frac{\Delta\lambda}{\lambda}$ = constant = $C_3$. Thus, one can write Equation 2.15 as

$$\Delta k = C_1 + k(C_2 + C_3) \qquad \text{(BT–7)} \tag{2.16}$$

where $C_1$, $C_2$, and $C_3$ are constants. Figure 2.6 shows the calculated reflectivity spectrum of a 1000Å DPS film on quartz using the resolution functions of POSY II and BT–7. Compare these with the data set in Figure 2.3, where the reflectivity of the same 1000Å DPS film using "ideal" resolution is shown.

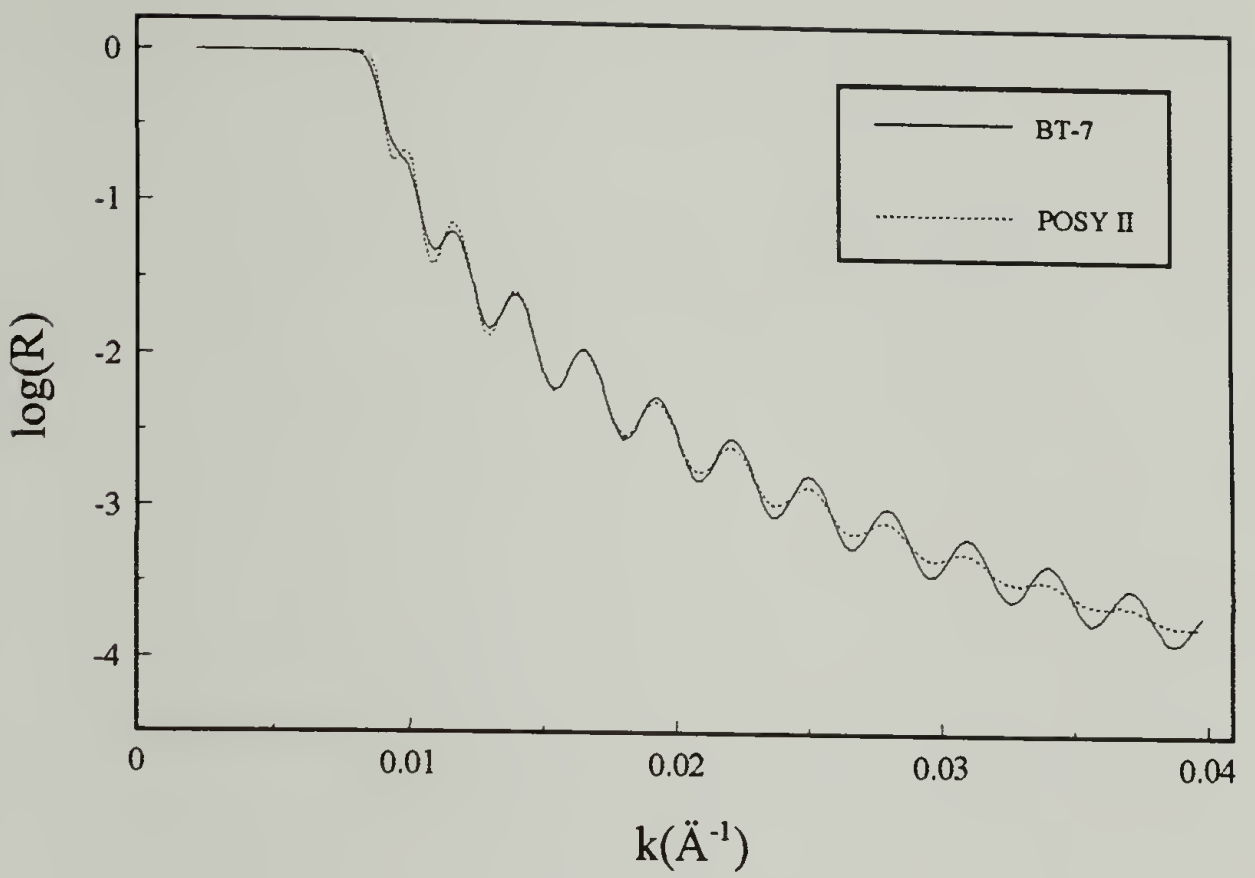


Figure 2.6 Comparison of two calculated NR data sets for a 1000Å DPS film on a quartz substrate using typical resolution functions for BT–7 and POSY II (at 0.7°). For purposes of comparison, Figure 2.3 is the calculated NR data set for the same 1000Å DPS film using ideal an "ideal" instrument.

The minima and maxima of both experimental spectra are less pronounced than in the ideal case. The reader can verify Equations 2.15 and 2.16 visually: POSY II has higher resolution at low k values (where $\Delta k$ approaches 0 rather than $C_1$) and BT–7 exhibits higher resolution at high k.

## References


[1]M. Born, E. Wolf *Principles of Optics*, 6th edition, Pergamon Press, Oxford, 1980

[2]T.P. Russell, *Materials Science Reports* **5**(4) 171-271

[3]W.D. Dozier, *Private Communication*

# CHAPTER 3

# TERMINALLY–FUNCTIONALIZED POLYSTYRENES AT THE SOLUTION–SOLID INTERFACE

## 3.1 Introduction

Specifically–functionalized polymers (SFP) are polymers of moderate (or greater) degree of polymerization with special chemical groups attached at well defined positions on the chain. The chemical groups can be chosen to interact specifically with chemical moieties on other molecules or on objects such as latex particles or inorganic substrates. One can envision SFP's of various architecture, having arrays of chemical groups (such as a graft, diblock or star block copolymer) or individual chemical groups at well defined (or random) positions on the molecule. This dissertation describes the investigation of a family of polystyrene molecules having a single carboxylic acid group attached to one end of the chain.

The addition of a single carboxylic acid group to one end of a polystyrene molecule can decrease its mobility on inorganic substrates in a thin layer chromatography experiment by several orders of magnitude.[1] This dramatic difference can be understood in terms of the relative strengths of the monomer/substrate and COOH/substrate interactions, which are 0.03kT and 6.4kT respectively for PSCOOH near $SiO_2$.[2] In the chromatography experiment cited in reference 1, the COOH group literally acts like a "ball and chain" attached to the polystyrene molecule, as shown schematically in Figure 3.1.

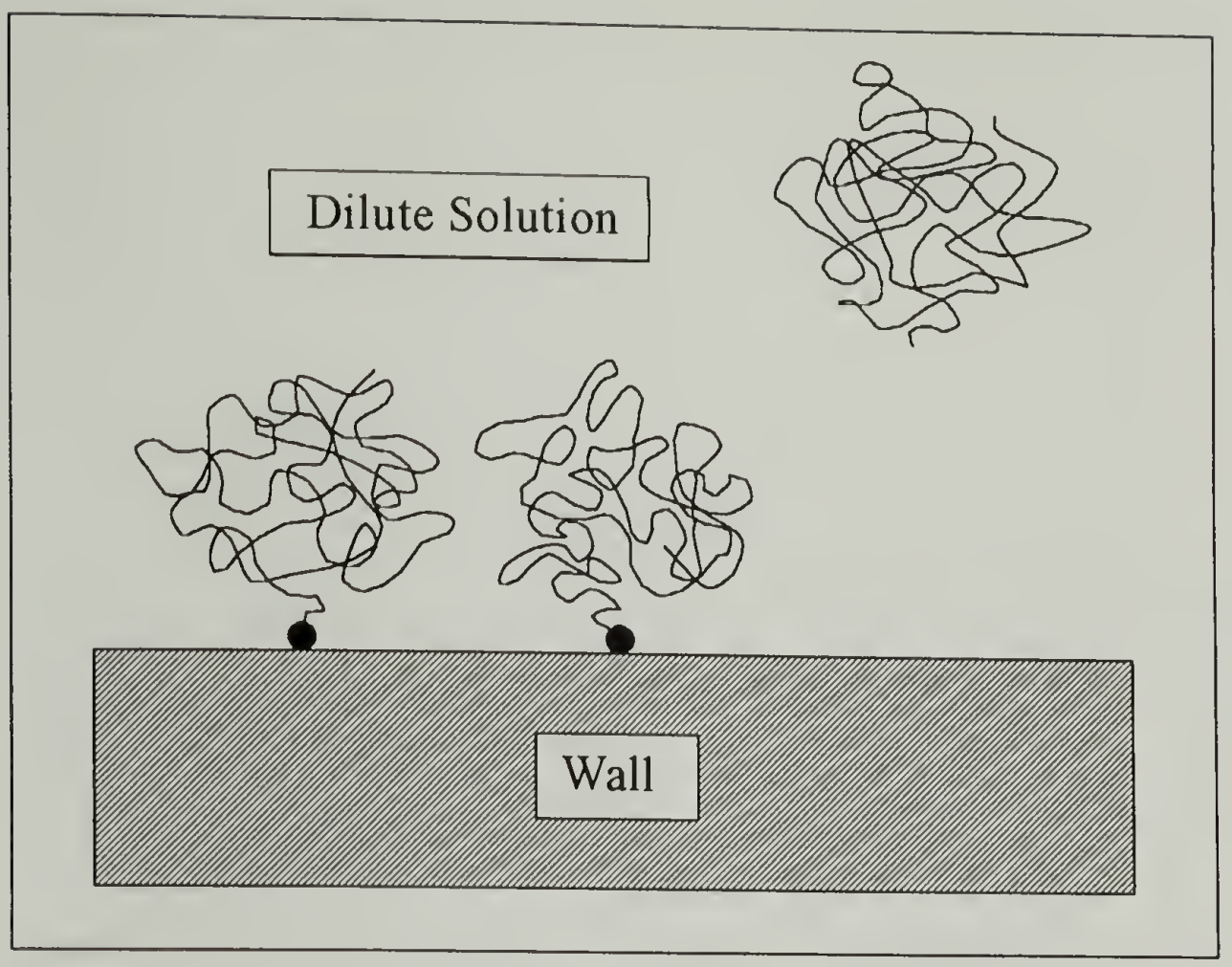


Figure 3.1 Schematic diagram of a terminally–functionalized polymer near a wall to which the plain polymer does not adsorb. The strongly interacting terminal group (depicted as the black circle) can effectively "attach" the polymer to the wall.

In the remaining sections of 3.1, we describe the scope of the experiments presented in this chapter as well as describe the experimental procedures and materials used therein. In section 3.2, relevant theoretical topics are discussed in light of terminally–functionalized polystyrenes in solutions. Experimental data and discussion are presented in sections 3.3 through 3.6 for the effects of functionalization, solvent quality, molecular weight, and isotope in the PSCOOH/cyclohexane system.

### 3.1.1 Scope of Experiments

A collection of polymer molecules attached by one end to a wall can exhibit several different types of behavior including stretching, overlap, and polymer adsorption. These are summarized schematically in Figure 3.2. While the attached chains can be "solvated" by melts or solutions, we limit discussion in this chapter to polymers at the solution/solid interface. The relevant molecular quantities governing the behavior of terminally-attached polymers are the Flory-Huggins interaction parameter $\chi$, the degree of polymerization N, the adsorption affinity of the monomers for the wall $\chi_a$, and the adsorption affinity of the functional group (in our case, a carboxylic acid group) $\chi_{foot}$.

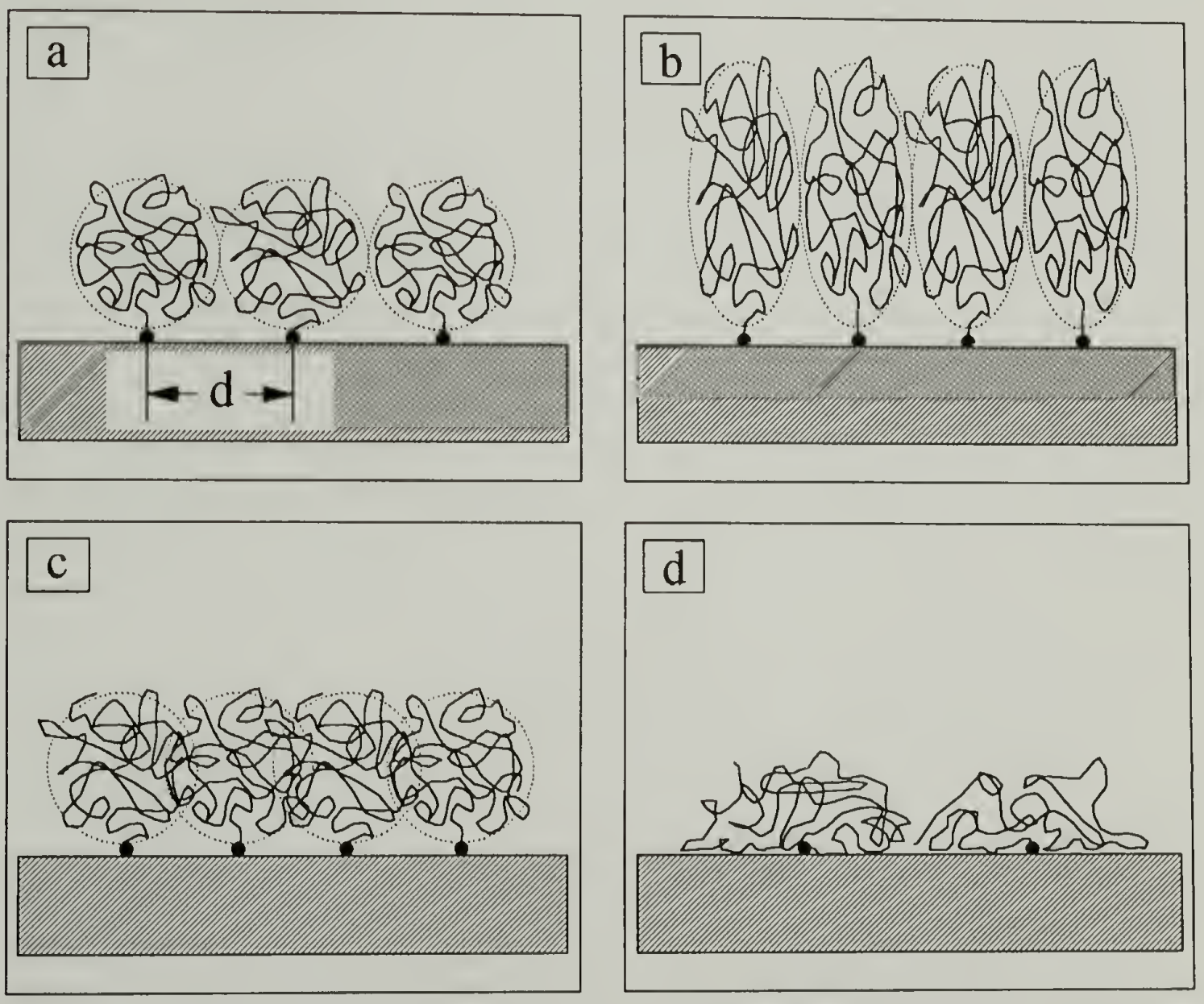


Figure 3.2 Some possible scenarios for polymer molecules attached to wall by a single functional group: a) unperturbed chains; b) stretching; c) overlap; and d) polymer adsorption.

If the average distance d between grafting sites on the wall decreases past $d \approx R_F$ (where $R_F$ is the Flory radius of the polymer in solution), the terminally attached polymers form a "brush" whereby the chains extend into solution away from the wall in much the same way that bristles extend from the base of a brush. Because d is less than the "natural" dimension of the polymer chains, $R_F$, polymer brushes are characterized by significant stretching or stretching *and* overlap. The extent to which the molecules extend into the solution is characterized by the height h of the brush. Figure 3.3 shows a typical experimentally measured concentration profile and summarizes the experimentally observable features of polymer brushes.

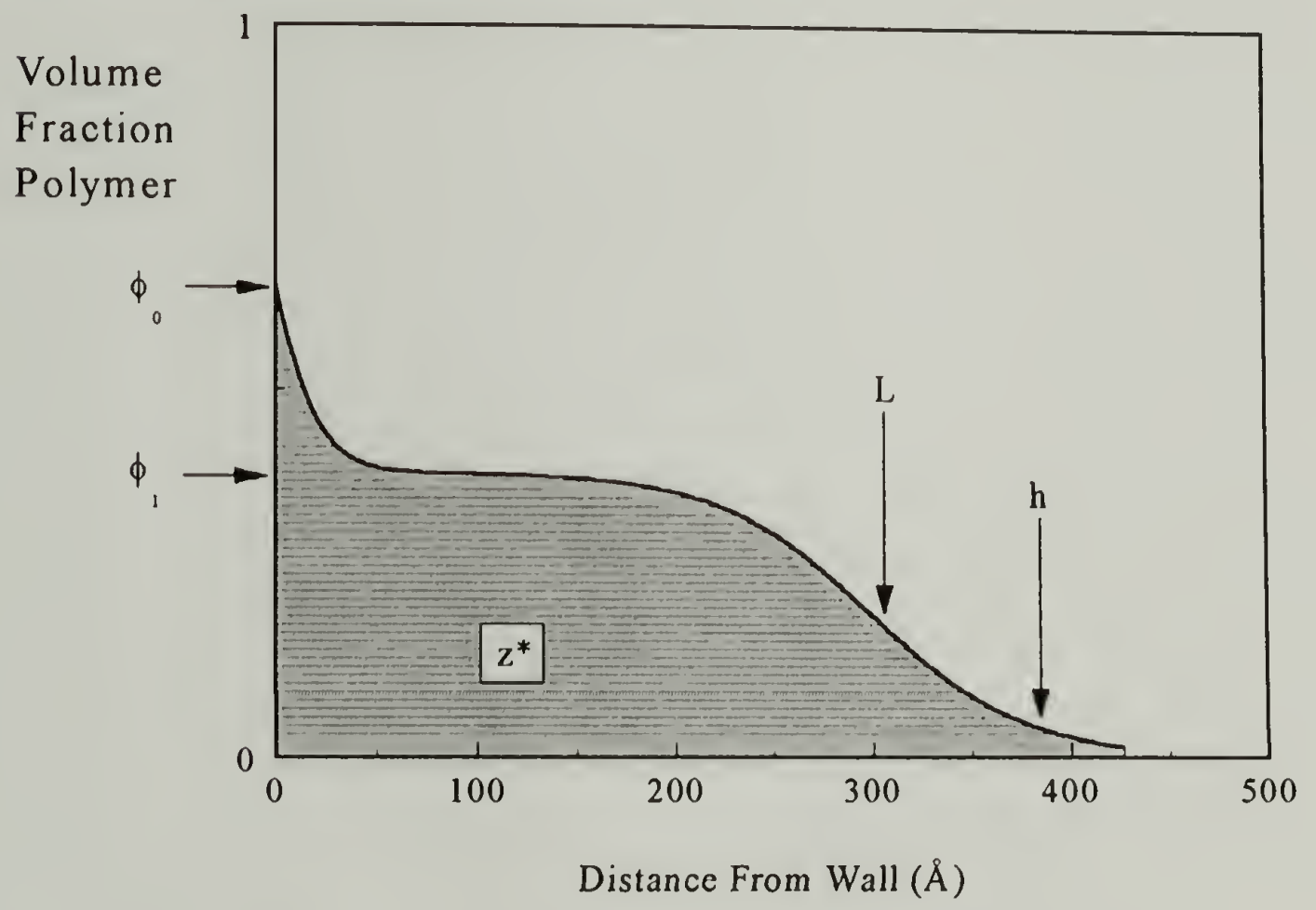


Figure 3.3 Features of brush concentration profiles which can be measured experimentally, $\phi_0$, $\phi_1$, z*, L, and h.

These features include the volume fraction polymer at the wall, $\phi_0$, the volume fraction polymer at the "plateau", $\phi_1$, the surface excess, z* (which is proportional to the normalized grafting density $\sigma$), the brush height, h, and the layer thickness L. Note that, as

long as the shape of the concentration profile of the brush does not change significantly, L ~ h $\left(\text{typically } L \approx \frac{h}{1.3}\right)$. Because neutron reflection is more sensitive to L than to h (see Chapter 2) the parameter L shall be used for all quantitative comparison with theories. Our goal is to understand these features in terms of stretching, overlap and adsorption in light of the applicable theoretical advances for polymer brushes.

The quantities shown in Figure 3.3 have the following definitions and relationships. The surface excess, z* is given by

$$z^* = \int_0^\infty dz\, (\phi(z) - \phi_\infty) \tag{3.1}$$

z* is has units of length and is proportional to the amount of adsorbed polymer. One can think of z* as the hypothetical "collapsed" thickness of the adsorbed polymer layer if the solvent were removed. The layer thickness L is given by

$$L = \frac{1}{z^*} \int_0^\infty dz\, z\, (\phi(z) - \phi_\infty) \tag{3.2}$$

The average distance d between junction points (the point at which a chain is attached to the wall) can be given by

$$d = \sqrt{\frac{NM_0}{z^* \rho_0 N_a}} \tag{3.3}$$

where $\rho_0$ is the density of the pure polymer, $N_a$ is the Avogadro number, N is the degree of polymerization of the polymer, and $M_0$ is the monomer molecular weight.

The dimensionless grafting density σ is the ratio of areas projected onto the wall of a single monomer (of size a) and the average area occupied by one chain at the wall.

$$\sigma = \frac{a^2}{d^2} = \frac{z^* a^2 \rho_0 N_a}{N M_0} \qquad (3.4)$$

Much of what was previously known about polymer brushes has come from force balance and ATR–FTIR, and ellipsometry experiments. Each of these techniques has its own advantages and disadvantages. Force balance experiments are particularly sensitive to the brush height and can provide a measure of the adsorbed amount. ATR–FTIR, and ellipsometry can provide an accurate measure of the adsorbed amount (and in the case of ellipsometry, the layer thickness L) and can be carried out in the laboratory. None of these techniques, however, can measure detailed features of the concentration profile of the adsorbed polymer such as $\phi_0$, $\phi_1$ or the shape of the concentration profile. The sensitivity of NR to these features of polymer concentration profiles makes it particularly powerful for the study of polymer brushes. Nevertheless, force balance and ATR–FTIR experiments have provided much useful information about polystyrenes at the solution/solid interface.

Force balance experiments performed by Klein have shown that PS adsorbs to mica from cyclohexane at room temperature and that polystyrene bearing substrates begin to exert mutually attractive forces at a separation s (where s is the distance between the mica substrates) on the order of $3R_g$.[3] As the s is decreased past $s \approx R_g$, the forces become mutually repulsive, increasing in magnitude with decreasing s. This behavior stands in marked contrast with that of terminally functionalized polystyrene adsorbed on mica from toluene, a good solvent for polystyrene. In this case, only mutually repulsive forces are observed. They increase monotonically with decreasing s over the interval $s \tilde{<} 6R_g$.[4]

ATR–FTIR and ellipsometry experiments have proven useful to observe the surface coverage and kinetics of formation of the enriched polymer layers in homopolymer and block copolymer systems.[5,6] While these techniques lack the spatial resolution to provide an explicit measure of the concentration profile of the adsorbed polymer layers, they can be utilized to follow the kinetics of adsorption of functionalized and non-functionalized polymers.

### 3.1.2 Description of Materials

This dissertation describes a series of experiments carried out on specifically–functionalized polymers synthesized by D. Iyengar in Prof. T.J. McCarthy's laboratory at the University of Massachusetts.[7] The polymers are polystyrenes of narrow molecular weight distribution with one of two chemical moieties (either a carboxylic acid group or a proton) on one end of the chain, and a secondary butyl group (which is part of the initiator) on the other end. The degrees of polymerization range from 67 to 788 (number average), and are shown in Table 3.1. The end capping yields for the functionalized polystyrenes is 90% or greater,[8] and indices of polydispersity are 1.10 or less for all of the polystyrenes used in these experiments.

The code names for the polymers are derived as follows: the first letter refers the hydrogen isotope present in the polymer, the number is the weight average molecular weight in $kg \cdot mol^{-1}$, and the last letter describes the chemical group on the chain terminus: C for a COOH group, and H for a proton, the terminal group for "regular" polystyrene. In this report, DPS is used as shorthand for deuterated polystyrene, and PS for polystyrene of natural isotopic abundance (i.e. $^{1}H$), and PSCOOH for polystyrene with a carboxylic acid end group.

Table 3.1 List of the family of Specifically Functionalized Polymers, their degree of polymerization and code names.

| Polymer | Degree Polymerization | Polydispersity Index | Code Name |
|---|---|---|---|
| DPS | 125 | 1.06 | D14H |
| DPSCOOH | 122 | 1.04 | D14C |
| PSCOOH | 67 | 1.10 | H7C |
| PSCOOH | 114 | 1.04 | H12C |
| PSCOOH | 220 | 1.07 | H23C |
| PSCOOH | 788 | 1.09 | H81C |

The solvents used in the experiments outlined in this chapter are cyclohexane in both $H_8$ and $D_8$ versions for the deuterated and protonated polymers, and perdeuterated toluene for H12C. The substrate is $SiO_2$, cleaned according to the procedure outlined in Section 3.1.3.

### 3.1.3 Description of Experiments

In essence, the experiment is to allow a dilute solution of the polymer $\left(c = 1.5\ \text{mg}\cdot\text{cm}^{-1} \approx \frac{c^*}{100}\right)$ in a poor or good solvent to stand in contact with a clean silicon surface with the native oxide intact (referred to hereafter as the wall), and to measure *in situ* the concentration profile of the polymer at or near the wall using neutron reflectivity (NR) after the enriched polymer layer at the wall has been saturated. The concentration was chosen so as to provide an ample reservoir of PSCOOH in the bulk, even after significant quantities of polymer had adsorbed to all surfaces of the interior of the cell. The substrate was cleaned with a $KClO_3/H_2SO_4$ etch, the purpose of which was to remove

organic impurities while leaving the oxide layer intact. The experimental arrangement is shown schematically in Figure 3.4.

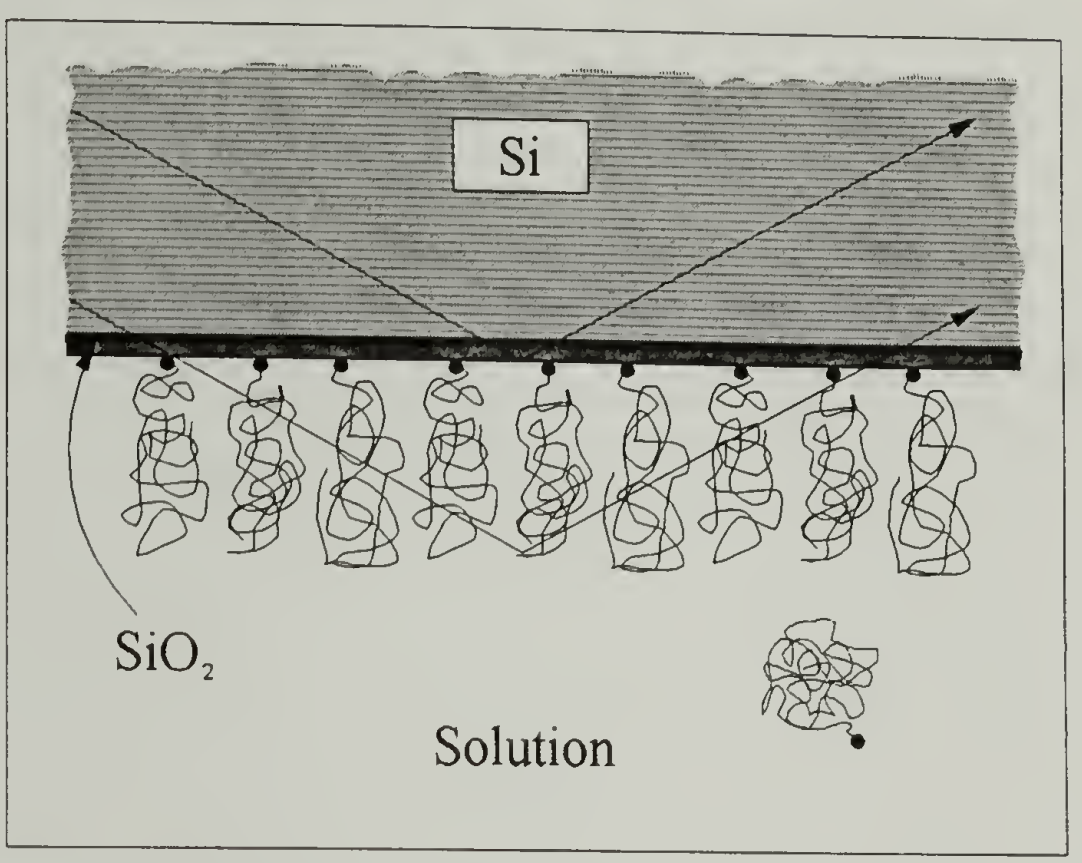


Figure 3.4 Schematic of a neutron reflection experiment wherein the concentration profile of the specifically-functionalized polymers is measured in situ.

The solution cell consists of a polished, flat single crystal of silicon 20 cm x 10 cm x 2.5 cm positioned in a fused quartz cell with polished windows on each end. (See chapter 2 and Figure 2.4 for more details). The cell and Si crystal were cleaned with toluene and then with fresh $H_2SO_4$ - $KClO_3$ solution, rinsed thoroughly with distilled water, dried in a nitrogen atmosphere, and then charged with polymer solution. The solution was allowed to incubate in the cell for 1-2 hours before the measurements were made, and remained in the cell throughout the entire (~12 hour) NR measurement. For the H12C measurement, a second NR measurement started 12 hours after the first gave, to within experimental error, the same NR spectrum. Further, a new solution (measured ~ 6 months after the original measurement) gave again, within experimental error, the same

result. For the H81C case, a second measurement made ~ 18 hours after the first gave approximately the same measurement at low k values. Thus, one cannot conclude unequivocably that the samples are at equilibrium. However, the results obtained for the lower molecular weights are stable on timescales of a few days, consisent with the observations of Motschmann and Stamm for styrene/PEO block copolymers at the solution/solid interface.[9]

The NR measurements were made on the BT-7 reflectometer at NIST. A graphite monochromator was used to select neutrons of wavelength 2.367 Å with $\frac{\Delta\lambda}{\lambda} = 0.01$. The horizontal angular resolution of the incoming beam was continuously varied from 0.015° to 0.03° during the specular scans,[10] which were done in the standard $\theta$ - $2\theta$ geometry. The background, which consists of off-specular diffuse as well as incoherent scattering, was measured by offsetting the detector from the specular condition by 0.2°, eliminating nearly all specular scattering.

The NR data were analyzed using a Levenburg-Marquardt non-linear least-squares algorithm[11] in conjunction with a computer program designed as part of this work to model NR experiments. The program is based on a recursive formalism[12] whereby the Fresnel equation is extended to a (sufficiently fine) histogram of strata of variable scattering length density. It is capable of accounting for finite instrumental resolution as well as the interfacial roughnesses encountered in the experimental situations presented in this dissertation. See chapter 2 for a complete description of the data reduction procedures.

## 3.2 Theoretical Considerations

Over the last ~20 years there has been much interest in relating the features of a polymer brush ($\phi(z)$, L, h, and $z^*$) to the molecular parameters of the system, N, $\chi$, and d. No attempt will be made in this dissertation to provide a complete account of the theoretical advances for polymer brushes, as several good reviews already exist.[13,14,15] However, the following section contains a brief overview of the theoretical advances most applicable to the experiments presented in this chapter.

The pioneering work of Alexander[16] and de Gennes[17] first established the theoretical N and $\sigma$ dependence of the polymer brush height for grafted chains in good solvents with $d < R_F$, where d and $R_F$ are the average distance between junction points and the Flory radius of the "free" polymer in dilute solution respectively. While these treatments did not give detailed information about concentration profiles (one assumption was that $\phi(z)$ remained approximately constant over $0 < z < h$), the successful prediction of the linear h dependence on N and $\sigma$ remains a landmark in the theoretical advancement of grafted polymers in the presence of solvent.

Subsequent theoretical work has refined these early simple models and extended the range of validity to a variety of molecular weights, solvent qualities, and grafting densities. Much of the subsequent theoretical work is based on self consistent field (SCF) arguments. These have been applied successfully to polymer brushes for a variety of conditions. SCF theories are a subset of a larger group of molecular theories known as mean field theories. The essence of mean field theories is that the conformation of a group of molecules (or polymer segments) can be adequately explained by the average molecular environment "seen" (or "felt") by the molecules. Hence, mean field theories are most valid when concentrations are not too low (as c decreases past $c \approx c^*$ global inhomogeneities in

concentration become strong) and for solutions not too far from theta conditions. Mean field theories have been successfully applied to polymer science problems such as the phase behavior and thermodynamics of polymer blends and solutions.[18]

SCF theories for polymers have extended the notion of mean fields theories to cases where the potential of a polymer segment can vary in real space, for example, inside the volume pervaded by an isolated polymer molecule in solution, or near an object such as a wall). In the framework of SCF theories, the local potential is itself a function of the local polymer concentration. To obtain the conformation of the polymer segments in such a field, one must place the segments into the field in such a way that their ultimate conformation is consistent with their own modification of the local potential[19,20]. While SCF approaches are valid under a wide range of experimental conditions (the restrictions are mostly the same as for mean field theories), they can presently be solved analytically for a limited set conditions. However, SCF equations can be solved numerically (on computers) using iterative approaches. Similar types of calculations can be achieved with molecular dynamics or Monte Carlo simulations. These are similar to SCF calculations in the sense that the final solution is approached iteratively during a series of computer calculations.

One of the best known analytical applications of SCF is for a collection of terminally attached polymer chains in a good solvent. If the grafting is high enough to induce strong stretching, but not so high that the dilute solution expressions for free energy lose validity (a proposition that can only be applied in the limit of large N), the concentration profile of the brush can be handled analytically[21]. These (celebrated) results indicate that the volume fraction profiles of these brushes are parabolic, of the form

$$\phi(z) = A_0 - B_0 z^2 \qquad z \leq h \tag{3.5}$$

where $A_0 \sim \sigma^{2/3} \upsilon^{-1/3}$ and $B_0 \sim \upsilon^{-1} N^{-2}$. These predictions of the N and $\sigma$ dependence of L are in agreement with the scaling arguments advanced by Alexander and de Gennes. Unlike the scaling arguments, the SCF results account for local variation of the monomer potential, thus they provide explicit information about the concentration profile of the polymer in the brush.

More recently, analytical SCF theories have been extended[22] (at a cost of much of the simplicity of the original analytical analysis) to higher grafting densities and into the theta and poor solvent regimes. However, the assumptions of very large N and strong stretching still apply. These assumptions restrict the viability of the analytical theory for brushes of moderate molecular weight, especially in poor solvents. However, these extensions to the analytical theory do appear to agree well with numerical calculations under conditions where the assumptions of the analytical theory are valid. The applicability of these analytical theories to the experimental conditions prevailing in the experiments described in this chapter is limited primarily by the assumption of high molecular weight. The (moderate) degrees of polymerization for our experimental "brushes" range from ~65 to ~800.

Halperin has used Flory arguments to predict the dimensions of irreversibly grafted polymers in theta and poor solvents.[23] The central result of this analysis is that $h \sim N^{1.0}$ for both cases, as long as the grafting density is sufficiently high ($d < R_F$, where $R_F$ is the Flory radius of the "loose" polymer in solution). The primary assumptions are that the polymer does not adsorb to the wall and that a virial expansion preserving the second and third coefficients suitably expresses the excess free energy of the grafted chains. The predictions for the dimension of the polymer brush can be summarized as

$$L \sim \sigma^{1/2} N \qquad \text{(theta solvent)} \qquad (3.6)$$

$$L \sim \sigma N |\upsilon|^{-1} \qquad \text{(poor solvent)} \qquad (3.7)$$

where $\upsilon = 0.5 - \chi$ and $\sigma = \frac{a^2}{d^2}$ where a and d are the monomer size and the average distance between grafting sites respectively. For comparison, MWC predict for similar polymer brushes in good solvent

$$L \sim \sigma^{1/3} N \upsilon^{1/3} \qquad \text{(good solvent)} \qquad (3.8)$$

Numerical realizations of SCF calculations can be invoked to address an array of experimentally accessible conditions. These approaches usually involve no implicit assumptions about molecular weight, ground state dominance (the basis of the strong stretching assumption in the analytical approaches discussed above). Thus they can be applied to systems of moderate molecular weight. Numerical approaches are, not surprisingly, more versatile, but also more complicated.

Cosgrove and coworkers published one of the earliest SCF studies of polymer brushes[24]. They considered the effect of $\chi$ and adsorption affinity, $\chi_a$, on the concentration profiles. They observed strong dependence of the volume fraction polymer at the wall ($\phi_0$) on the adsorption affinity $\chi_a$. Whitmore and Noolandi[25] (designated hereafter as WN) have done numerical SCF calculations for a range of solvent qualities, surface coverages, and degrees of polymerization. They observed that the behavior of the brush can differ considerably from the analytical result under conditions of poor solvent or moderate grafting density. They report the following relationships between L, N, and $\sigma$:

$$L \sim \sigma^{1/4} N^{4/5} \qquad \text{(theta solvent)} \qquad (3.9)$$

$$L \sim \sigma^{2/5} N^{3/5} \qquad \text{(poor solvent)} \qquad (3.10)$$

$$L \sim \sigma^{0.3} N^{>4/5} \qquad \text{(good solvent)} \qquad (3.11)$$

The probable origin of the weaker N and σ dependence of L (compare with Equations 3.6 – 3.8) is due to the (relatively) low grafting densities (σ) used in the WN calculations (approximately one order of magnitude than those observed in our experiments in poor solvents). Also included in the WN calculations are the dependence of $\phi_1$ on N and σ.

$$\phi_1 \sim \sigma^{1/2} N^{1/12} \quad \text{(theta solvent)} \tag{3.12}$$

$$\phi_1 \sim \sigma^{1/4} N^{1/8} \quad \text{(poor solvent)} \tag{3.13}$$

The N dependence of $\phi_1$ can be understood in terms of proximity to the coexistance curve. As one moves closer to the coexistance curve, the free energy penalty for overlap decreases, leading to increased $\phi_1$ values. Note that the N dependence weakens as the solvent quality improves.

In all of the theoretical work discussed in this dissertation, σ is treated as a fixed parameter. In the experiments presented in this dissertation, the polymer chains are attached *reversibly* to the wall by single COOH groups interacting with OH groups on the wall. Recall that PSCOOH adsorbed to the wall from cyclohexane can be removed with solvents such as THF. Polymer chains in dilute solution wishing to become part of the brush must 1) forfeit their translational entropy, and 2) diffuse up an osmotic gradient, the amount of work for which is determined by χ. Because the favorable COOH/wall interactions (~6.4kT) are the sole driving force for reversibly attached terminally functionalized polymers, σ is determined by χ and the foot/wall interaction.

The quantities $\phi_0$, $\phi_1$, σ, L, and d can be readily obtained from theoretical or experimental concentration profiles obtained from NR experiments and compared directly. Some features of the scattering length density profiles can be measured independently, thereby lending confidence to the NR results. In particular, z* can be measured using

ATR-FTIR, ellipsometry or FReS (in these experiments, FReS was used), and the oxide thickness and roughness using x-ray reflection.

While it is often useful to think of the chains comprising polymer brushes as grafted irreversibly to the wall, PSCOOH attaches *reversibly* to $SiO_2$ (used as the "wall" for all of the PSCOOH experiments discussed in this dissertation) under ambient conditions.[26,27] Hence, the total amount of attached polymer is expected to depend strongly on the strength of the COOH/$SiO_2$ interaction, $\chi_{foot}$, measured as $1.6 \times 10^4$ J·mol$^{-1}$ (about 6.4 kT) by Frantz and coworkers.[28]

In the Sections that follow, we present the experimental results in light of the most applicable published theoretical results. The rest of this chapter will be organized as follows. The effect of terminal functionalization on the adsorption and $\phi(z)$ of polymers in poor solvents will be presented in Section 3.3. The effects of molecular weight and solvent quality on the concentration profiles of PSCOOH brushes are presented in Sections 3.4 and 3.5 respectively. Finally, in Section 3.6 the effects of isotope on the PS/cyclohexane system are briefly discussed.

## 3.3 Effect of Terminal Functionalization

Figure 3.5 shows one manifestation of the dramatic effect that a single COOH group can exert on a polymer molecule near a wall. It shows three measured NR data sets: neat cyclohexane, D14H in cyclohexane, and D14C in cyclohexane.

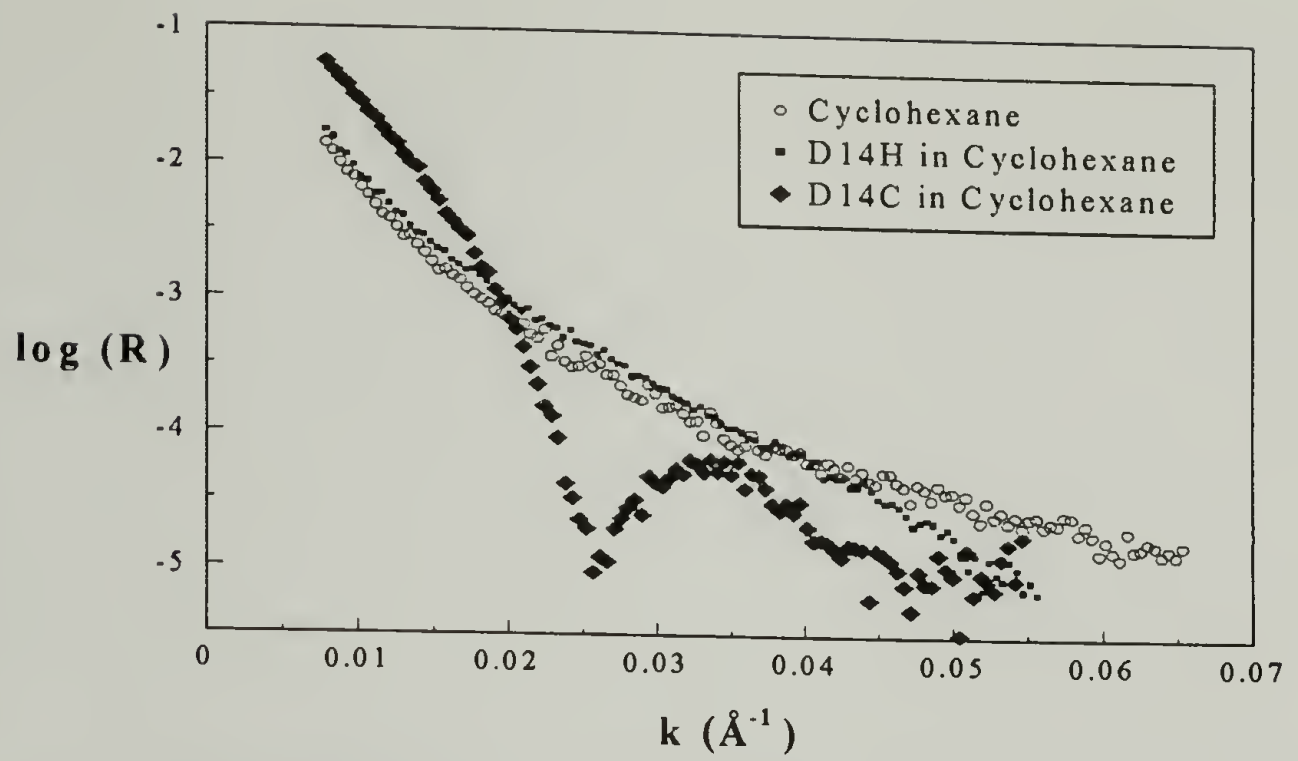


Figure 3.5 Experimentally observed NR data sets for dilute solutions of D14H and D14C, and neat cyclohexane in contact with a silicon ($SiO_2$) wall at 23°C. The "dip" in the reflectivity of D14C at $k \approx 0.026Å^{-1}$ indicates the formation of an enriched polymer layer approximately 120Å in thickness.

The most dramatic part of Figure 3.5 is the "dip" in the reflectivity of D14C at $k \approx 0.026Å^{-1}$. This dip indicates the formation of an enriched layer at the wall sufficiently "discrete" to reflect neutrons predominantly from the layer's front and back edges (its front edge is at the solution/solid interface). The k value at which the dip is observed is (predominantly) determined by the distance between the front and back edges of the layer (approximately 120Å). The sample's NR is also sensitive to specific features of the concentration profile, such as how the polymer concentration falls off near the back edge of the layer. The neat cyclohexane data, on the other hand, are featureless and are consistent with a silicon "wall" in contact with pure cyclohexane. This particular wall has an oxide layer about 15Å in thickness and a roughness of about FWHM 11Å. Detailed results of the modeling of the D14C and D14H data sets are presented below in Figures 3.6 and 3.7 respectively, where the profiles of scattering length density, $\rho_n(z)$, from which the data were calculated are shown at the insets. Note the presence of the $SiO_2$ layer

accompanied by a monolayer of water, corresponding to the leftmost swell and depression respectively in the plot of $\rho_n$ vs z at the inset. The boundaries of the oxide appear rounded as a result of the modeling of the interfacial roughness (see section 2.4).

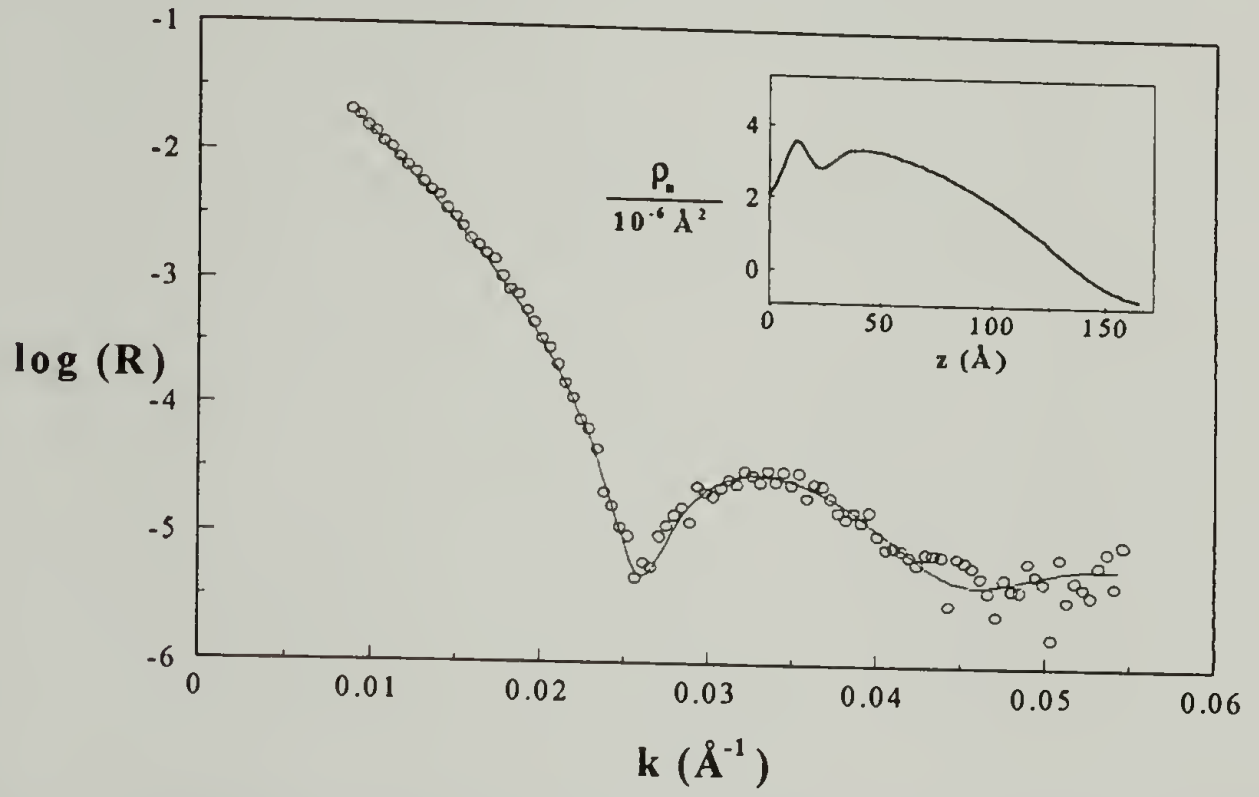


Figure 3.6 Comparison of calculated and observed NR for D14C in cyclohexane at the solution/$SiO_2$ interface. The calculated NR was calculated using the profile of scattering length density shown at the inset. The oxide and a monolayer of water can be seen in the $\rho_n$ profile at the inset as a local maximum and minimum at $z \approx 10$ Å and 20 Å respectively. The polymer concentration profile obtained from $\rho_n$ vs z is shown in Figure 3.8.

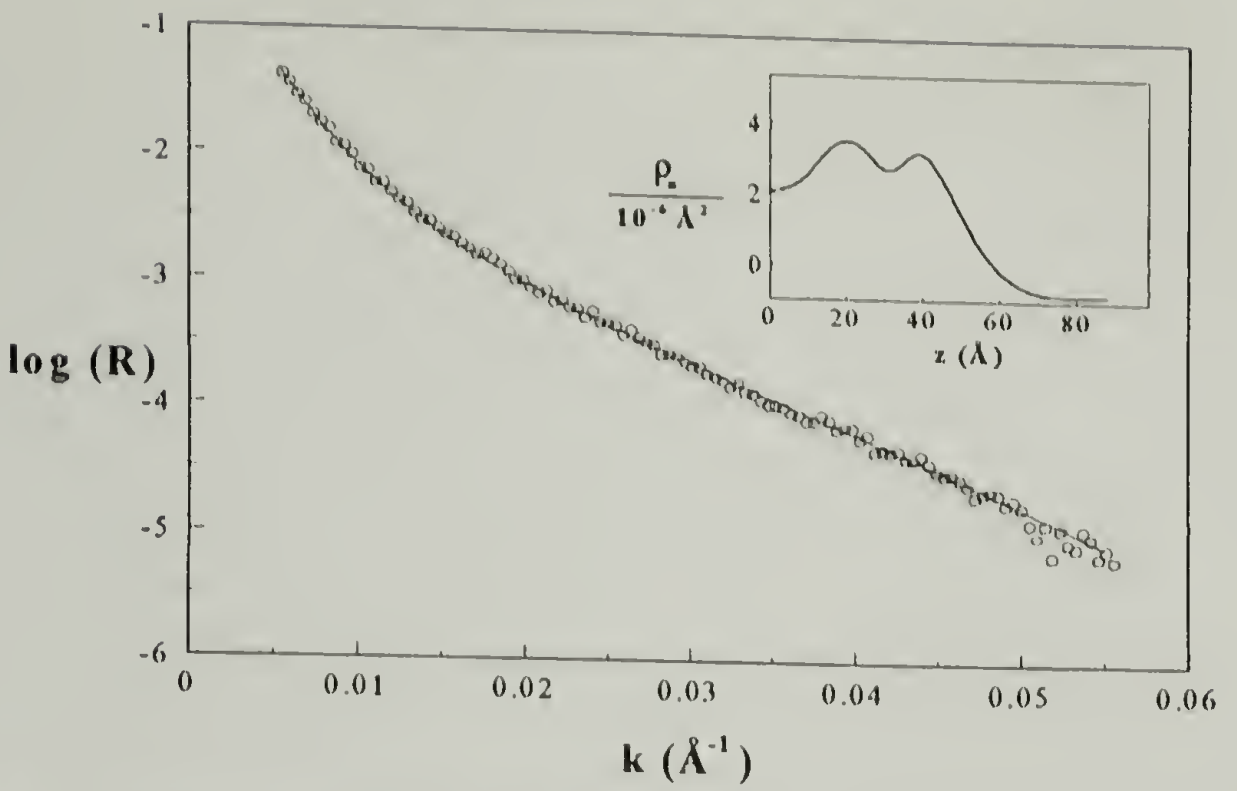


Figure 3.7 Comparison of calculated and observed NR for D14H in cyclohexane at the solution/$SiO_2$ interface. The calculated NR corresponds to the profile of scattering length density shown at the inset. The oxide and a monolayer of water can be seen in the $\rho_n$ profile at the inset as a local maximum and minimum at $z \approx 20$ Å and 30 Å respectively. The polymer concentration profile obtained from $\rho_n$ vs z is shown in Figure 3.8.

The volume fraction profiles of D14H and D14C from which the profiles of $\rho_n$ in the insets of Figures 3.6 and 3.7 were calculated are shown in Figure 3.8.

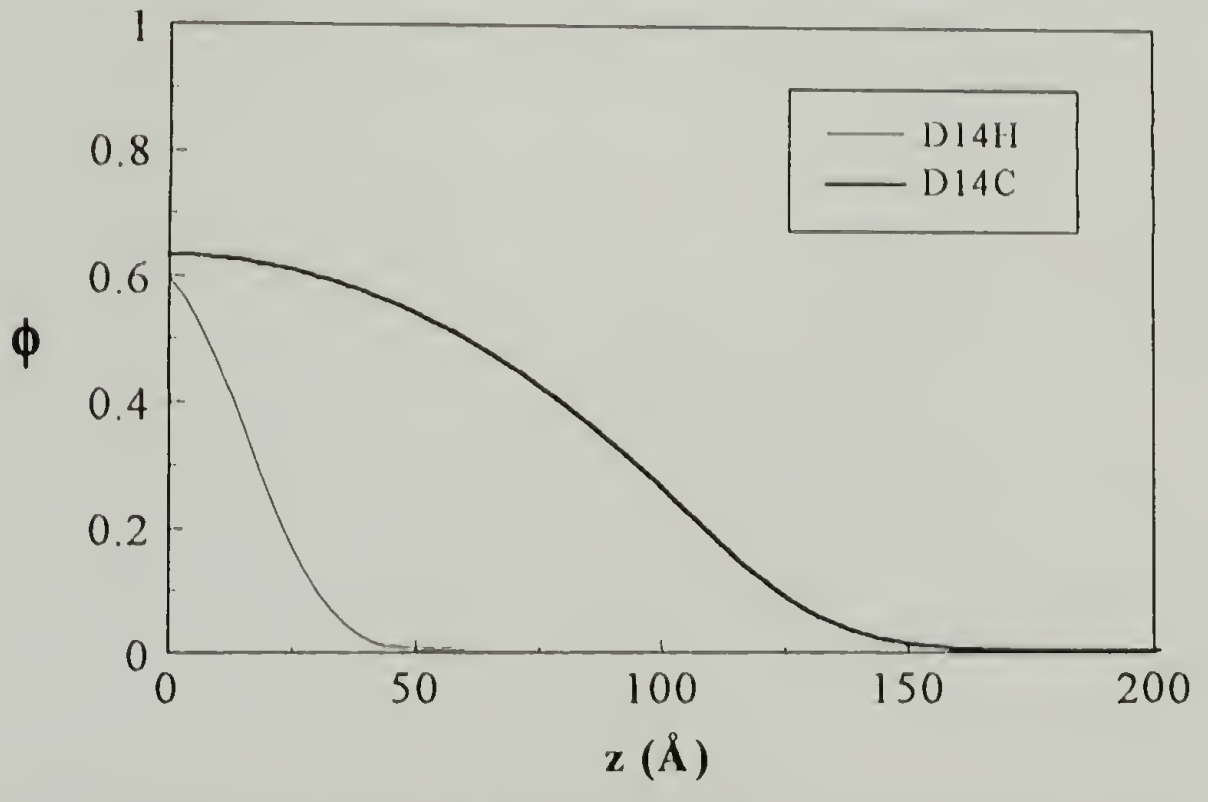


Figure 3.8 Comparison of volume fraction profiles of D14H and D14C in cyclohexane at the solution/$SiO_2$ interface. The ~fourfold increase in z* and L for D14C is caused by a single COOH group on one end of the D14C chain.

The layer thickness L (see Equations 3.2 – 3.5) of the D14H at the wall is 24Å, slightly smaller than its ideal $R_g$ (32Å). Therefore the D14H at the wall is not strongly perturbed from its ideal dimensions. On the other hand, the layer thickness L of D14C is 105Å, some 4.7 $R_g$. FRES experiments on rinsed films of H12C indicate that the COOH-bearing polymer remains on the wall after rinsing, leading to the conclusion that the D14C molecules are attached to the wall by their end groups, as opposed to merely "piled on" one another at the wall. The average distance d between junction points (assuming that the COOH group of each molecule is in contact with the wall) of D14C is 19.8Å, compared with its "Flory radius" of 32Å. Thus, $d < R_F < L$, placing D14H in the regime described by Halperin[29] for a polymer brush in a poor solvent. The (hypothetical) d value for D14H is 41.5Å, calculated from the (smaller) number of chains per unit area of the wall. The COOH group on the D14C chains increases by a factor of ~4 the adsorbed amount and the thickness of the adsorbed DPS layer.

The concentration profile of D14H was modeled using the parabolic form expressed in Equation 3.5 modified by introducing rounding in the tail by convolution with a slowly varying Gaussian function (FWHM = 16 Å at z = L). While a parabolic profile is predicted for high N in good solvents, it provides a reasonable description (within experimental error) of D14C in cyclohexane, a brush of moderate N in a poor-to-theta solvent. This parabolic form of the concentration profile of terminally attached polymers in theta and poor solvents is also qualitatively consistent with the numerical SCF calculations published by several other researchers.[30,31,32]

While the differences between D14C and D14H are dramatic, there is one significant similarity. $\phi_0 \approx 0.6$ for the functionalized *and* "regular" deuterated polystyrenes. It is obvious that the monomer adsorption affinity $\chi_a$ determines $\phi_0$ for D14H, one would not necessarily expect that it would generally determine $\phi_0$ for D14C. Therefore, the

volume fraction polymer at $z \approx 0$ is most sensitive to the polymer adsorption affinity under the conditions prevailing for these samples: $\phi_0$ for the "regular" polymer is greater than (or equal to) $\phi_1$ for the functionalized polymer. Similar results can be observed in the H81C concentration profile presented in Section 3.5.

## 3.4 Molecular Weight Effects

The analytical and numerical SCF theoretical results presented in Section 3.2 uniformly predict strong N dependence of L and the weak N dependence of $\phi_1$. The thickness L of the adsorbed layer is directly determined by the dimension of the stretched chains, which varies linearly with N when $d < R_F$. This has been confirmed experimentally.[33]

Experimental NR data for four molecular weights of PSCOOH are shown in Figures 3.9 through 3.12. These are for 1.5 mg·ml$^{-1}$ solutions of PSCOOH having degrees of polymerization 67, 114, 221, and 788 in d-cyclohexane at 23°C, some 17° below the theta temperature. Again, the profiles of scattering length density $\rho_n$ corresponding to the calculated NR data sets are shown at the insets. Further, the concentration profiles (from which the $\rho_n$ profiles were calculated) for each of the four data sets are shown in Figure 3.13, with the key results summarized in Table 3.2. The errors presented therein are the 95% confidence limit i.e. there is a 95% chance that the actual parameter falls in the range expressed, as calculated using standard statistical experiments.[34] See Appendix A for discussion of the functional forms of the concentration profiles used in modeling the PSCOOH data.

The primary change in the NR with increasing N is a decrease in the period of the oscillations. In the H7C case, the period is so large that a clear minimum in the reflectivity is not observed on the experimentally accessible k range. For H12C, a single minimum is

present, while two minima can be plainly observed for the H23C and H81C cases. The decrease in the oscillatory period $\Delta k$ with increasing degree of polymerization is directly caused by increased adsorbed layer thicknesses according to $\Delta k = \frac{\pi}{L}$.

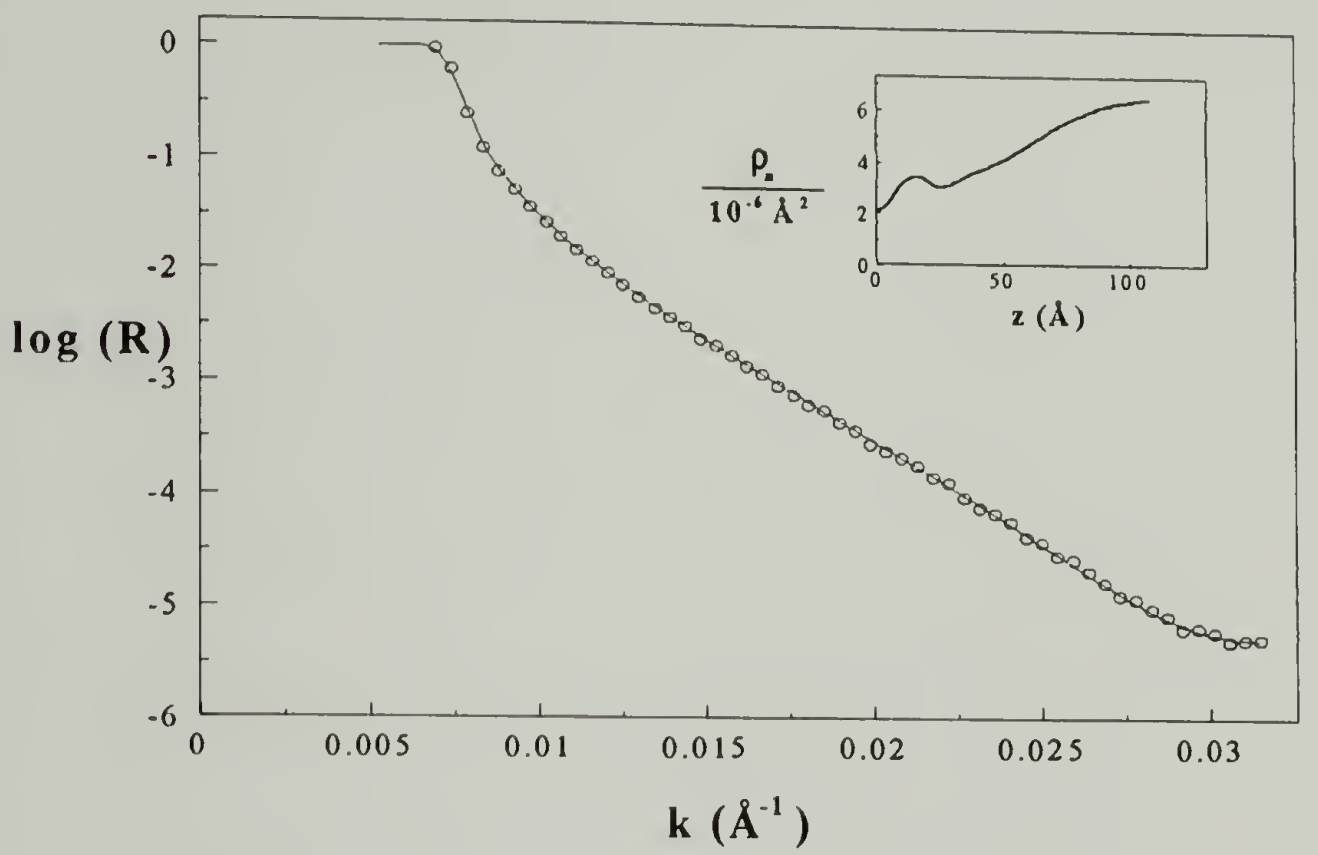


Figure 3.9 Comparison of calculated and observed NR for H7C in d-cyclohexane at the solution/$SiO_2$ interface. The calculated NR corresponds to the profile of scattering length density shown at the inset. The relative maximum and minimum at $z \approx 20$ Å and 30 Å in the $\rho_n$ vs z profile correspond to the oxide and a monolayer of water respectively.

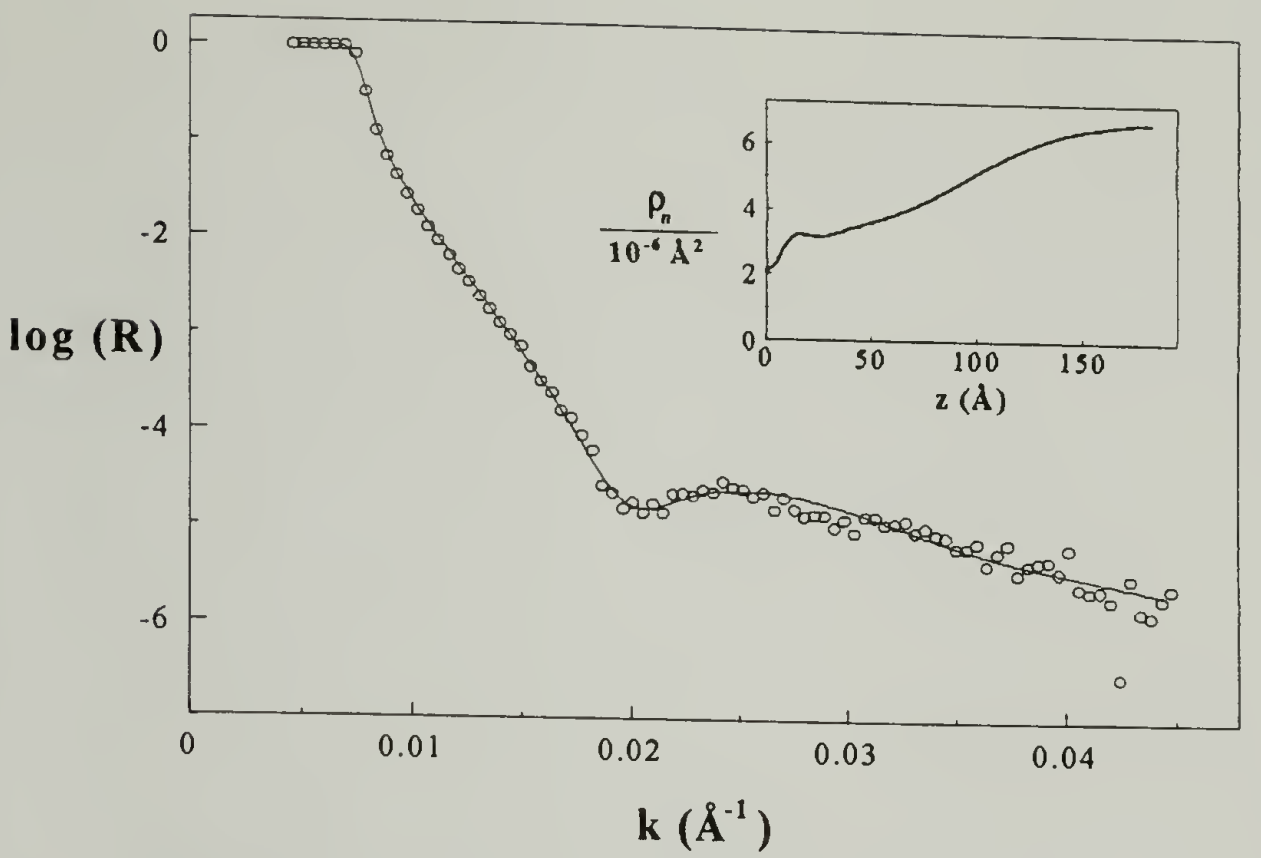


Figure 3.10 Comparison of calculated and observed NR for H12C in d-cyclohexane at the solution/$SiO_2$ interface. The calculated NR corresponds to the profile of scattering length density shown at the inset. The "dip" in the reflectivity at k ≈ 0.02 Å$^{-1}$ corresponds to an enriched polymer layer ~ 90 Å in thickness.

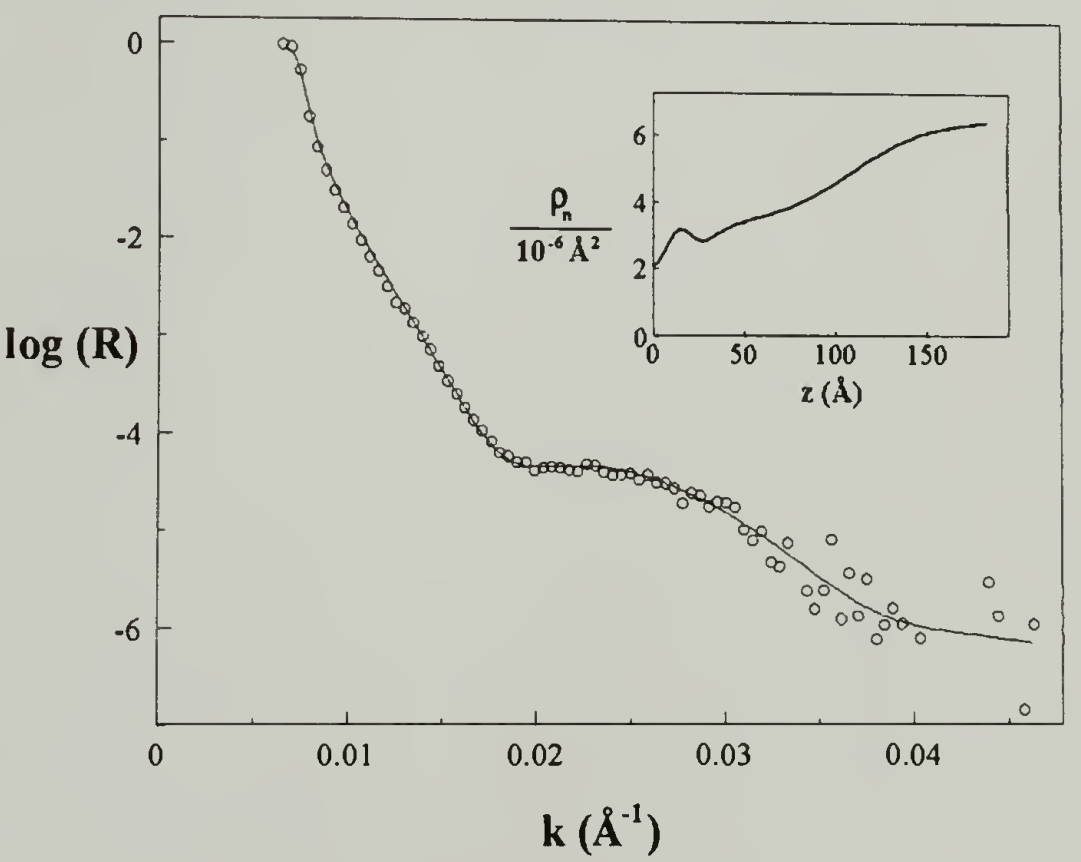


Figure 3.11 Comparison of calculated and observed NR for H23C in d-cyclohexane at the solution/$SiO_2$ interface. The calculated NR corresponds to the profile of scattering length density shown at the inset. The "dip" in the reflectivity at k ≈ 0.018 Å$^{-1}$ corresponds to an enriched polymer layer ~ 100 Å in thickness.

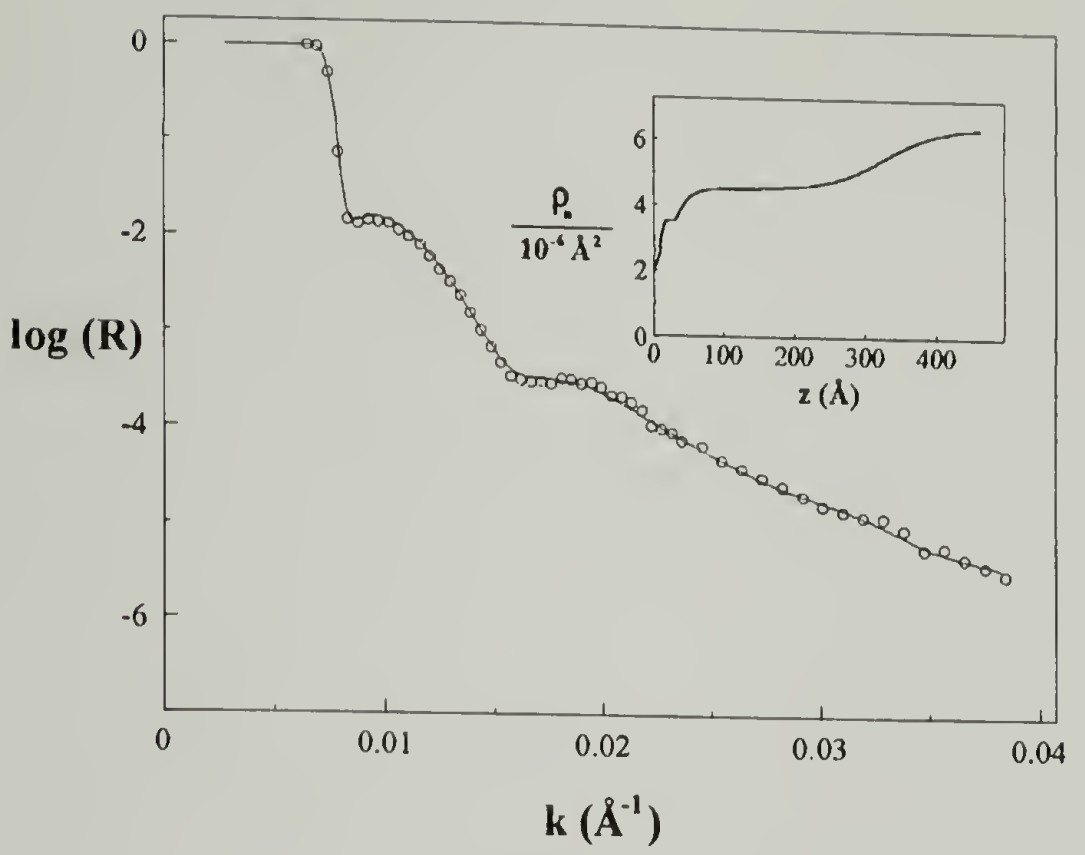


Figure 3.12 Comparison of calculated and observed NR for H81C in d-cyclohexane at the solution/$SiO_2$ interface. The calculated NR corresponds to the profile of scattering length density shown at the inset. The "dips" in the reflectivity at k ≈ 0.008 Å$^{-1}$ and k ≈ 0.015 Å$^{-1}$ correspond to an enriched polymer layer ~ 310 Å in thickness.

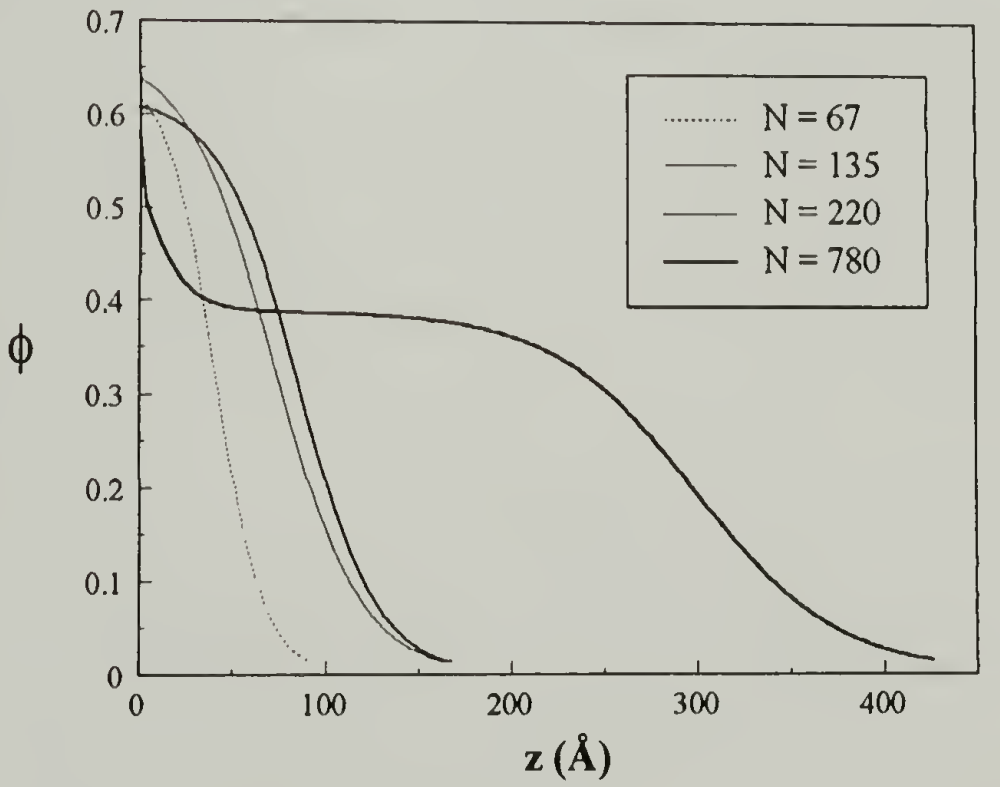


Figure 3.13 Volume fraction profiles of H7C, H12C, H23C and H81C in d-cyclohexane at the solution/$SiO_2$ interface as measured by NR.

Table 3.2 Summary of the essential features of the concentration profiles of the PSCOOH family.

| Polymer | N | L (Å)† | $\phi_1$† | d (Å)† | σ† |
|---|---|---|---|---|---|
| H7C | 67 | 51±1.2 | .62±.02 | 20±1.8 | 0.062±0.005 |
| H12C | 114 | 92±1.0 | .64±.01 | 21±1.4 | 0.056±0.005 |
| H23C | 220 | 100±1.1 | .61±.01 | 26±1.8 | 0.037±0.004 |
| H81C | 788 | 306±3.7 | .39±.01 | 33±4.3 | 0.023±0.002 |

†95.4% confidence limits.

Assuming $\chi$ is held constant, the data of this molecular weight series are best described by the relationship

$$L \sim \sigma^{0.73} N^{1.0} \qquad (3.14)$$

Because the analysis using Equation 3.14 is based on only 4 points, one cannot conclusively establish the scaling behavior of this system. However, this result falls between the scaling behavior for theta and poor solvents respectively, predicting dependence of $\sigma^{0.5}$ and $\sigma^{1.0}$ respectively. This behavior seems reasonable for the PS/d-cyclohexane system at 23°C, where $\chi = 0.53$.[35] The behavior observed by Whitmore and Noolandi exhibits significantly weaker σ and N dependence of L (see Equations 3.9 and 3.10). However, their results were for significantly smaller surface coverages than observed for PSCOOH in d-cyclohexane. Again, this seems reasonable as their exponents fall between Equations 3.5 and 3.6 and that of isolated chains. One cannot, on the basis of the limited number of samples presented in this chapter conclusively confirm scaling behavior. However, taken as a guide, the theoretical predictions are in good agreement with our results for the PSCOOH/cyclohexane system.

The dependence of $\phi_1$ on $\sigma$ and N for the experimenta data sets here does not lend itself well to scaling analysis. Qualitatively, however, the $\sigma$ dependence of $\phi_1$ is much stronger than the N dependence, in accord with all of the theoretical results discussed in this chapter. $\phi_1$ is determined primarily by $\sigma$, which is in turn determined primarily by $\chi$. Therefore, for a more complete discussion of the $\chi$ dependence of $\phi_1$ for these polymer brushes is postponed until Section 3.5.

It is desirable to compare these experimental results with the relevant analytical SCF theory. One problem with the extension of analytical theories to poor solvents is the assumption of large degree of polymerization (N approaching infinity). Thus, these theories predict discontinuities in the concentration profile as soon as the theta threshold is crossed. However, it might be useful to compare the observed and calculated results under conditions of constant $\chi_s$ - $\chi$. Figure 3.14 shows just such a comparison between the measured H81C data set (this comes closest to the theory's assumptions) and the analytical theory of Zhulina and coworkers[36] adapted to conditions of $\chi_s$ - $\chi$ = 0.035.

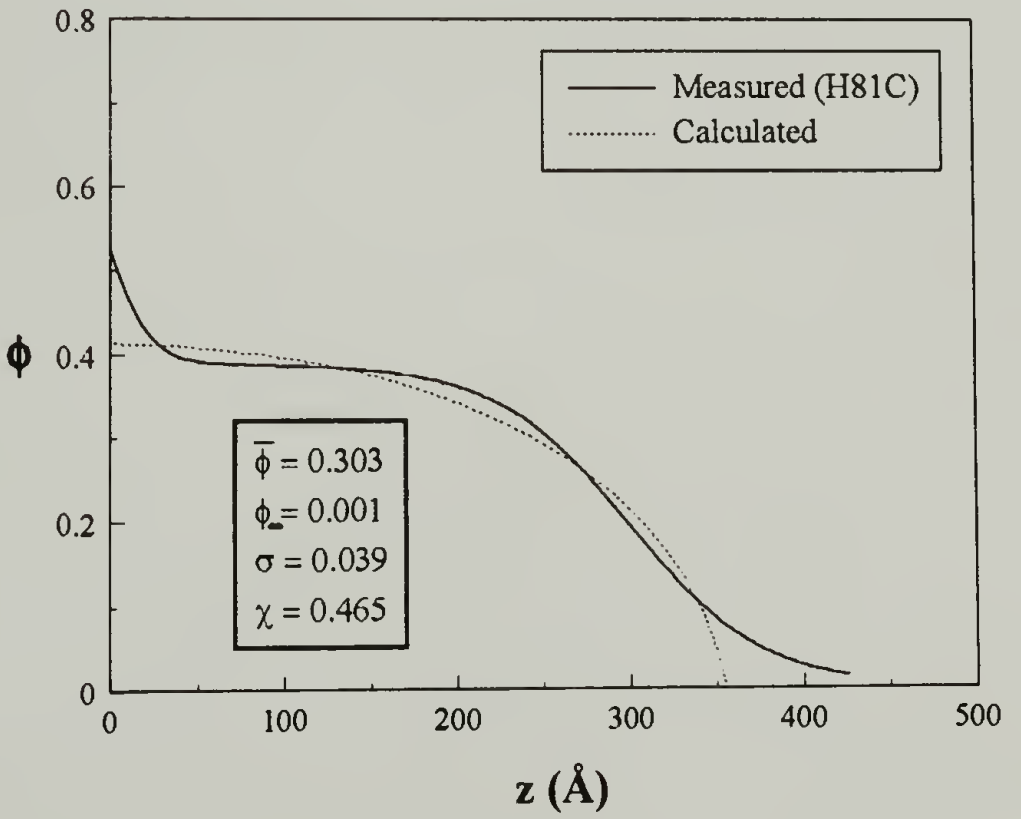


Figure 3.14 Comparison of calculated and measured volume fraction profiles for H81C in cyclohexane. The dotted line is calculated from the theory of Zhulina and coworkers, using the parameters shown in the box at the lower left corner. (Reference 35).

The agreement between the data sets is best in the intermediate z region away from the wall and "tail" of the profile. Close to the wall, $\phi_0$ for H81C is not unlike $\phi_0$ of the other molecular weights, providing additional evidence that $\phi_0$ is driven by $\chi_a$. At large z, the experimental data set changes concavity and exhibits pronounced "rounding" compared to the theoretical result. This can be understood by examining one of the assumptions of the theory, i.e. that strong stretching prevails at all locations in the brush. This assumption is more valid at low and intermediate z values than it is near the tail, where the volume fraction polymer is low. Similar rounding at the tail for brushes of moderate molecular weight has been widely observed for a variety of SCF and Monte Carlo calculations.

On the time interval of 2 hours to ~20 hours, the NR of the H81C changed slightly, though this change was small compared to the changes during the first 2 hours. Thus, one must face the possibility that the H81C brush was not at equilibrium during the NR measurement.

## 3.5 Effect of Solvent Quality

In dilute athermal polymer solutions ($\chi = 0$), the mutual interactions between polymer molecules are unfavorable. These unfavorable interactions, often called excluded volume interactions, are of entropic origin because the overlapping of chains decreases the entropy of the system. The chains in polymer brushes stretch (thereby decreasing their lateral dimension) in order to relieve their excluded volume interactions with their neighbors. The free energy penalty (due to excluded volume interactions) for overlap is determined by the Flory-Huggins interaction parameter $\chi$. Therefore, the extent of overlap in polymer brushes depends strongly on $\chi$.

Consider the course of events for the formation of a PSCOOH brush from an initially bare wall in contact with dilute solution. Recall that the chains in these experiments attach *reversibly* to the wall (PSCOOH molecules attached to a $SiO_2$ wall from cyclohexane can be removed by solvents such as THF[37]). The initial formation of the brush proceeds readily (the chains lose only their "translational" entropy as they attach) until $d \approx R_F$, corresponding roughly to part a of Figure 3.2. The attachment of additional PSCOOH requires stretching or overlap (or both) of the PSCOOH chains. Because the molecular parameter $\chi$ determines the free energy penalty for overlap, it determines the state of overlap in the "finished" brush. The chains can also stretch, reducing their lateral dimension to relieve the unfavorable lateral interactions in the collection of overlapped chains forming the brush. The stretching of the chains in the brush is a reflection of the total magnitude of the excluded volume interactions in the brush and must ultimately be balanced by the energy of the foot/wall interaction, governed by $\chi_{foot}$. Therefore, $\phi_1$ is determined by $\chi$, and L is determined by $\chi_{foot}$.

For polymer molecules attached reversibly to a wall, The qualitative $\sigma$ dependence is obvious. Higher grafting densities lead to higher polymer volume fractions at the wall. $\sigma$, in turn, depends primarily on $\chi$, which "sets" the free energy for polymer overlap. As overlap becomes more expensive (corresponding to decreasing $\chi$), the relative cost of stretching decreases, and the polymer brush adopts a stretched state having low polymer volume fractions at all z values. As overlap becomes cheaper (increased $\chi$) the driving force for stretching is decreased and the polymer therefore resides, on average, closer to the wall. The sensitivity of $\phi_1$ to $\chi$ increases with increasing $\chi$ as shown by Equations 3.11 through 3.13. The most applicable numerical SCF results are those of Whitmore and Noolandi, who obtained $\sigma$ dependence of 0.25 to 0.5 and weak N dependence. Again, the weaker $\sigma$ dependence observed by WN can probably be explained by the lower graft densities in the WN results.

We now present the results of experiments done with H12C in three solvents: poor (d-cyclohexane at 23°C), theta (d-cyclohexane at 40°C) and good (d-toluene at 23°C). Figures 3.15, 3.16, and 3.17 show comparisons of observed and calculated NR for H12C in d-cyclohexane at 23°C, d-cyclohexane at 40°C, and d-toluene respectively. The profiles of scattering length density corresponding to the calculated NR data are shown at each inset, and the resulting volume fraction profiles are compared in Figure 3.18.

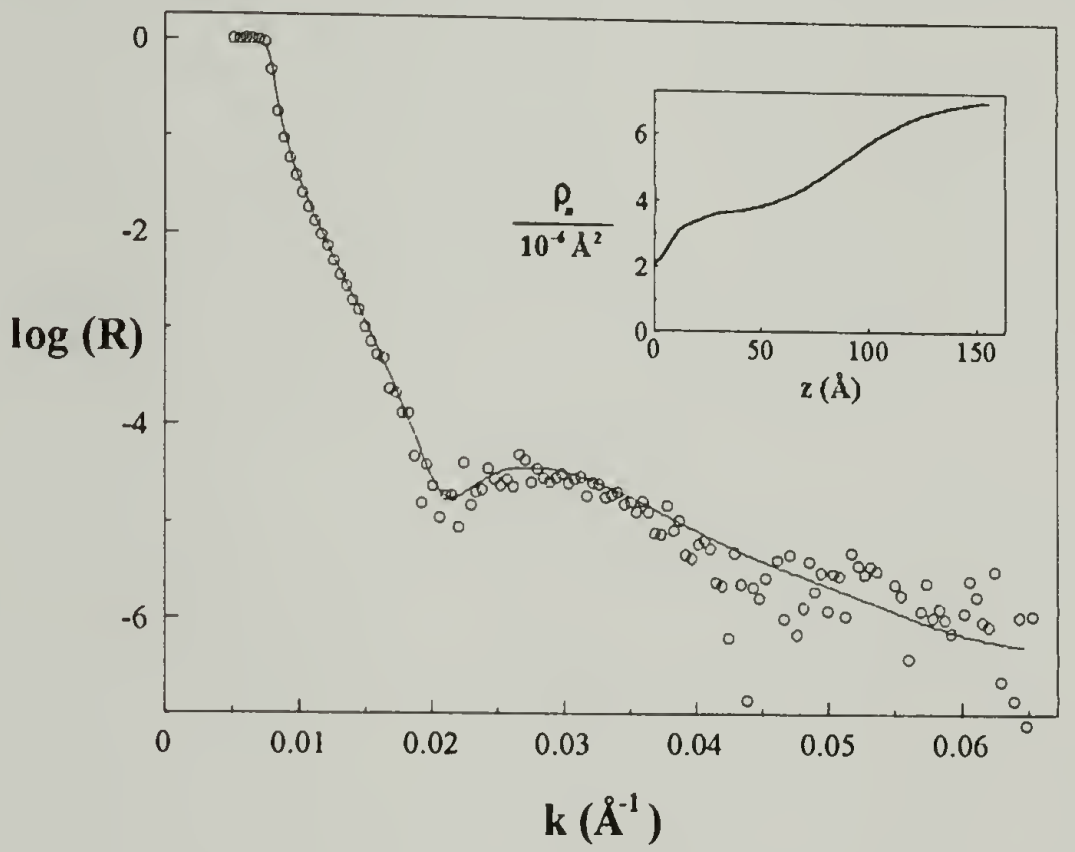


Figure 3.15 Comparison of calculated and observed NR for H12C in d-cyclohexane at 23°C (poor solvent). The calculated NR corresponds to the profile of scattering length density shown at the inset.

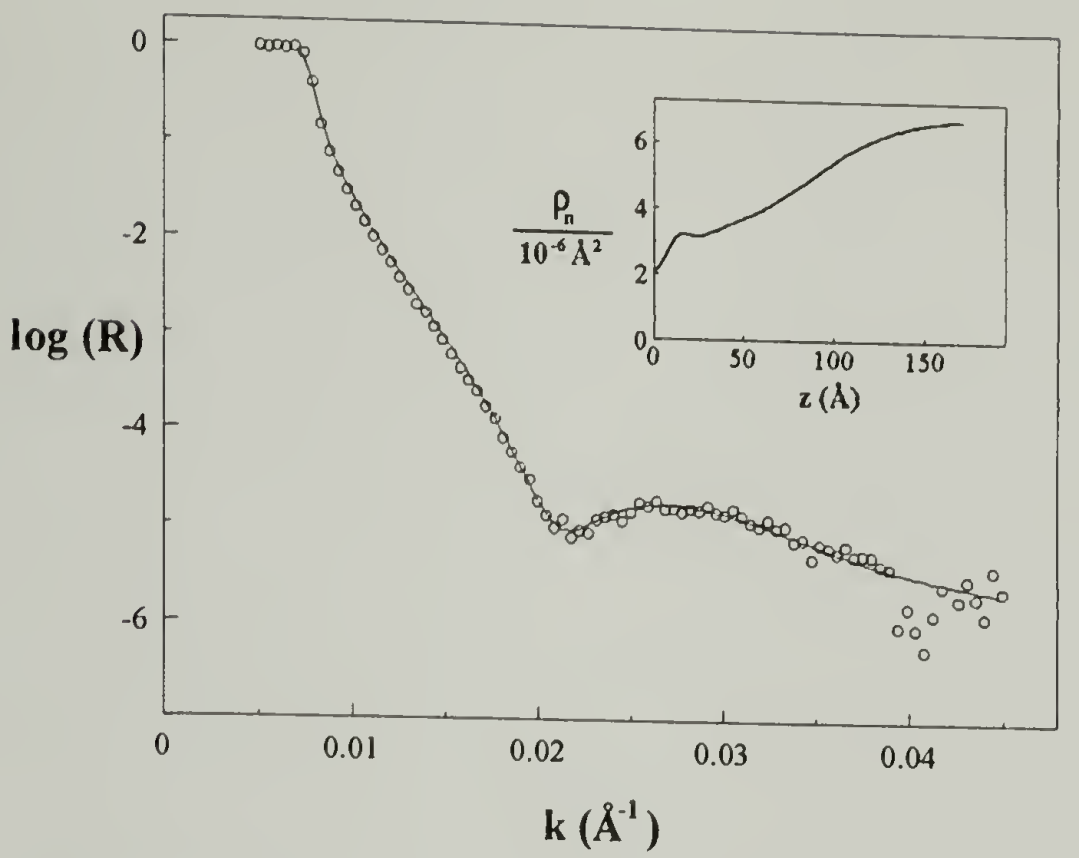


Figure 3.16 Comparison of calculated and observed NR for H12C in d-cyclohexane at 40°C (theta temperature). The calculated NR corresponds to the profile of scattering length density shown at the inset.

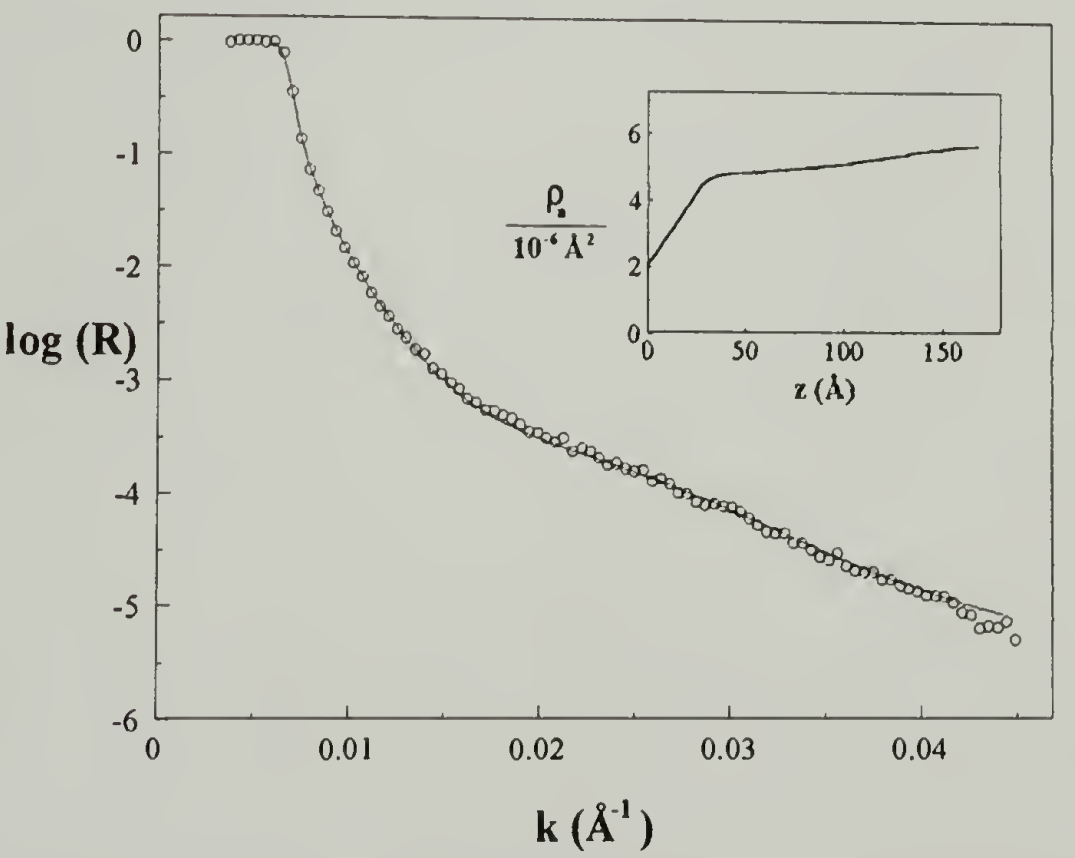


Figure 3.17 Comparison of calculated and observed NR for H12C in d-toluene. The calculated NR corresponds to the profile of scattering length density shown at the inset.

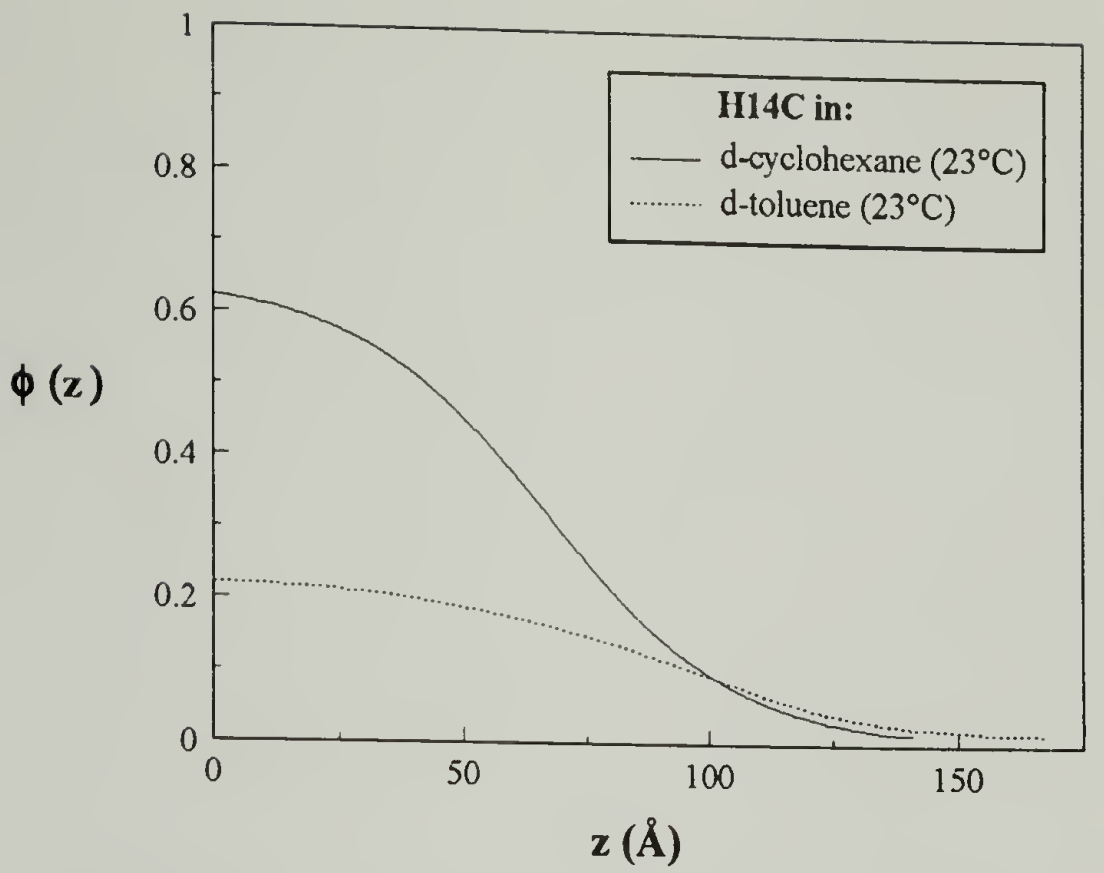


Figure 3.18 Comparison of volume fraction profiles of H12C in good and poor solvents (toluene and d-cyclohexane respectively) as measured by neutron reflection.

Data at 40°C were also taken after filling the cell at 23°C and then allowing it to incubate for 2 hours. While we cannot include this data set in the calculations of scaling relationships, etc., it is interesting that $\phi(z)$ is virtually the same as that in the poor solvent case. The conditions prevailing during the incipient filling period determined the total amount of polymer attached to the wall, suggesting that times on the order of 12 hours are not sufficient for equilibration.

One interesting result of this section is the similarity of L values for all three solvent qualities. While $\phi_1$ varies strongly with $\chi$, L remains nearly constant for PSCOOH. These results provide some of the first evidence that the thickness of the adsorbed layer for reversibly attached polymer chains may actually determined by $\chi_{foot}$, through its control of the grafting density. See Equations 3.9 - 3.11.

## 3.6 Isotope Effects in the Polystyrene/Cyclohexane System

Figure 3.19 shows a comparison of the H12C and D14C volume fraction profiles.

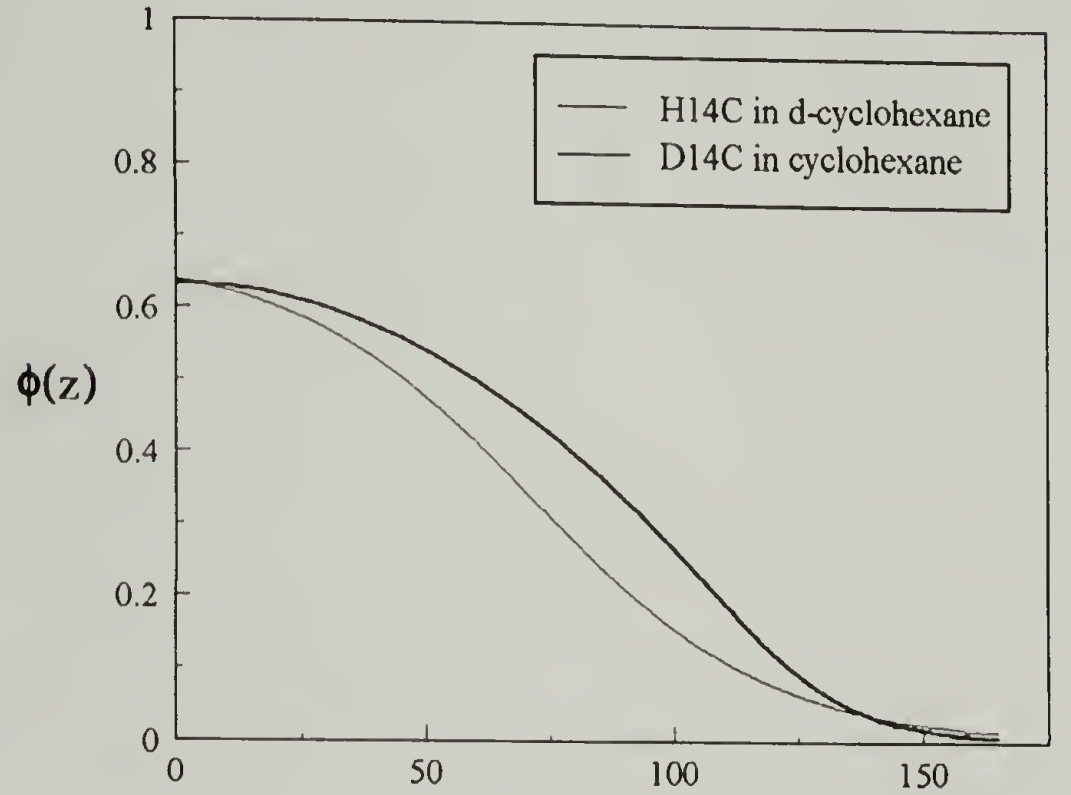


Figure 3.19 Comparison of volume fraction profiles of H12C and D14C as measured by neutron reflection.

D14C's L and z* values are both about 15% greater than H12C's. This is consistent with the differences in the degrees of polymerization, which are 122 and 114 respectively. Hence, the overall agreement between isotopes is quite good, as one would expect for two polymer brushes in thermodynamically similar solvents (the $\chi$ values are 0.53 and 0.51 for D14C in cyclohexane and H12C in d-cyclohexane respectively)[38]. Thus, the isotope effect on physical quantities of polymer brushes in this system is not strong.

## 3.7 Conclusions

The contents of this chapter have shown that terminally functionalized polystyrenes form enriched layers at the solution/$SiO_2$ interface. These enriched layers exhibit concentration profiles consistent with current theoretical descriptions of "polymer brushes". These layers have concentration profiles which are parabolic or near-parabolic in form and exhibit thicknesses on the order of 4Rg when the functional group is a carboxylic acid. The height of the brushes is proportional, to within experimental error, to the degree of polymerization of the polymer.

## References


[1]Iyengar, D.R. and T.J. McCarthy *Macromolecules* **23** 4344 (1990).

[2]P. Frantz, D.C. Leonhardt, and S. Granick *Macromolecules* **24** 1868 (1991).

[3]J. Klein *Nature* **288** 248 (1980).

[4]H.J. Taunton, C. Toprakcioglu, L.J. Fetters, and J. Klein *Nature* **332** (21) 712 (1988).

[5]S. Granick *Macromolecules* **23** 4344 (1990).

[6]H. Motschmann, M. Stamm, and Ch. Toprakcioglu *Macromolecules* **24** 3681 (1991).

[7]Quirk, R.P. *Macromolecules* **22** 85 (1989).

[8]Iyengar, D.R. and T.J. McCarthy *Macromolecules* **23** 4344 (1990).

[9]H. Motschmann, M. Stamm, and Ch. Toprakcioglu *Macromolecules* **24** 3681 (1991).

[10]C. F. Majkrzak, and S. K. Satija, Private Communication.

[11]Press, W.H., B.P. Flannery, S.A. Teukolsky, and W. J. Vetterling, *Numerical Recipes* Cambridge: Cambridge University Press, 1986.

[12]Russell, T.P. Materials Science Reports **5**(4,5) 171-271 (1990) and references therein.

[13]M. Kawaguchi, and A. Takahashi *Adv. Colloid Int. Sci.* **37** 219 (1992).

[14]A. Halperin, M. Tirrell, and T.P. Lodge *Adv. Polym. Sci.* **100** 31 (1992).

[15]S.T. Milner *Science* **251** 905 (1991).

[16]S. Alexander *J. Phys. (Paris)* **38** 983 (1977).

[17]P.–G. de Gennes, *J. Phys. (Paris)* **37** 1445 (1976); *Macromolecules* **13** 1069 (1980).

[18]P.J. Flory, *Principles of Polymer Chemistry* (Cornell University Press, Ithica, NY 1953).

[19]P.–G. de Gennes, *Scaling Concepts in Polymer Physics* (Cornell University Press, Ithica, NY 1979).

[20]A.K. Dolan and S.F. Edwards *Proc. R. Soc. London* **A343** 427 (1975).

[21]S.T. Milner, T.A. Witten, M.E. Cates *Europhysics Letters* 5(5) 413 (1988); *Macromolecules* **21** 2610 (1988).

[22]C.M. Wijmans, J.M.H.M. Scheutjens, and E.B. Zhulina *Macromolecules* **25** 2657 (1992).

[23]A. Halperin *J. Phys. (Paris)* **49** 547 (1988)

[24]T. Cosgrove, T Heath, B. van Lent, F. Leeermakers, and J. Scheutjens *Macromolecules* **20** 1692 (1987).

[25]M.D. Whitmore and J. Noolandi *Macromolecules* **23** 3321 (1990).

[26]D.L. Allara, Z. Wang, and C.G. Pantano *Journal of Non-Crystalline Solids* **120** 93 (1990).

[27]Iyengar, D.R. and T.J. McCarthy *Macromolecules* **23** 4344 (1990).

[28]P. Frantz, D.C. Leonhardt, and S. Granick *Macromolecules* **24** 1868 (1991).

[29]A. Halperin *J. Phys. (Paris)* **49** 547 (1988).

[30]K. Shull, Unpublished results.

[31]S. J. Hirtz M.S. Thesis University of Minnesota (1986).

[32]M.D. Whitmore and J. Noolandi *Macromolecules* **23** 3321 (1990).

[33]P. Auroy, L. Auvray, and L. Léger Phys. Rev. Lett. 66(6) 719 (1991).

[34]Press, W.H., B.P. Flannery, S.A. Teukolsky, and W. J. Vetterling, p.684 *Numerical Recipes* Second Edition Cambridge: Cambridge University Press, 1986.

[35]C. Strazielle and H. Benoit *Macromolecules* **8** 203 (1975).

[36]C.M. Wijmans, J.M.H.M. Scheutjens, and E.B. Zhulina *Macromolecules* **25** 2657 (1992).

[37]Iyengar, D.R. and T.J. McCarthy *Macromolecules* **23** 4344 (1990).

[38]C. Strazielle and H. Benoit *Macromolecules* **8** 203 (1975).

# CHAPTER 4

# SAN COPOLYMERS AT SURFACES

## 4.1 Introduction

There are many examples of incompatible polymer blends which have mechanical properties inferior to all of the components present in the blend. For example, polystyrene/polyethylene blends fail at very low stresses unless compatibilizing agents (read: diblock copolymers) are present at the interfacial regions of the blend.[1] These blends are weak because the low degree of mutual interpenetration prevents the formation of entanglements across the interface. The diblock copolymers can be used to "anchor" the coexisting phases together if they form at least one entanglement on each side of the interface.[2] Hence, the role of entanglements across immiscible interfaces is immensely important.

ABS resins are comprised primarily of polybutadiene rubber particles in a SAN copolymer matrix. These resins exhibit a desirable combination of economy, toughness, and processability. The (mutually immiscible) SAN and rubber phases are anchored together by SAN molecules which are grafted to the rubber particles. ABS resins can also be blended with polycarbonate, producing alloys with further improved toughness. Unlike the SAN/rubber interface, no grafting of SAN to PC is required for acceptable interfacial adhesion. Although the interfacial behavior of SAN copolymers is one of the key criteria influencing the mechanical properties of these blends, it is not well-understood. The goal of this chapter is to identify the fundamental principles governing the behavior of SAN copolymers near surfaces. Particularly, the role of composition drift on the surface composition has been investigated.

The rest of this chapter is organized as follows. The synthesis and phase behavior of SAN copolymers are discussed in Sections 4.1.1 and 4.1.2. Section 4.2 describes experiments and results of miscible blends of SAN copolymers near surfaces. Section 4.3 discusses experiments and results of the SAN/PC interface.

### 4.1.1 SAN Copolymers: Synthetic Realities

SAN copolymers are typically synthesized via free-radical copolymerizations by one of three processes: suspension, emulsion, or bulk. The styrene acrylonitrile system exhibits an azeotrope (where the compositions of the comonomer feed and the copolymer are the same) at approximately 38 mol% acrylonitrile.[3] Styrene and acrylonitrile have reactivity ratios $r_1 = 0.40$ and $r_2 = 0.04$ respectively.[4] Because $0 < r_1 r_2 < 1$, this comonomer pair exhibits a tendency toward alternating copolymerization. This observation is relevant when considering SAN copolymers near surfaces, as tendencies toward blockiness could play a significant part in segregation near surfaces. The primary SAN copolymer used in the experiments discussed in this chapter, DSANEF (see Table 4.1), is therefore well-suited (as "random" copolymers go) for surface studies, having near–azeotropic composition and no tendency toward blockiness.

Free radical polymerizations generally produce products with polydispersity indices (PDI) of 2 or more. The SAN copolymers in discussed in this chapter are no exception. DSANEF and DSANGH both have PDI values of ~2 while the PDI of SAN43 is somewhat higher (~3). This is probably a consequence of the temperatures accompanying the different methods of polymerization. DSANEF and DSANGH were polymerized using a suspension polymerization (T ~ 80°C) while the SAN43 was polymerized via a continuous bulk process (T ~ 160°C).

Styrene monomers form dimers and trimers spontaneously upon polymerizations at moderate and high temperatures.[5] When acrylonitrile is present as a comonomer, the oligomeric products are predominantly S-AN-AN and S-S-AN trimers, as revealed by mass spectrometry experiments carried out at the Chemical Group of Monsanto Company.[6] These dimers and trimers make up 1 w% to 4 w% of the polymerization products, depending on the polymerization temperature, and are readily removed from the polymer by standard re precipitation techniques.

### 4.1.2 Phase Behavior of SAN : SAN Blends

The primary determinants of the phase behavior of SAN/SAN blends are molecular weight and the AN content of each component. Table 4.1 shows these quantities for the SAN : SAN blends discussed in this chapter. ten Brinke and coworkers have developed a formalism relating the interaction parameter $\chi$ for a blend of two random copolymers to the composition of the copolymers and the interaction parameters between the monomers from which the copolymers are made.[7] Applying this formalism and using $\chi_{S-AN} = 0.8$ one obtains $\chi = 2.0 \times 10^{-3}$ for DSAN38 : SAN43, corresponding to $\chi \approx 0.95\chi_C$.[8,9] This $\chi$ value is consistent with all phenomenological evidence obtained with the DSAN38 : SAN43 system, including annealing samples at $\phi \approx \phi_c$ for extended periods of time at temperatures $T > T_g + 30°C$ and higher. In contrast, blends of SAN38 with SAN48 readily exhibit where phase separation (they scatter light strongly) under a wide range of experimental conditions.

## 4.2 Miscible Polymer Blends Near Surfaces

Consider a binary blend of polymers 1 and 2 free from external influences (such as surfaces or mechanical perturbation). A sample of these polymers of composition $\phi$ (where $\phi$ is the volume fraction of polymer 1 in the mixture) will mix homogeneously if

$$0 > \frac{G_m}{kT} = \frac{\phi \ln\phi}{N_1} + \frac{(1-\phi)\ln(1-\phi)}{N_2} + \phi(1-\phi)\chi \qquad (4.1)$$

where $G_m$ is the free energy change upon mixing and $\chi$ is the interaction parameter. The first two terms (which are entropic in origin) are always negative, approaching zero in the limit of large N. They act to drive the components toward mixing. The last term is usually positive, increasing in relative importance at large N. For the case where $\chi$ is small and positive, entropy tends to drive the system toward the mixed state while enthalpic interactions tend to drive the system toward demixing.

If the blend is perturbed in some way, other factors can contribute to $G_m$. For example, if the perturbation is caused by a surface, one might expect the perturbation of $G_m$ to depend on the difference in surface tensions of the two components. Binder and Schmidt have adapted the mean field approach of Cahn (originally developed by van der Walls) to polymer blends using a Flory-Huggins formalism.[10] The expression they obtain for the Helmholz free energy A of a polymer blend in contact with a surface is,

$$\frac{A}{kT} = f_s(\phi_1) + \int_0^\infty dz \left( G_m(\phi) - \phi(\Delta\mu) + \frac{a^2}{36\phi(1-\phi)} \left(\frac{d\phi}{dz}\right)^2 \right) \qquad (4.2)$$

where $G_m$ is given by Equation 4.1, a is the polymer statistical segment length, $\Delta\mu = \left(\frac{\partial G_m}{\partial \phi}\right)$ evaluated at $\phi = \phi_\infty$, and $f_s(\phi_1)$ is a "bare" surface free energy, assumed to depend on $\phi_1$ only, given by

$$f_s(\phi_1) = -\mu_1\phi_1 - \tfrac{1}{2} g\phi_1^2. \qquad (4.3)$$

where $\mu_1$ is the chemical potential favoring one component at the surface and g characterizes the effect of the surface on the binary interactions between the components. This expression is strictly valid only at low $\phi$ (a condition difficult to maintain for "surface enriched" blends). However, it does seem to hold as at least a first approximation for many systems including those discussed in this chapter. See Section 4.2.4 for details.

While the difference in surface tensions is the primary driving force behind segregation of one component to the surface of a miscible blend, the thermodynamics of the bulk play a large role in determining the surface excess. This is most easily understood by thinking of segregation as a process of partial demixing. As the components of the blend become less compatible, the free energy penalty of partial demixing decreases. Figure 4.1 shows the calculated $\chi$ dependence of the volume fraction profile of polymer 1, holding $\phi_1$ and $\phi_\infty$ constant. The surface excess depends strongly on $\chi$, especially as $\chi$ approaches $\chi_c$.

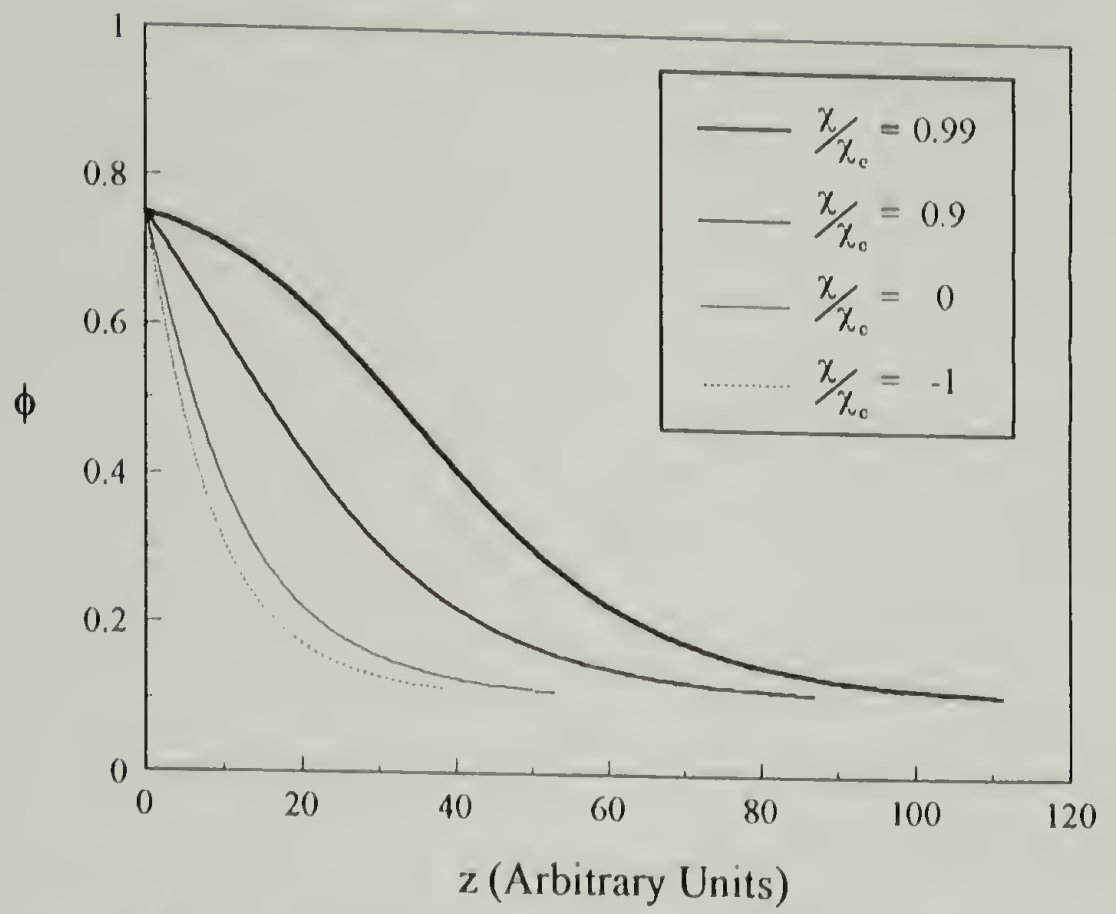


Figure 4.1 Calculated volume fraction profiles of a series of miscible polymer blends having $\frac{\chi}{\chi_c}$ values ranging from -1 to 0.99. (Calculated from Reference 10)

Thus, segregation is driven by differences in surface tension and by the thermodynamics of mixing in the bulk. As mixing becomes less favorable in terms of free energy, the surface excess increases

### 4.2.1 Description of Materials and Experiments

Table 4.1 summarizes the molecular parameters of the polymers discussed in this chapter. These were supplied and characterized by the Chemical Group of Monsanto Company. All of the SAN copolymers except SAN43 were polymerized on the laboratory scale via free radical polymerizations carried out to low yields. The SAN43 was polymerized via a continuous polymerization process. All polymers were re precipitated from solutions of $c \approx 2\frac{w}{w\%}$ added dropwise into large excesses of methanol under stirring.

The molecular weights were measured using size exclusion chromatography and the AN contents of the copolymers were confirmed using CHN microanalysis at both UMASS and the Chemical Group of Monsanto Company.

Table 4.1 Molecular parameters of the polymers discussed in Chapter 4.

| Polymer Name | $\overline{M_n}$ Kg · mol$^{-1}$ | Mole Fraction AN | PDI |
|---|---|---|---|
| DSANEF | 81.5 | 0.38 | 2.20 |
| DSANGH | 58.2 | 0.38 | 1.96 |
| SAN43 | 81.3 | 0.43 | 2.98 |
| SAN38 | 79.6 | 0.38 | 2.05 |
| PC 6500 | 6.5 | — | 2.94 |

The primary experimental techniques utilized in the work discussed in this chapter are SIMS and NR. Two types of samples were used in this chapter: single films (such as a miscible blend deposited on a substrate); and bilayers, consisting of two films deposited in series on the substrate. All films were prepared by spin casting unless otherwise noted. The SAN copolymers were spun from solutions of MIBK (typically 4 $\frac{w}{w\%}$) onto silicon or glass substrates. The PC 6500 (hereafter referred to as PC) was spun from solution of 1,2 dichloroethane (typically 8 $\frac{w}{w\%}$) onto silicon substrates. The PC films had to be spun under conditions where the air above the substrate was nearly saturated with the spin casting solvent. The samples comprised of single films were spun directly onto the silicon substrate, as was the base film of the bilayer samples. The upper films of the bilayers were spun onto clean glass substrates, floated onto a pool of de ionized water, and deposited onto the base film. The samples were then dried in vacuum at 23°C < T < 80°C for ~24

hours, and then subjected to the thermal treatments required for experiments. The SIMS samples then required two more steps: the addition of a "sacrificial" layer (typically a 400Å layer of polystyrene) and then sputter coating of a thin gold film to prevent excessive charging of the sample during the SIMS experiment. The samples for NR were used with no further treatment.

The procedure for substrate preparation is as follows. Silicon wafers (N–type) at least 5 millimeters thick were purchased from Semiconductor Processing Company. They were degreased in $NH_4OH$ solution, rinsed thoroughly in de ionized water, and then placed in a ~5% HF solution until water no longer wetted the substrate (usually 20 - 30 seconds). They were then rinsed thoroughly with de ionized water, and then immediately used for spin coating (see Chapter 2 for a description of the spin coating procedure).

### 4.2.2 Copolymer Composition and Segregation at Interfaces

An SAN copolymer's acrylonitrile content is the single most important determinant of its behavior near surfaces. Indeed, in the experiments discussed in this section, the acrylonitrile content is the only determinant. In miscible SAN : SAN blends, the low AN content component segregates to the polymer/vacuum and polymer/substrate interfaces. Figure 4.2 shows the experimentally observed neutron reflectivity of a 977Å film of (0.3)DSANEF : (0.7)SAN43 film on a smooth, flat silicon substrate before and after annealing. Note that the low AN content component has the deuterium label. The increase in the sample's reflectivity at $k > 0.005Å^{-1}$ indicates segregation of the high $\rho_n$ component, DSANEF, to the polymer/vacuum interface, the dominant contributor to sample's reflectivity at large k values. Detailed analyses of these data sets shall be presented in the following paragraphs.

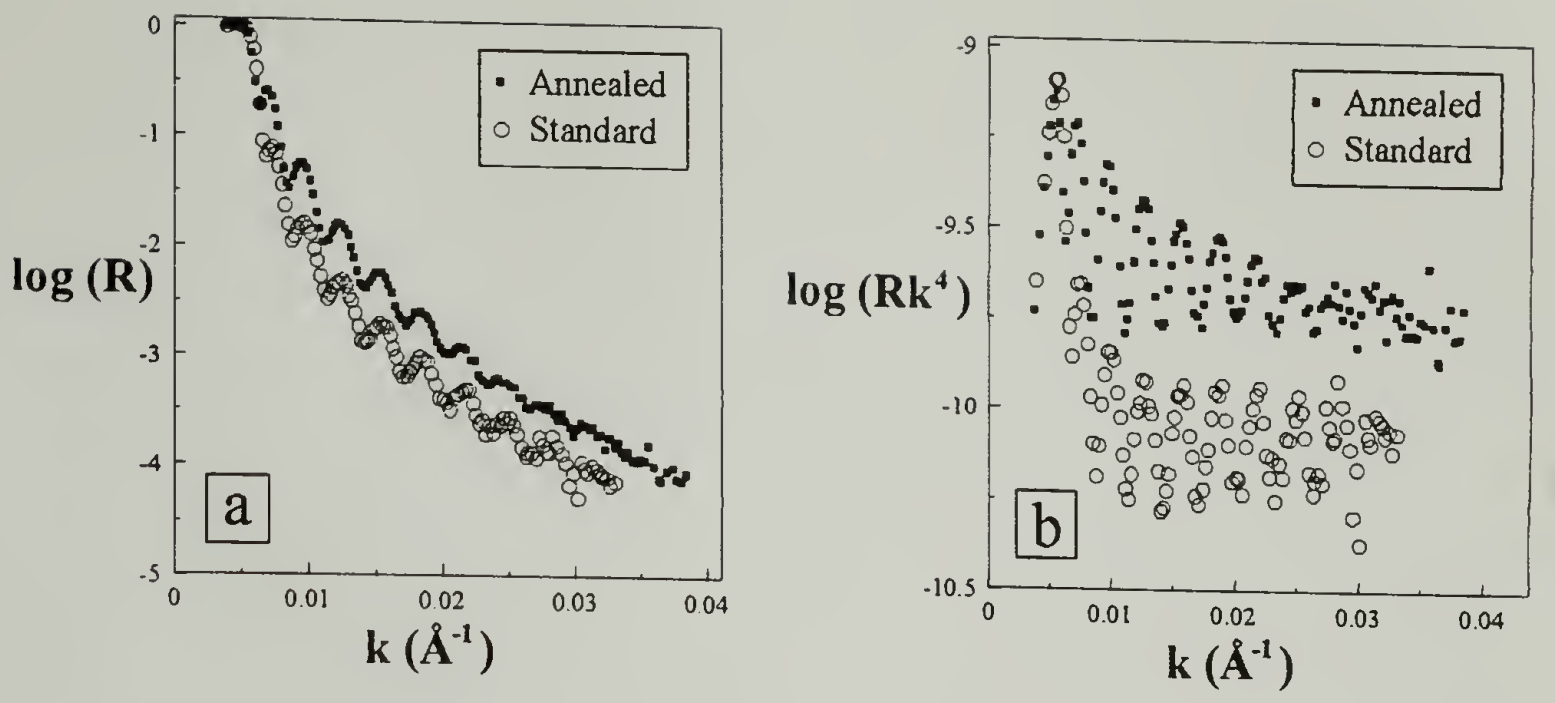


Figure 4.2 a) Observed neutron reflectivity for (0.3) DSANEF : (0.7)SAN43 before and after annealing for 69 hours at 167°C. b) Same data plotted as $Rk^4$ vs k.

There are two primary differences between DSANEF and SAN43: isotope and acrylonitrile content. Studies performed on isotopic blends of polystyrene have confirmed that the deuteration of one component can provide a driving force for surface segregation.[11,12] segregation of DSANEF to the surface brings a question: was the driving force due to isotope or composition. Figure 4.3 shows the observed NR of a (0.3)DSANEF : (0.7)SAN38 blend (matching AN content) before and after annealing.

Unlike the case where the AN contents differed, these data sets are the same before and after annealing and are correspond to samples uniform throughout in composition. Hence, for this set of SAN : SAN blends, the driving force for segregation due to AN content mismatch far outweighs the isotope effect.

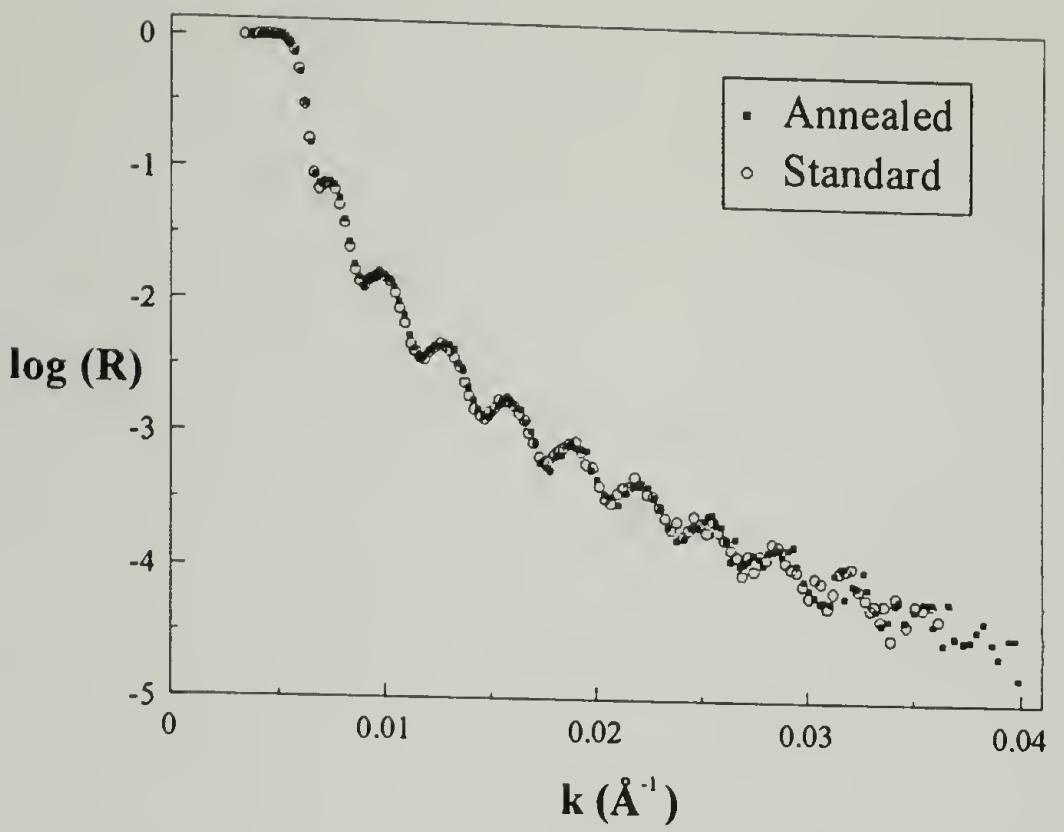


Figure 4.3 Observed neutron reflectivity for (0.3) DSANEF : (0.7)SAN38 (matching AN content) before and after annealing for 48 hours at 167°C.

A simple inspection of the NR data can provide some answers about the volume fraction profiles corresponding to the data sets in Figure 4.2 without detailed modeling of the data. The critical wave vector $k_c$ corresponds to $\rho_n = 2.65 \times 10^{-6}$Å$^{-2}$ in the bulk, corresponding to $\phi_\infty \approx 0.30$. Similarly, the limiting value of $Rk^4$ at large k corresponds to $\rho_n = 2.65 \times 10^{-6}$Å$^{-2}$ at the polymer/vacuum surface, corresponding to $\phi_1 \approx 0.30$. These observations suggest that the concentration of this film is uniform throughout. The situation is different after annealing. While the limiting value of $Rk^4$ at large k indicates that $\rho_n \approx 4.25 \times 10^{-6}$Å$^{-2}$ at the polymer/vacuum interface (corresponding to $\phi_1 \approx 0.75$), the critical wave vector $k_c$ indicates that $\rho_n \approx 2.4 \times 10^{-6}$Å$^{-2}$ in the bulk (corresponding to $\phi_\infty \approx 0.20$). One cannot explain the observed reflectivity of the annealed film with a uniform film of any $\rho_n$ value. Hence, one can conclude that an enriched layer of high $\rho_n$ material (DSANEF) has formed at the surface.

There are, however, several features of the concentration profiles which cannot be extracted from the NR data without quantitative modeling. In particular, segregation at the polymer/substrate interface (which does not dominate the reflectivity at large k but affects profoundly the oscillations in the reflectivity at intermediate k values), and the shape and thickness of the segregated layers are two features of the volume fraction profile which elude the simple type of NR data analysis described in the previous paragraph. Figure 4.4 shows a comparison between the experimentally observed NR of the annealed sample and the calculated NR corresponding to the profile of $\rho_n$ which best explains the observed NR of the annealed sample (shown at the inset). In addition to the $\rho_n$ values at the polymer/vacuum interface and in the bulk, this analysis provides an explicit profile of $\rho_n$ (and hence volume fraction DSANEF).

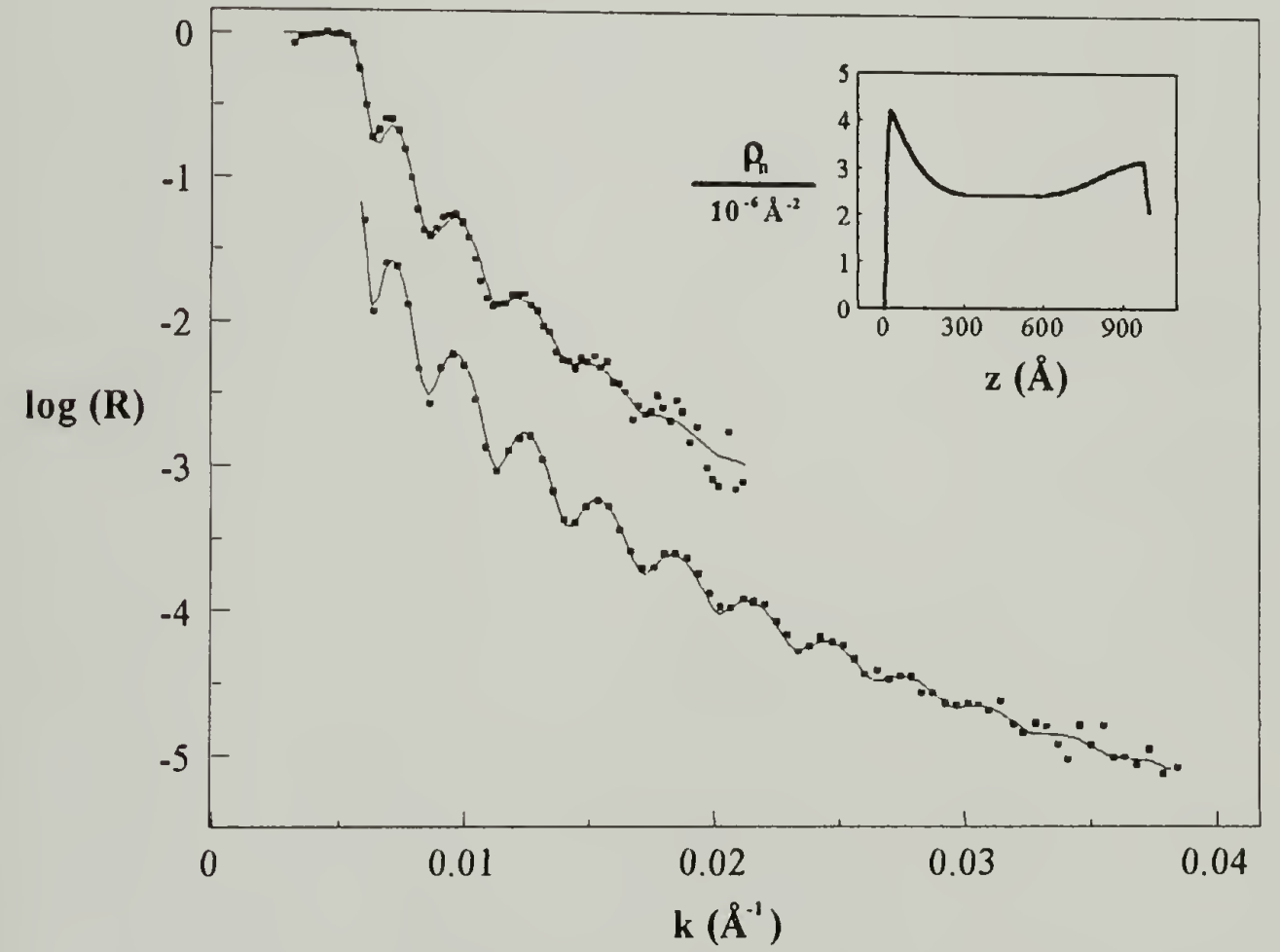


Figure 4.4 Comparison of calculated and observed neutron reflectivity for (0.3) DSANEF : (0.7)SAN43 after annealing for 67 hours at 167°C. These data were collected on POSY 2 at angles of 0.4° and 0.7°. The 0.7° data set has been shifted down on the plot by one decade. The calculated NR corresponds to the profile of $\rho_n$ shown at the inset.

Figure 4.5 shows a similar comparison of two calculated data sets: that shown in Figure 4.4 (returned to its proper decade), and one of a uniform film of $\rho_n = 4.25 \times 10^{-6}$Å$^{-2}$ (corresponding to $\phi_1$ of the segregated film). Because these films have the same profile at the polymer/air interface, the reflectivities approach the same limit at high k. However, because their bulk compositions differ, they exhibit very different $k_c$ values.

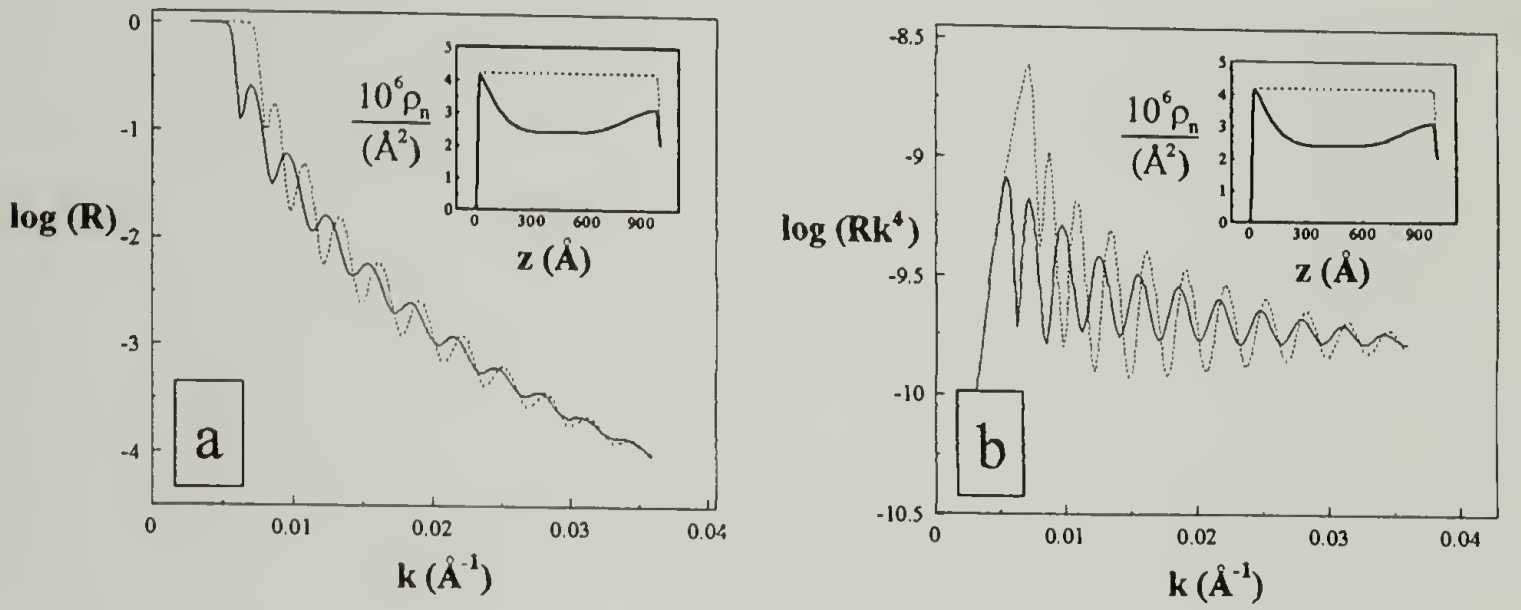


Figure 4.5 Comparison of two calculated neutron reflectivity data sets. The solid lines are the calculated sets shown in Figure 4.4 and the dotted lines correspond to a uniform film of $\rho_n = 4.25 \times 10^{-6}$Å$^{-2}$.a) log R vs k and b) log Rk$^4$ vs k. The $\rho_n$ profiles from which the reflectivity was calculated are shown at the inset.

Up to this point, all of the experimental data presented in this chapter has been collected on POSY 2. One may reasonably ask to what extent is the measurement of concentration profiles affected by the choice of reflectometer or, for that matter, by the vagaries of the sample preparation procedure itself. To this end, a sample of (0.3)DSANEF : (0.7)SAN43 was prepared on a 10 cm substrate (POSY 2 utilizes 5 cm substrates) and measured on BT–7 neutron reflectometer. While these two instruments have different resolution functions, (see section 2.2.2 for more details) one should in principle be able to account for them and obtain results independent of the particular

experimental instrumentation. Figure 4.6 shows data collected on BT–7 for a 10 cm version of the sample used for the data set shown in Figure 4.4.

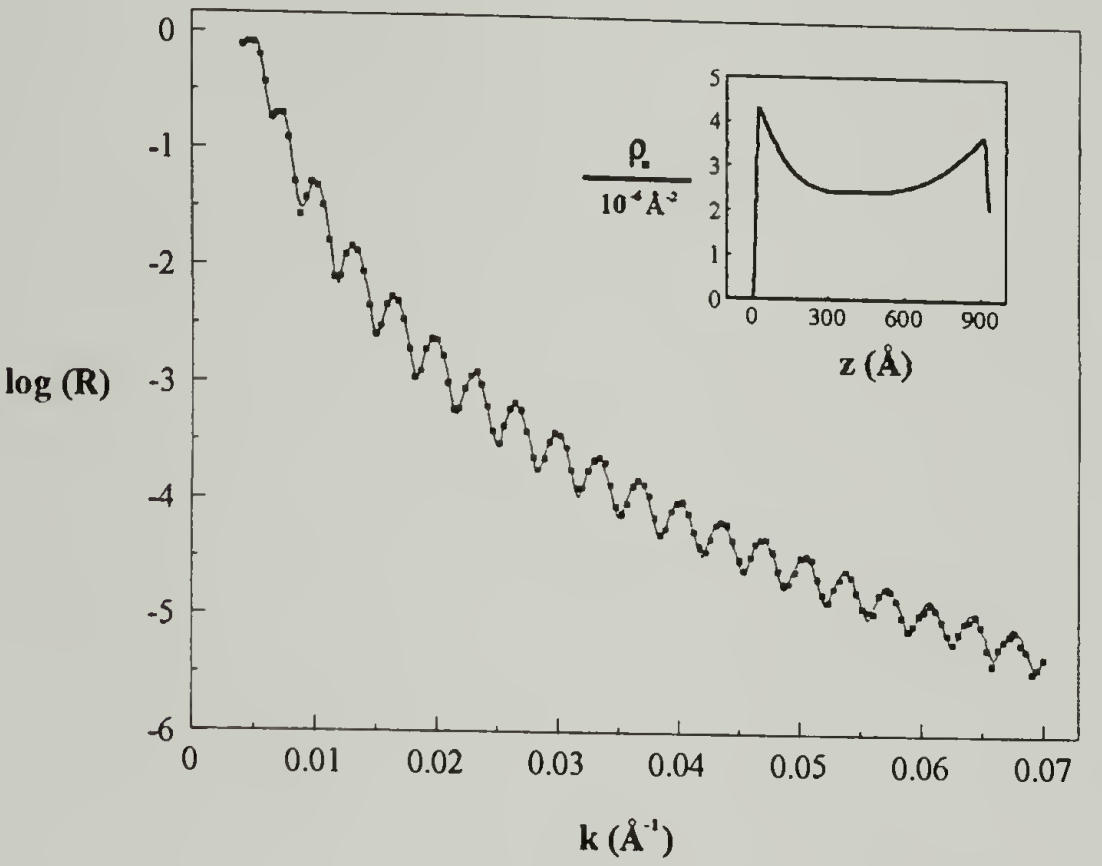


Figure 4.6 Comparison of calculated and observed neutron reflectivity for (0.3) DSANEF : (0.7)SAN43 after annealing for 69 hours at 182°C. These data were collected on BT–7 at angles varied continuously over $0 < \theta < 1.5°$. The calculated NR corresponds to the profile of $\rho_n$ shown at the inset.

The data set collected on the BT-7 reflectometer exhibits lower resolution than POSY 2 at small wave vectors and significantly higher resolution at large wave vectors. The data collection times on each instrument were similar, ~4 hours. The concentration profile obtained from this data set is strikingly similar to that shown in Figure 4.4, even though, at first glance, the data sets look significantly different, primarily because of the differing resolution functions. The BT-7 data set extends to larger k values, and is therefore more sensitive to the small size scale features at the polymer/vacuum interface, including the roughness and $\phi_1$. The BT-7 data set also has higher resolution at the larger

k values, where the oscillations in the reflectivity carry the most statistical weight. As a result, this data set is more sensitive to $\phi_{wall}$, the primary determinant of the oscillatory amplitude.

When blended with SAN43, DSANEF segregates to the polymer/vacuum interface and to the polymer/substrate interface, though less strongly to the latter. The oscillations in the reflectivity provide an accurate and reliable method of measuring the volume fraction DSANEF at the polymer/substrate interface. Figure 4.7 shows a comparison of two calculated NR data sets, one with no segregation at the substrate.

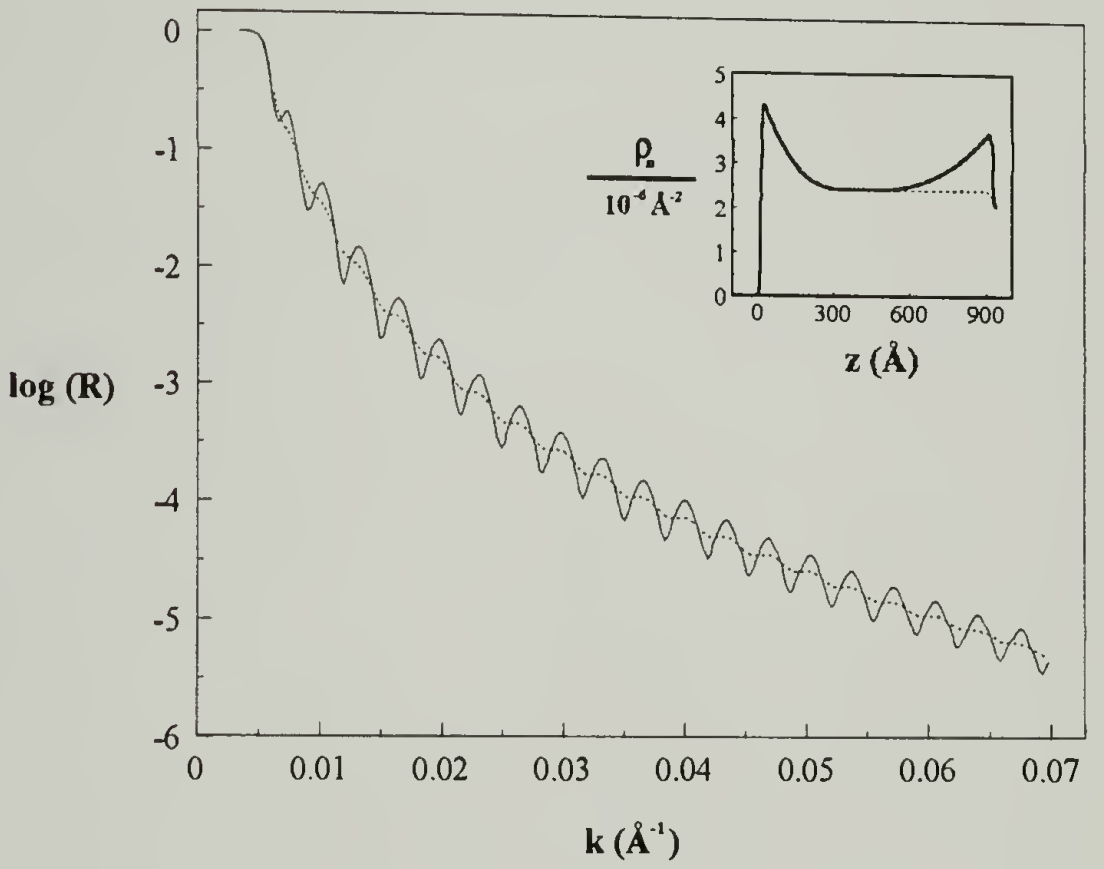


Figure 4.7 Calculated neutron reflectivity of two samples which are identical with the exception of segregation at the polymer/substrate interface. The oscillations are a manifestation of many orders of constructive and destructive interference between neutrons reflected from the front and back edges of the film.

The near disappearance of the maxima and minima in the reflectivity (broken line in Figure 4.7) coincide with the near $\rho_n$ matching of the polymer blend and substrate at the polymer/substrate boundary. The amplitude of the oscillations is very sensitive to the

volume fraction DSANEF at the polymer/substrate boundary (which is 0.52 in this case), and the phase of the oscillations shifts by $\frac{\pi}{2}$ radians if the polymer blend is "depleted" to the point where $\rho_{n\,(polymer)} < \rho_{n\,(substrate)}$.

The (0.3)DSANEF : (0.7)SAN43 sample has also been investigated using secondary ion mass spectroscopy (SIMS) in conjunction with Dr. Barry Wilkins at Bellcore. Figure 4.8 shows a comparison of the calculated and experimentally observed $CD^-$ ion trace for a sample 990Å in thickness. The calculated ion trace was directly convoluted with a Gaussian function increasing in width as the crater depth increased from FWHM = 85Å at z = 0 (just after the ~400Å sacrificial layer) to FWHM = 120Å at z ≈ 1000Å (at the polymer/substrate interface).

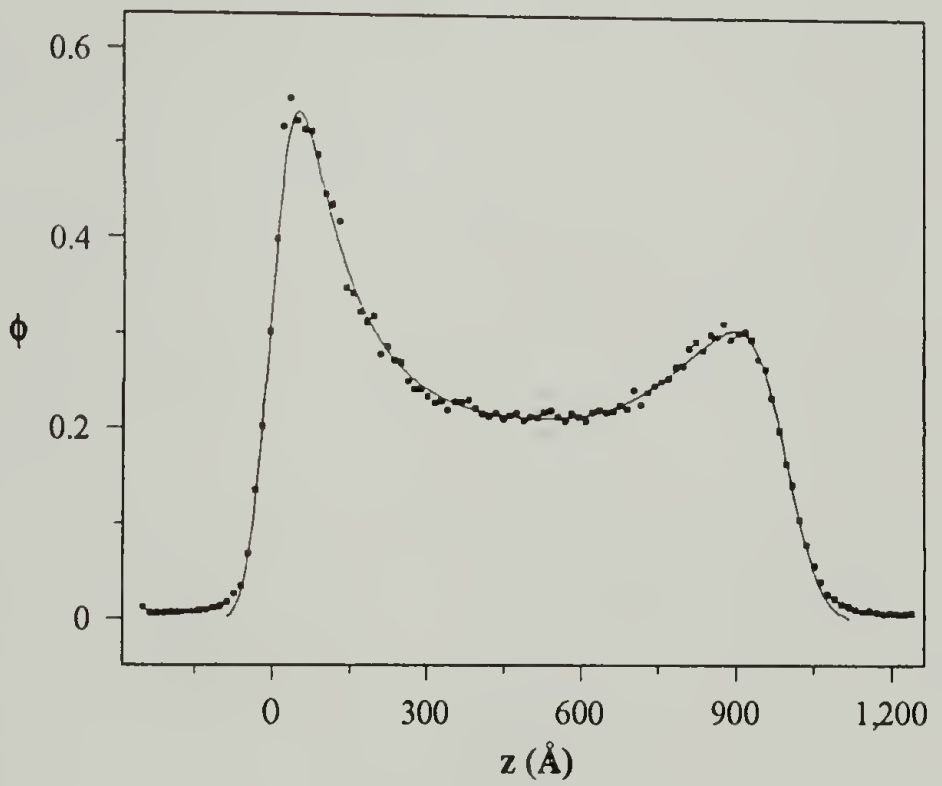


Figure 4.8 Comparison of calculated and experimentally measured $CD^-$ ion trace for a 990Å film of (0.3)DSANEF : (0.7)SAN43. $\phi$ is the volume fraction DSANEF.

Figure 4.9 shows comparisons of the volume fraction profiles for (0.3)DSANEF : (0.7)SAN43 measured using POSY 2, BT–7, and SIMS.

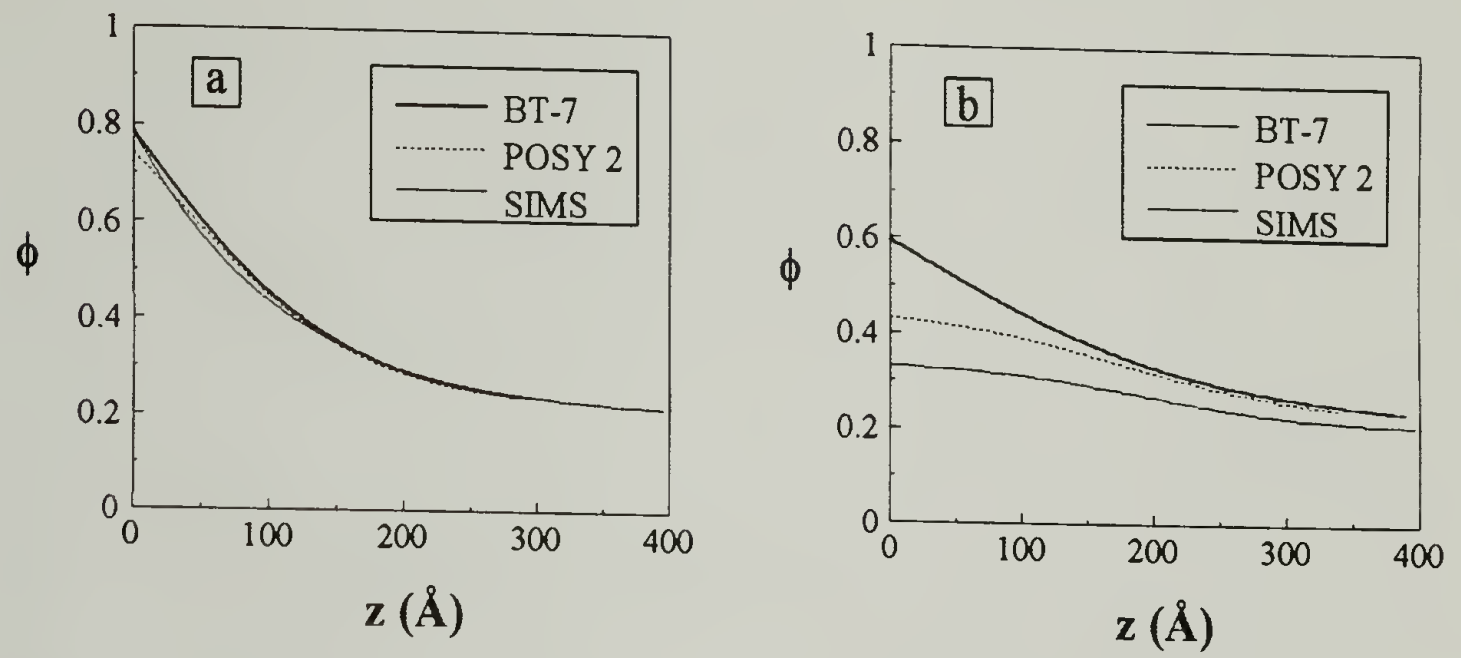


Figure 4.9 Comparison of measured volume fraction profiles for (0.3)DSANEF : (0.7)SAN43 measured using POSY 2, BT–7, and SIMS: a) at the polymer/vacuum interface and b) at the polymer/substrate interface.

At the polymer/vacuum interface, the agreement between instruments is remarkable. At the polymer/substrate interface (a "buried" interface, which is a more difficult experiment, see Section 1.3), the techniques agree on size scale, but quantitative agreement on the volume fraction DSANEF at the wall is not as good. Probably the most reliable data set is that from BT–7. The reflection techniques are sensitive to the sharpest discontinuities in $\rho_n$, which occur at the boundaries of the polymer film (see Figure 4.7). Of the two NR instruments, BT–7 has higher resolution at intermediate and large wave vectors, yielding a better measure of the amplitude of the oscillations in the reflectivity, which, in turn, provide a measure of the polymer composition at the back wall.

One can compare these results to mean field predictions for binary miscible polymer blends.[13] We take the BT–7 results as the basis for comparison.

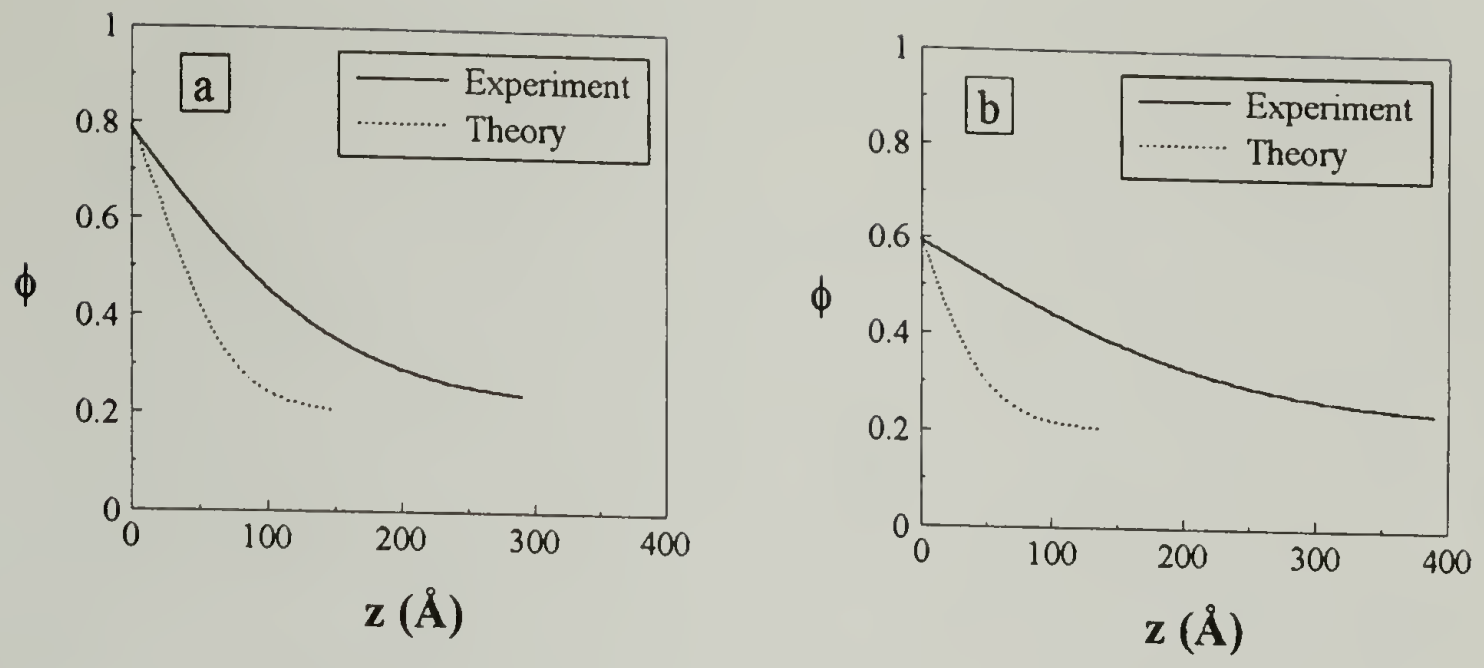


Figure 4.10 Comparison of calculated and measured volume fraction profiles for (0.3)DSANEF : (0.7)SAN43 a) at the polymer/vacuum interface and b) at the polymer/substrate interface. The calculated data sets were obtained using $\chi = 2.0 \times 10^{-3}$ and the number average degrees of polymerization for each component (see Reference 10).

As can be seen in Figure 4.10, if the number average degrees of polymerization are used ($\overline{N}_N$ = 911 and 991 for DSANEF and SAN43 respectively), the theory underestimates the thickness of the enriched polymer layer for $\chi = 2.0 \times 10^{-3}$. The theoretical result diverges if the weight average degrees of polymerization are used ($\overline{N}_W$ = 2001 and 2951 for DSANEF and SAN43 respectively). Furthermore if $\overline{N}_W$ is used in the calculations, the calculation becomes increasingly sensitive to small changes in $\chi$ as $\chi = 1.02 \times 10^{-3}$ is approached. Thus, the theory is of limited utility for the estimation of size scales for segregation in blends which are not too far from criticality. However, the theory and experiments are in qualitative accord in terms of the overall shape of the volume fraction profile and in terms of criticality. To within the precision within which c is known, the theory may be quantitatively correct as well, especially if lower N species segregate to the surface. These results would suggest that DSANEF and SAN43 are near the coexistence curve under the experimental conditions chosen.

If no fractionation of species of different molecular weights occurs at the surface, $\overline{N}_W$ is the best quantity to use to estimate the concentration profile. However, segregation of low N species to polymer surfaces has been predicted theoretically and observed experimentally. would be the best value to u One might expect fractionation of molecular weights to occur at the surfaces. Probably the most useful size scale for comparison in this case is the $R_g$ corresponding to $\overline{M_w}$, which is 110Å for DSANEF.

### 4.2.3 Blend Composition and Segregation

Volume fraction profiles for DSANEF : SAN43 films having overall compositions of 0.05 and 0.15 have also been measured using NR. These data are shown in Figures 4.10 and 4.11 respectively.

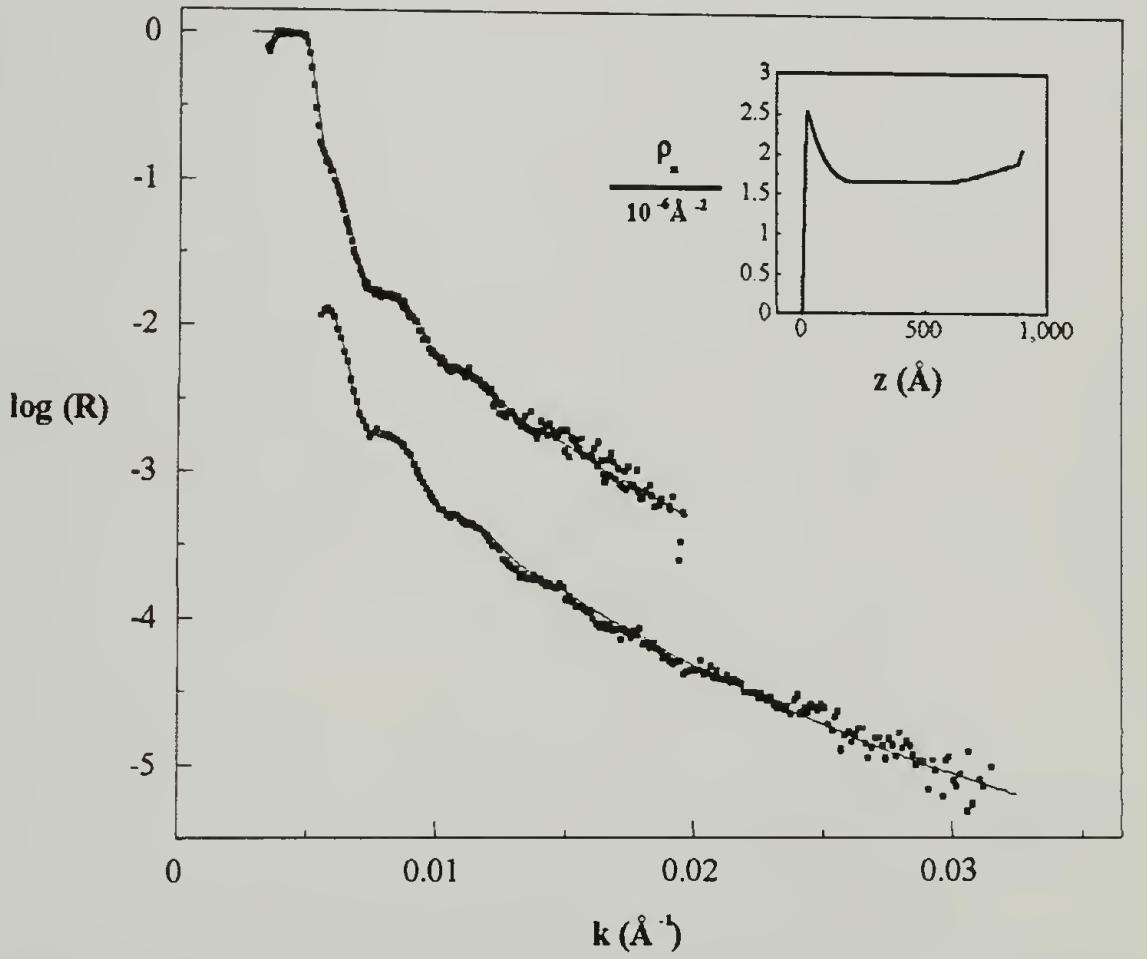


Figure 4.11 Comparison of calculated and observed neutron reflectivity for (0.05) DSANEF : (0.95)SAN43 after annealing for 69 hours at 166°C. The high angle data set has been shifted down on the plot by one decade. The calculated NR corresponds to the profile of $\rho_n$ shown at the inset.

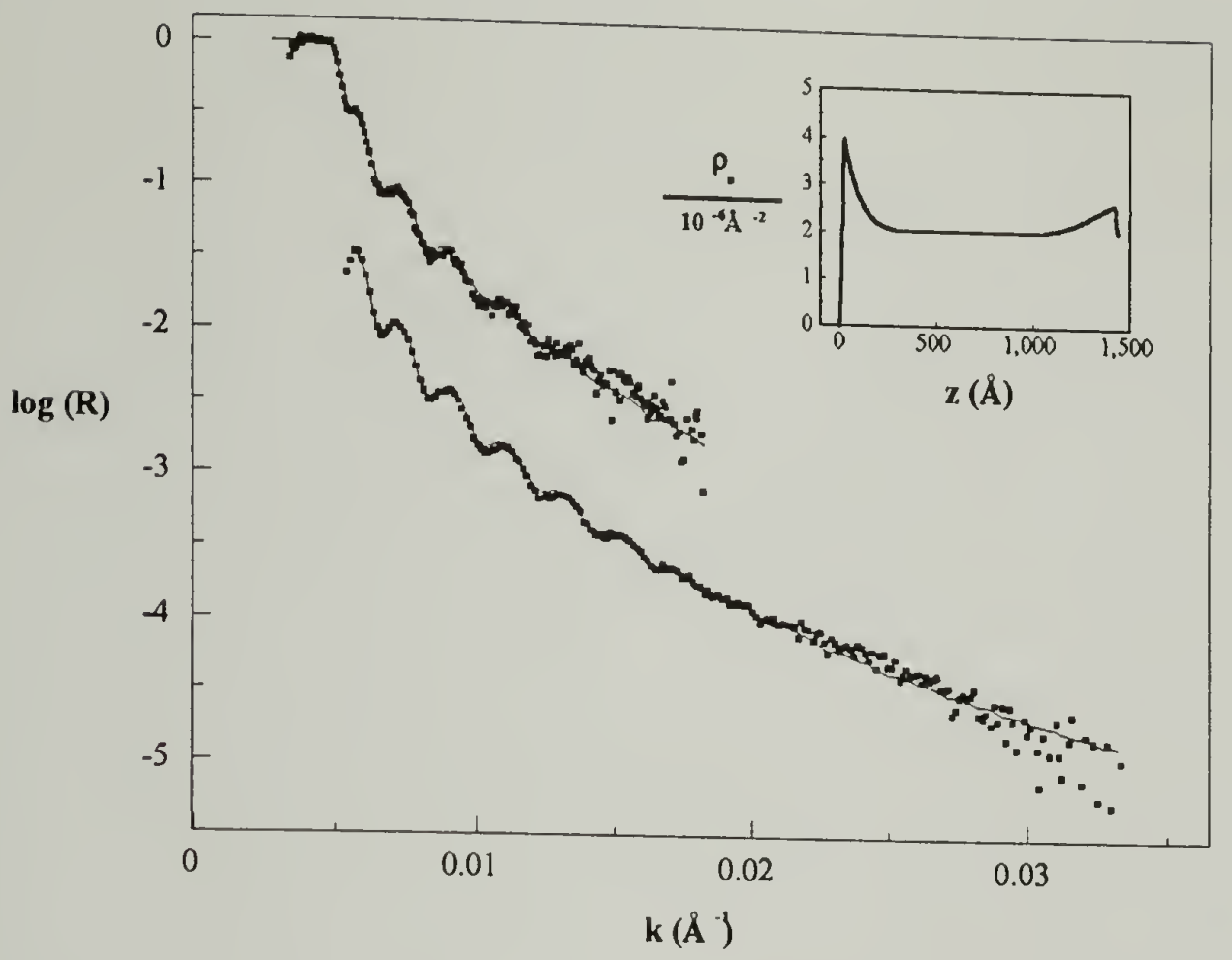


Figure 4.12 Comparison of calculated and observed neutron reflectivity for (0.15) DSANEF : (0.85)SAN43 after annealing for 69 hours at 166°C. The high angle data set has been shifted down on the plot by one decade. The calculated NR corresponds to the profile of $\rho_n$ shown at the inset.

SIMS measurements were also done on the sample of overall composition 0.05, and the results for the CD- ion trace are shown in Figure 4.13. Thus, the series of overall compositions from 0.05 to 0.30 can be examined in the form of an "isotherm" comparing the volume fraction DSANEF at the surface and in the bulk as shown in Figure 4.14.

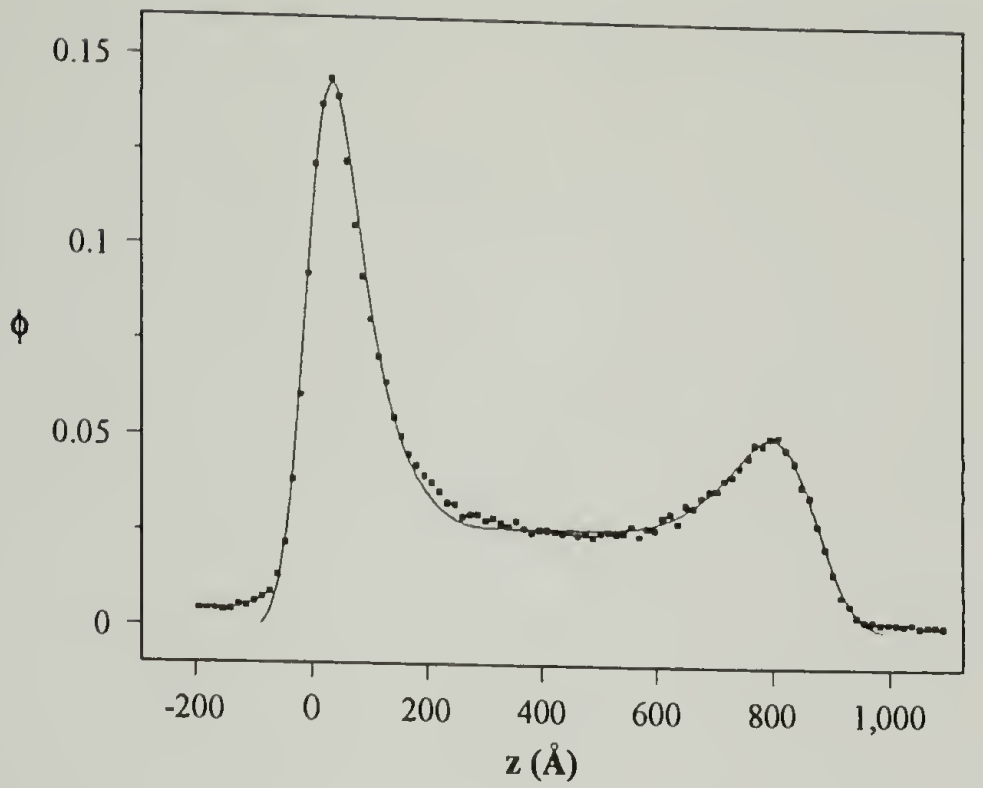


Figure 4.13 Comparison of calculated and observed SIMS $D^-$ ion trace for (0.05)DSANEF : (0.95)SAN43.

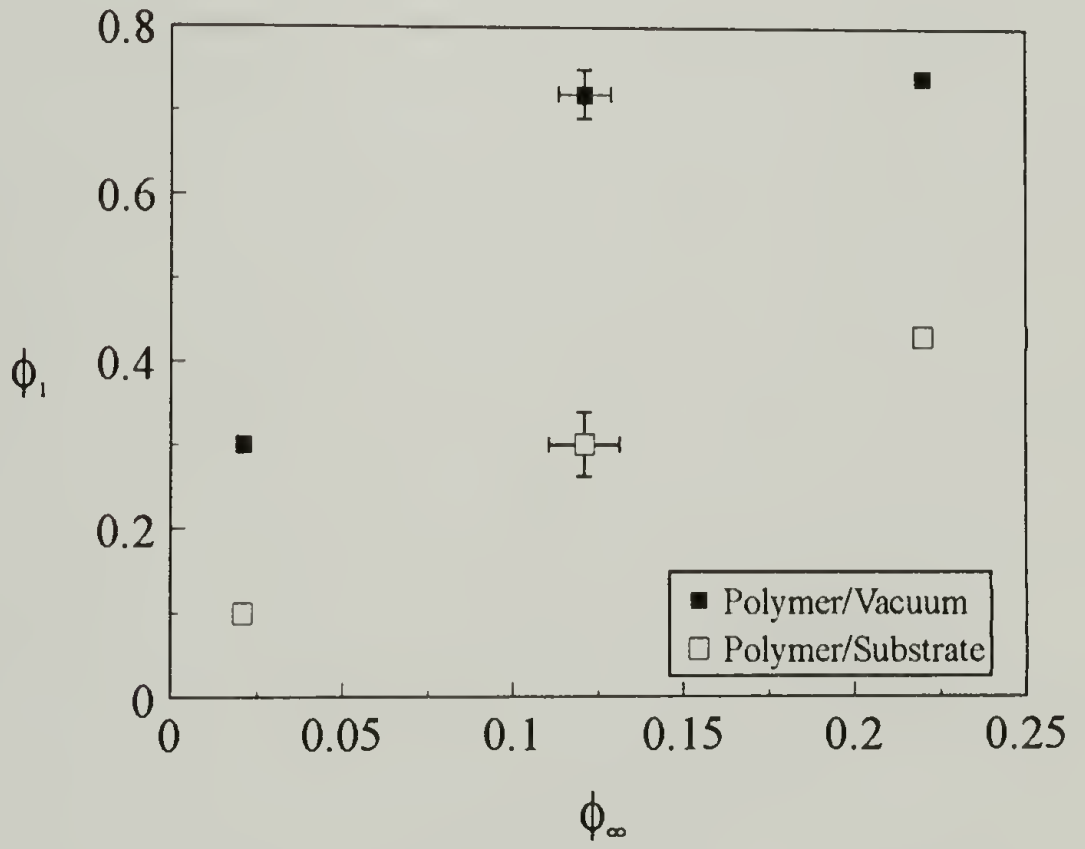


Figure 4.14 Volume fraction DSANEF at surface as a function of volume fraction DSANEF in the bulk.

The volume fraction DSANEF at the surface changes smoothly with bulk composition, growing most rapidly at low bulk compositions. The surface excess increases in a similar manner, as indicated in Figure 4.15.

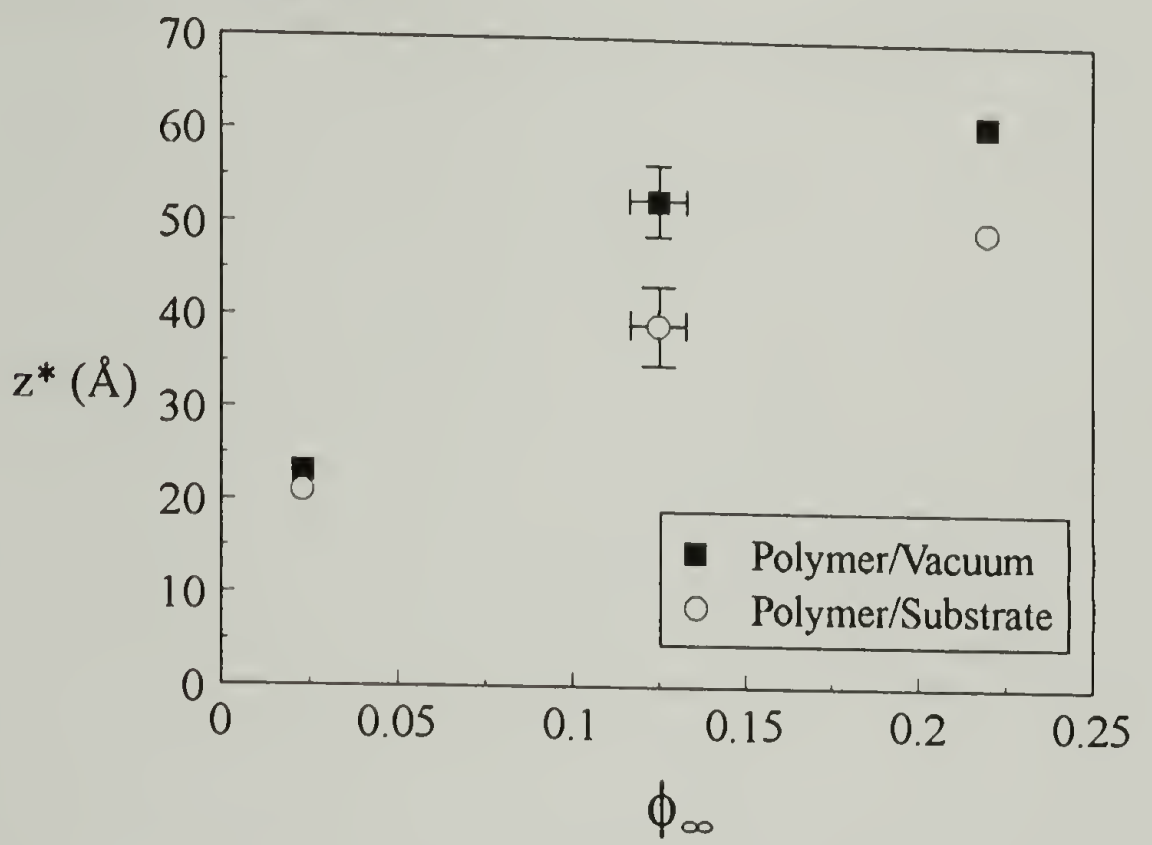


Figure 4.15 Surface excess DSANEF at polymer/vacuum interface as a function of volume fraction DSANEF in the bulk.

The surface excess increases with increasing bulk concentrations, leveling off at higher bulk compositions. The approach of "saturation" is not rapid (compare, for example, with the case of DPS adsorbed on $SiO_2$ from cyclohexane; Section 3.2), consistent with low free energy consts for demixing and relatively low surface affinity of DSAN38. Further, the thickness of the enriched layer (L = 187Å at $\phi_\infty = 0.205$) is larger than the "unperturbed" molecular dimension ($R_g$ = 107 Å), another indication that much of the segregation is driven by the bulk thermodynamics. Correspondingly, the "surface activity" of DSANEF in SAN43 is relatively small (depending, of course, on the reader's frame of reference–less active than most surfactants, but more active than isotopic polymer blends). Figure 4.16 shows a plot of the difference in surface free energy vs the volume fraction

DSANEF at the surface for the polymer/vacuum and polymer/substrate interfaces for the three compositions.

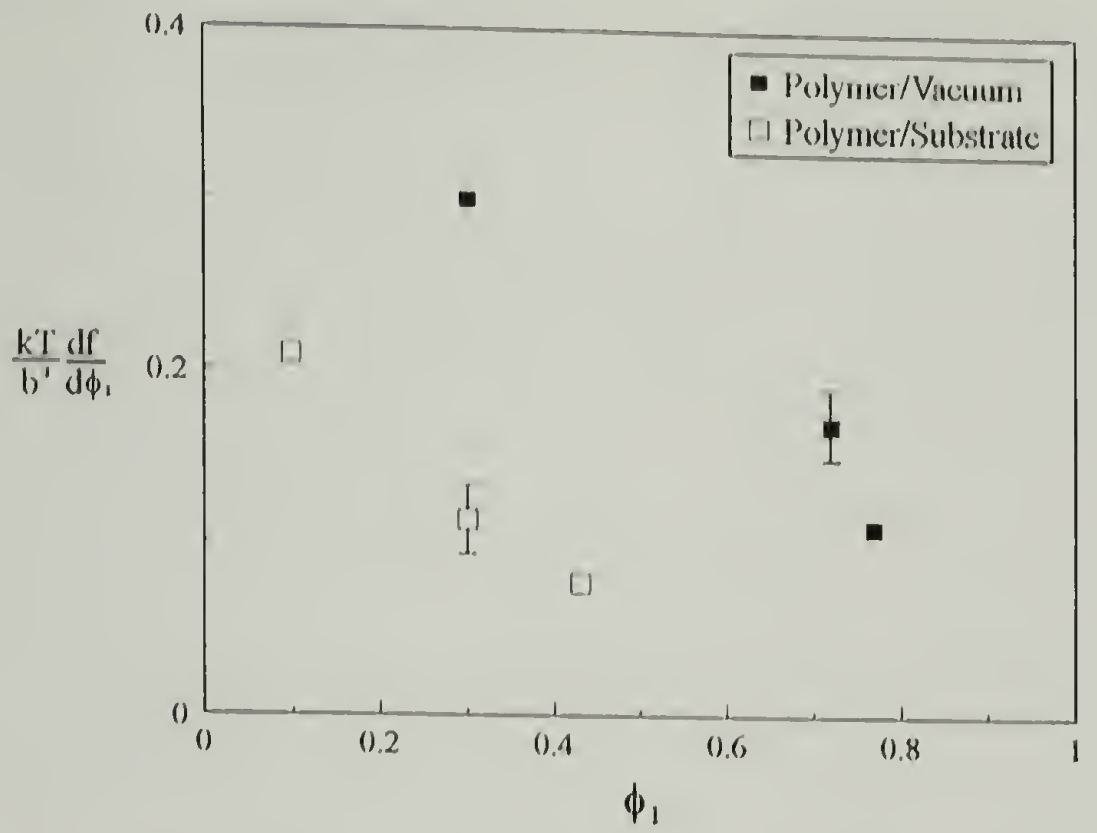


Figure 4.16 Difference in surface energy as calculated from Equation 4.3 as a function of volume fraction DSANEF at the surface. The intercepts are proportional to the difference in surface tensions and the slopes reflect the affect of the surface on the polymer/polymer interactions.

From the plot, one can estimate the the difference in surface tensions at the polymer/vacuum and polymer/substrate interfaces (corresponding to the quantity $\frac{kT}{b^3}\frac{df}{d\phi_1}$) as a function of $\phi_1$. These values range from 0.1 to 0.3 dyn·cm$^{-1}$ for the polymer/vacuum interface and from 0.08 to 0.21 dyn·cm$^{-1}$ for the polymer/substrate interface. One would therefore expect that the AN units in the copolymer interact with $SiO_2$ better than they interact with vacuum (or air). Both of these quantities decrease with increasing $\phi_1$, and do so at roughly the same rate. This behavior is consistent with the case where two surfaces exerting approximately the same effect on the polymer/polymer interactions near the surface even though the surface free energy with respect to each component differs. These

calculations also suggest that the affinity of DSANEF at the surface diminishes at higher DSANEF concentrations. This has had some experimental support.[14]

### 4.2.4 Effects of Temperature

The size and shape of the DSANEF : SAN43 concentration profiles is not very sensitive to temperature in the range of 155°C < T < 185°C. Figure 4.17 shows a comparison of (0.3) DSANEF : (0.7) SAN43 blends at the polymer/vacuum interface at temperatures of 155°C 167°C, and 182°C as measured by NR.

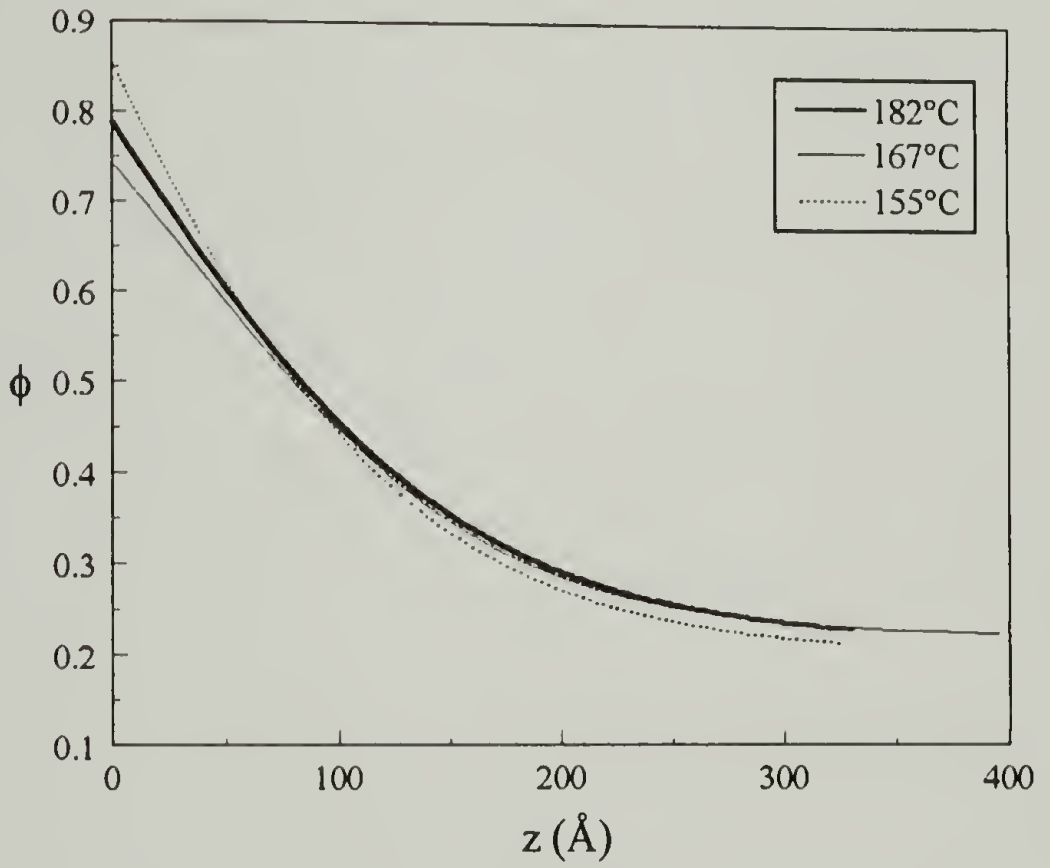


Figure 4.17 Comparison of measured concentration profiles of DSANEF : SAN43 at temperatures of 155°C, 167°C, and 182°C.

## 4.3 SAN Copolymers at Immiscible Interfaces

In many practical applications, SAN copolymers are grafted covalently to polymers with which they are incompatible, the primary example being ABS resins. However, some commercially important blends of SAN copolymers have been prepared with no special

grafting. The interfacial toughness of such (non-grafted) blends depends primarily on the number of effective entanglements across the immiscible interface. In this section, we compare concentration profiles and mechanical properties of SAN/PC blends with other systems, primarily the polystyrene/poly (methyl methacrylate) (PS/PMMA) system.

### 4.3.1 Theoretical Expression for Interfacial Width

Broseta and coworkers[15] have extended the self-consistent-field theories of Helfand and coworkers[16] to polymer blends of finite molecular weight. They obtain the following expression for the equilibrium interfacial width w between two coexisting phases according to

$$w = w_\infty \left(1 - 2 \ln 2 \left(\frac{1}{w_B} + \frac{1}{w_A}\right)\right)^{-1/2} \qquad (\#\#)$$

where a is the (average) statistical segment length, $w_\infty = \frac{2a}{(6\chi)^{1/2}}$ and $w_i = N_i \chi$.

### 4.3.2 Results and Discussion

Figure 4.18 shows a comparison of experimentally-observed NR of a ~740 Å film of SANGH on a thick (>2200Å) film of PC 6500 before and after annealing. The sites in this sample which dominate the reflectivity are the polymer/air and polymer/polymer interfaces, as opposed to the single film samples shown earlier in this chapter, where the polymer/air and polymer/substrate interfaces dominated. Hence, the amplitude of the oscillations is determined by the reflectivity of the polymer/polymer interface.

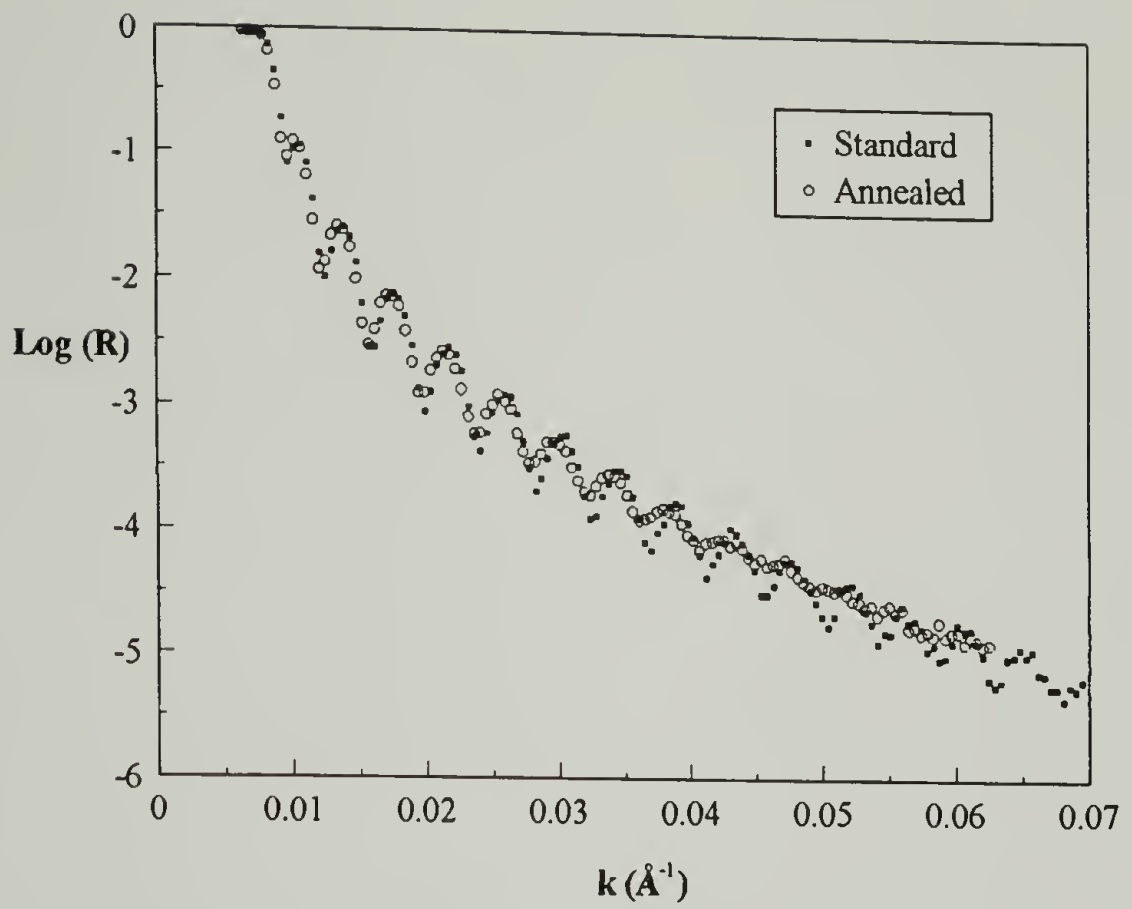


Figure 4.18 Comparison of experimentally-observed NR of a bilayer sample of SANGH (~740 Å thick) on a thick (>2200 Å thick) film of PC 6500 before and after annealing at 180°C for 20 hours. The dampening of the oscillations upon annealing indicates finite interdiffusion at the DSANGH/PC interface.

As long as the interfacial is not too broad, the amplitude of the oscillations is quite sensitive to the interfacial width (see Figure 1.1). One can obtain a measure of the width by simulations, which show the standard and annealed data sets in Figures 4.18 and 4.19 respectively.

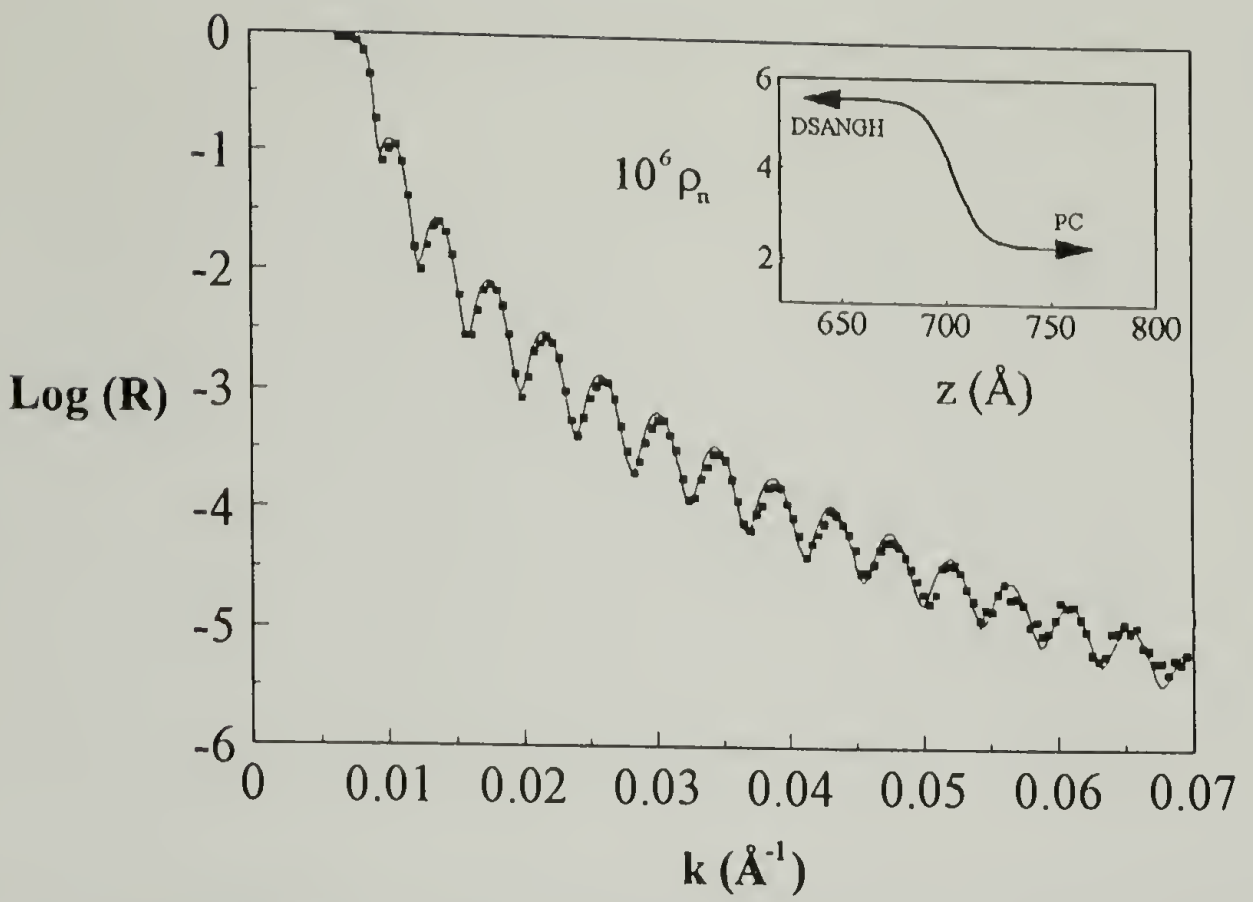


Figure 4.19 Comparison of calculated and observed NR of a 740 Å DSANGH film on a thick PC 6500 film before annealing.

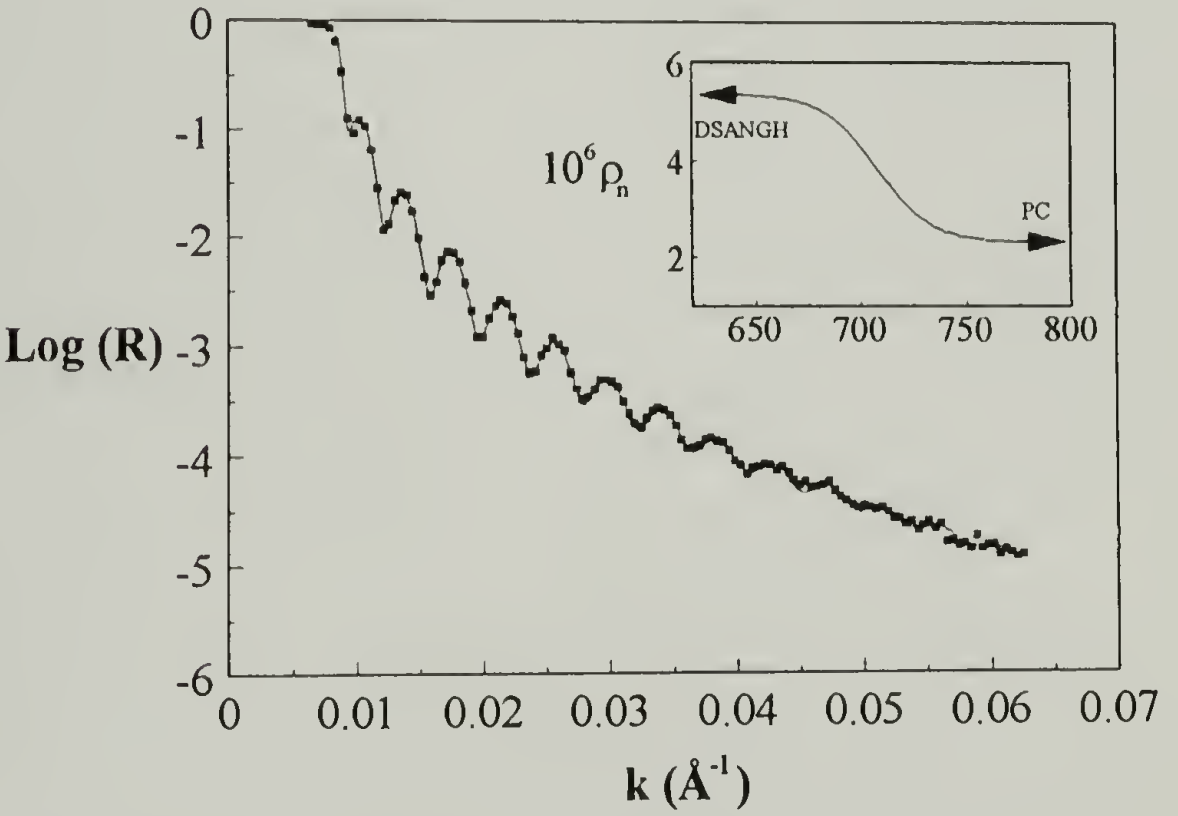


Figure 4.20 Comparison of calculated and observed NR of a 740 Å DSANGH film on a thick PC 6500 film after annealing at 180°C for 20 hours.

Note that the profile of scattering length density for the standard sample (at the inset) appears rounded at the polymer/vacuum and polymer/polymer interfaces. This rounding is a literal depiction of the modeling of the roughness, which is FWHM 12 Å and 28 Å respectively. This "initial" roughness must be accounted for in the calculation of the interfacial width of the annealed sample. The most straightforward "accounting method" is to simple subtract the interfacial roughness from the interfacial width in quadrature. The resulting measure of the interfacial width of the SAN/PC interface is 44 Å ±3 Å. Using the theory of Broseta and coworkers and assuming statistical segment lengths of 5.9 Å and 22 Å for DSANGH and PC 6500 respectively, one obtains $\chi = 0.064$, corresponding to $\frac{\chi}{\chi_c} \approx 2.3$. For reference, if infinite molecular weights are assumed, one obtains $\chi = 0.045$.

It is interesting to compare the interfacial widths of the SAN/PC (~45 Å) and the PS/PMMA (~50 Å) [17,18] systems in light of their known mechanical properties. The SAN/PC (20 - 30 $J \cdot m^{-2}$) interface[19] is about three times as tough as the PS/PMMA interface (5 - 10 $J \cdot m^{-2}$)[20] even though it is slightly thinner. The most plausible explanation comes from considering the hypothetical "distance" (in real space) between crosslinks of each of the components.[21] Assuming that the chains are unperturbed and that they are Gaussian on size scales of their entanglement molecular weight, Aharoni[22] has calculated values of ~ 40 Å and ~39 Å (comparable to the interfacial width) for PS and PMMA are respectively, while the distance between entanglements in PC is ~19 Å (approximately half the interfacial width).

## References


[1]R. Fayt, P. Hadjiandreou, P.H. Teyssie *J. Polym. Sci. Polym. Chem. Ed.* **23** 337 (1985).

[2]C. Creton and E.J. Kramer *Macromolecules* **24** 1846 (1991).

[3]G. Odian *Principles of Polymerization*, 2nd edition, Wiley Interscience, New York, 1981.

[4]L.J. Young *Copolymerization Reactivity Ratios* in Chapter 2 in *Polymer Handbook* J. Brandrup and E.H. Immergut with W. McDowell, Eds. Wiley Interscience, NY, 1975.

[5]Encyclopedia of Polymer Science Volume 16 p. 21.(1985)

[6]A. R. Padwa, Private Communication.

[7] G. ten Brinke, F.E. Karasz, W.J. MacKnight, *Macromolecules*, **16,** 1827 (1983).

[8] G.E. Molau, *Polymer Letters,* **3,** 1007 (1965).

[9] J.M.G. Cowie and D. Lath, *Makromolecular Chemie Macromolecular Symposium,* **16,** 103 (1988).

[10] I. Schmid and K. Binder, *Journal of Physics (Paris),* **46,** 1631 (1985).

[11] R.J. Composto, R.S. Stein, E.J. Kramer, R.A.L. Jones, A. Mansour, A. Karim, and G.P. Felcher, *Physica B,* **156 & 157,** 434 (1989).

[12] R.A.L. Jones, E.J. Kramer, M.H. Rafailovich, J. Sokolov, and S.A. Schwartz, *Physical Review Letters,* **62**(3), 280 (1989).

[13] I. Schmid and K. Binder, *Journal of Physics (Paris),* **46,** 1631 (1985).

[14]J. Genzer, R.J. Composto *Private Communication.*

[15]D. Broseta, G.H. Fredrickson, E. Helfand, and L. Leibler *Macromolecules* **23** 132 (1990).

[16]E. Helfand and Y. Tagami *J. Polym. Sci. Part B* **9** 741 (1971); E. Helfand and Y. Tagami *J. Chem. Phys.* **56** 3592 (1971);and E. Helfand and A.M. Sapse *J. Chem. Phys.* **62** 1327 (1975).

[17]Fernandez, M.L., J.S. Higgins, J. Penfold, R.C. Ward, C. Shackleton and D. Walsh, *Polymer* **29** 1923 (1988)

[18]Anastasiadis, S.H., T.P. Russell, S.K. Staija, and C.F. Majkrzak, *J. Chem. Phys.* **92** 5677 (1990)

[19]V. Janarthanan, R.S. Stein To be Published.

[20]H. R. Brown *Journal of Materials Science* **25** 2791 (1990).

[21]While it is often conceptually appealing to think of entanglements as being localized in space, it is likely that "real" entanglements are de localized to a significant degree. Therefore, this distance is strictly hypothetical.

[22]S.M. Aharoni *Macromolecules* **16** 1722 (1983).

# CHAPTER 5

# SUMMARY

The modification of surfaces is an area of considerable industrial and theoretical importance. The mechanical properties of polymer alloys having more than one phase is one example of the importance of interfaces in polymer systems. Furthermore, polymers play important roles in the modification of many non-polymeric surfaces, and have important roles in such fields as medicine, tribology, and microelectronics. This dissertation has included experimental results which can be brought to bear on both polymeric and non-polymeric surfaces.

The following paragraphs contain brief summaries of the experimental results and possible areas for further investigation.

## 5.1 Solutions of Terminally-Functionalized Polymers

A single carboxylic acid group on a polystyrene molecule of considerable molecular weight (up to 80 $Kg \cdot mol^{-1}$ or more) affects profoundly the conformation of the adsorbed polymer as well as the amount of polymer adsobed. These polymers "attach" themselves to the wall via the acid groups in quantities far greater than the "normal" polymer would. These polymers are strongly stretched, even under poor solvent conditions and are consistent with the predictions of Halperin i.e. the brush height depends strongly on the degree of polymerization in poor solvents, being best described by $L \sim N$ and by $L \sim \sigma^{0.5 \text{ to } 1.0}$.

One possible area for further work is to understand the effect of "foot strength" on the maximum extention of the polymers in the brush. For example, how sensitive would L be to changes in the interaction energy between the functional group and the wall?

Another interesting area would be to invoke competition between the functional group and the segments comprising the polymer in the brush. Could there be a "brush to pancake" transition upon increasing polymer/wall affinity for a given "foot strength"?

## 5.2 Miscible SAN Copolymer Blends at Interfaces

The acrylonitrile content of a SAN copolymer is the single most important factor determining its behavior near surfaces. For the range of compostions near the azeotrope (~38 mol% AN), the component of low AN content segregates preferentially at the polymer/vacuum interface as well as the polymer/substrate interface, consistent with differences in surface tension of ~ 0.04 to 0.25 dyn·cm$^{-1}$ depending on the chemical nature of the surface.

SAN copolymers are usually used in alloys in which more than one polymer phase is present. One useful extension of the work presented in Chapter 4 would be to better understand the behavior of SAN mixtures near interfaces with which both SAN components are immiscible.

## 5.3 Width of the SAN/PC Interface

The interfacial width of the SAN/PC interface is 44Å. In light of the large toughness of the SAN/PC interface, this result is somewhat surprising. By comparison, the polystyrene/PMMA interface is ~10% wider than SAN/PC and several times weaker. V. Janarthanan has recently shown that the toughness of the SAN/PC interface decreases monotonically with increasing oligomer content. These facts lead one to consider the possibility that PC chains (which have an extrordinarily low charactaristic ratio) form effective entanglements over smaller size scales than polystyrene and PMMA. Clearly, further investigation of this idea would be of great importance.

## 5.4 Unifying Principles

One of the themes of this dissertation is that the neutron reflection of a polymer sample is most sensitive to those regions exhibiting the greatest discontinuities in refractive index: namely, their surfaces and interfaces. Further, when two reflecting regions in a sample are within the coherence length of the radiation, interference can be utilized to obtain precise information about the density profiles of the polymers in these samples.

Another unifying principle is the role of bulk interactions in determining the degree of demixing which occurrs near perturbing objects such as surfaces. As coexistance is approached from the miscible side, the surface excess increases systematically. While surface tensions or specific interactions determine which component segregates, the free energy of mixing in the bulk determines the extent to which segregation occurs.

# APPENDIX

## FUNCTIONAL FORMS FOR NEUTRON REFLECTION SIMULATIONS

All of the PSCOOH data sets were modeled using the functional form

$$\phi(z) = \phi_\infty + \left(\frac{\phi_1 - \phi_\infty}{1 - \tanh\left(\frac{z_c}{\lambda}\right)}\right)\left(1 - \tanh\left(\frac{z}{\lambda} - z_c\right)\right) \qquad (3.15)$$

where $z_c$ is a parameter which can be shifted to change the shape of the profile, as shown in Figure A.1. In the case of H81C, this form was modified by adding a small exponential "lump" near the wall. This overall functional form is convenient from a modeling standpoint because of its well-behaved nature and versatility.

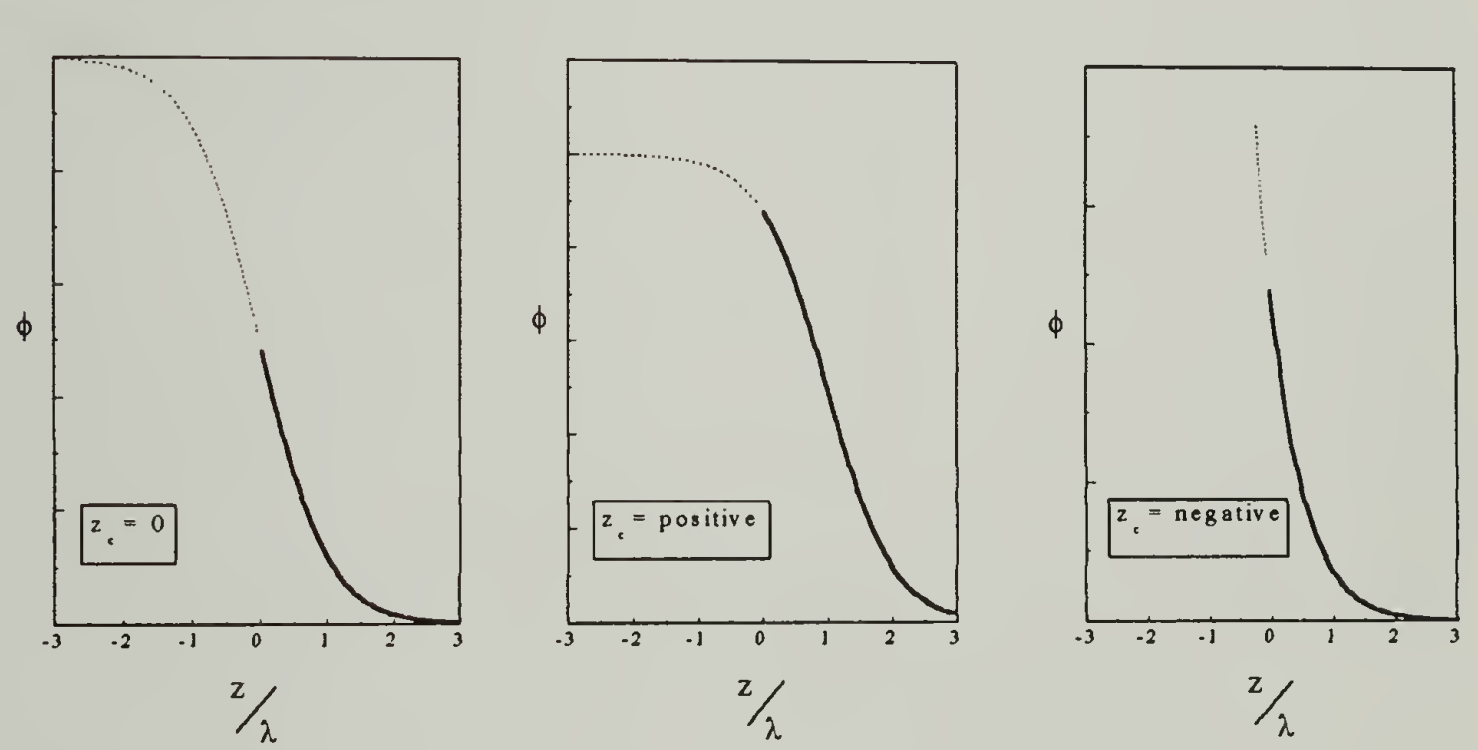


Figure A.1 Relationship between the parameter $z_c$ and the shape of the volume fraction profile for the PSCOOH samples. Only the positive values of z are used in the fitting procedure.

Except for H81C, all of the data sets could also be suitably explained using the parabolic form, albeit with more "rounding" at the tail. For example, H14C needs needs to be convoluted with a Gaussian ~ 3 times as wide as D14C for reasonable agreement between calculated and observed data sets. Figure A.2 shows a comparison of the $\rho_n$ profiles of which best explain the observed NR for H14C in d-cyclohexane ($\chi^2 \approx 2.2$ for each form).

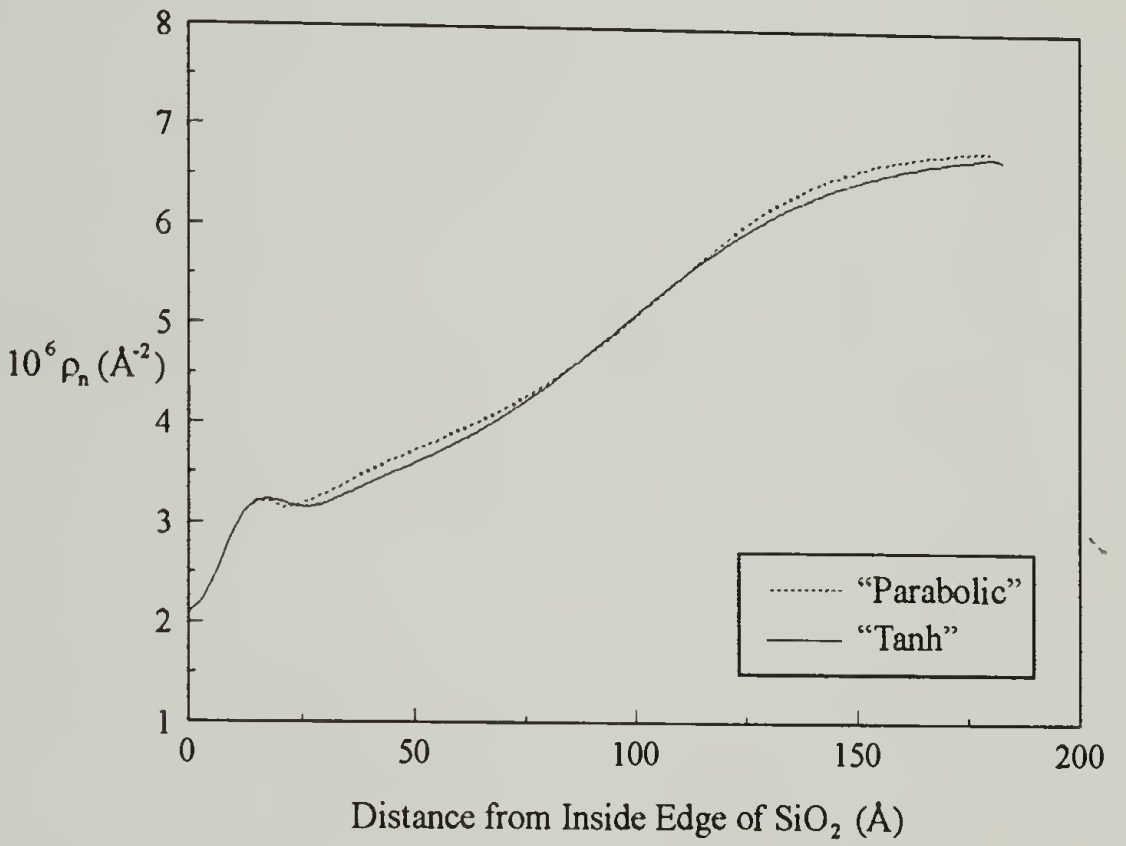


Figure A.2 Comparison of the parabolic and tanh profiles which best explain the observed NR for H14C in d-cyclohexane. Note the coincidence of these curves at the regions of largest $\frac{d\rho_n}{dz}$ ($z \approx 10$Å and $z \approx 110$Å).

Inspection of Figure A.2 is a good demonstration of the importance of the choice of functional form. While more than one functional form can explain the observed NR satisfactorily, there are serious restrictions on the overall shape and size of the $\rho_n$ profile. One of our criteria for successful modeling of the NR data is that the final overall $\rho_n$ profile can be approached using more than one function. The $\rho_n$ profiles in Figure A.2 satisfy this criterion within experimental error.

NR experiments are most sensitive to features of the concentation profile having large $\frac{d\rho_n}{dz}$ (for example, at the solution solid interface) and least sensitive to regions having small $\frac{d\rho_n}{dz}$ (for example, at the intermediate z values of the H81C sample, where $\rho_n$.is either a "plateau" or a slowly varying function of z). Therefore, NR is at its best in the observation of $\phi_1$ values (at the solution solid interface) and at its worst in the intermediate regions of the PSCOOH brush. No experimental techinque has to date produced more reliable in-situ measurements of L or $\phi_1$.

# BIBLIOGRAPHY


Aharoni, S.M. *Macromolecules* **16** 1722 (1983).

Alexander, S. *J. Phys. (Paris)* **38** 983 (1977).

Allara, D.L., Z. Wang, and C.G. Pantano *Journal of Non-Crystalline Solids* **120** 93 (1990).

Anastasiadis, S.H., T.P. Russell, S.K. Staija, and C.F. Majkrzak, *J. Chem. Phys.* **92** 5677 (1990).

Auroy, P. ,L. Auvray, and L. Léger Phys. Rev. Lett. 66 719 (1991).

Bates, F.S., G.D. Wignall, *Phys. Rev. Lett.* **57**, 1429 (1986).

Bates, F.S., G.D. Wignall, W.C. Kohler, *Phys. Rev. Lett.* **55**, 2425 (1985).

Benninghoven, A., F.G. Rudenaur, H.W. Werner, *Secondary Ion Mass Spectroscopy, Chemical Analysis Series*; John Wiley: New York, 1987; Vol.86.

Born, M., E. Wolf *Principles of Optics*, 6th edition, Pergamon Press, Oxford, 1980.

ten Brinke, G., F.E. Karasz, W.J. MacKnight, *Macromolecules,* **16,** 1827 (1983).

Broseta, D., G.H. Fredrickson, E. Helfand, and L. Leibler *Macromolecules* **23** 132 (1990).

Brown, H. R. *Journal of Materials Science* **25** 2791 (1990).

Chaturvedi, U.K., et.al. *Phys. Rev. Lett.* **63**(6) 616-619 (1989).

Chu, W.K. ,J.W. Mayer, M.A. Nicolet, *Backscattering Spectrometry*; Academic Press, NY, 1978.

Composto, R.J. and E.J. Kramer, *J. of Materials Science* **26** 2815 (1991).

Composto, R.J, E.J. Kramer, and D.M. White; *Macromolecules* **21** 2580-2588 (1988).

Composto, R.J, R.S. Stein, E.J. Kramer, R.A.L. Jones, A. Mansour, A. Karim, and G.P. Felcher, *Physica B,* **156 & 157,** 434 (1989).

Cosgrove, T,. T Heath, B. van Lent, F. Leermakers, and J. Scheutjens *Macromolecules* **20** 1692 (1987).

Cowie, J.M.G., and D. Lath, *Makromolecular Chemie Macromolecular Symposium,* **16,** 103 (1988).C. Creton and E.J. Kramer *Macromolecules* **24** 1846 (1991).

Doi, M., S.F. Edwards, *The Theory of Polymer Dynamics*, Clarendon Press, Oxford, 1986.

Dolan, A.K. and S.F. Edwards *Proc. R. Soc. London* **A343** 427 (1975).

Fayt, R., P. Hadjiandreou, P.H. Teyssie *J. Polym. Sci. Polym. Chem. Ed.* **23** 337 (1985).

Feldman, L.C. and J.W. Mayer, *Fundamentals of Surface and Thin Film Analysis*, Elsevier Science, NY,1986.

Fernandez, M.L., J.S. Higgins, J. Penfold, R.C. Ward, C. Shackleton and D. Walsh, *Polymer* **29** 1923 (1988).

Flory, P.J. *Principles of Polymer Chemistry* Cornell University Press, Ithica, NY 1953.

Frantz, P., D.C. Leonhardt, and S. Granick *Macromolecules* **24** 1868 (1991).

de Gennes, P.–G., *J. Chem Phys.* **55**, 572 (1971).

de Gennes, P.–G., *J. Phys. (Paris)* **37** 1445 (1976); *Macromolecules* **13** 1069 (1980).

de Gennes, P.–G., *Scaling Concepts in Polymer Physics* Cornell University Press, Ithica, NY 1979.

Graessley, W.W., *Adv. Polym. Sci.* **16**, 1 (1974).

Granick, S., *Macromolecules* **23** 4344 (1990).

Green, P.F., et.al.*Macromolecules* **18** 501 (1985).

Green, P.F., B.L. Doyle, *Macromolecules* **20** 2471-74.

Green, P.F., B.L. Doyle, *Phys. Rev. Lett.* **57** 2407-10.

Halperin, A. *J. Phys. (Paris)* **49** 547 (1988).

Halperin, A., M. Tirrell, and T.P. Lodge *Adv. Polym. Sci.* **100** 31 (1992).

Helfand, E. and A.M. Sapse *J. Chem. Phys.* **62** 1327 (1975).

Helfand, E. and Y. Tagami *J. Chem. Phys.* **56** 3592 (1971).

Helfand, E., and Y. Tagami *J. Polym. Sci. Part B* **9** 741 (1971).

Hirtz, S. J. M.S. Thesis University of Minnesota (1986).

Iyengar, D.R. and T.J. McCarthy *Macromolecules* **23** 4344 (1990).

Jones, R.A.L., E.J. Kramer, M.H. Rafailovich, J. Sokolov, and S.A. Schwartz, *Physical Review Letters,* **62**(3), 280 (1989).

Kausch, H.H. and M. Tirrell, *Annu. Rev. Mater. Sci.* **19**, 341-377 (1989).

Kawaguchi, M., and A. Takahashi *Adv. Colloid Int. Sci.* **37** 219 (1992).

Klein, J. *Nature* **288** 248 (1980).

Klein, J. and B.J. Briscoe, *Proc. R. Soc. Lond.* **365**, 53 (1979).

Mark, J., Encyclopedia of Polymer Science Vol. 16 (1985).

Milner, S.T. *Science* **251** 905 (1991).

Milner, S.T., T.A. Witten, M.E. Cates *Europhysics Letters* **5**(5) 413 (1988).

Milner, S.T., T.A. Witten, M.E. Cates *Macromolecules* **21** 2610 (1988).

Molau, G.E. *Polymer Letters,* **3,** 1007 (1965).

Motschmann, H., M. Stamm, and Ch. Toprakcioglu *Macromolecules* **24** 3681 (1991).

Odian, G. *Principles of Polymerization*, 2nd edition, Wiley Interscience, New York, 1981.

Pandit, R., M. Schick, M. Wortis *Phys. Rev. B* **26** 5112 (1982).

Press, W.H., B.P. Flannery, S.A. Teukolsky, and W. J. Vetterling, *Numerical Recipes* Cambridge: Cambridge University Press, 1986.

Price, F.P., P.T. Gilmore, E.L. Thomas, R.L. Laurence *J. Polym. Sci. Polym. Symp.* **63**, 33-44 (1978).

Quirk, R.P. *Macromolecules* **22** 85 (1989).

Rafailovich, M.H., J. Sokolov, X. Zhao, R.A.L. Jones, E.J. Kramer, *Hyperfine Interactions* **62**, 45-53 (1990).

Russell, T.P. *Materials Science Reports* **5**(4) 171-271 (1990).

Schmid, I. and K. Binder, *Journal of Physics (Paris),* **46,** 1631 (1985).

Shewmon, P.G. *Diffusion in Solids*; McGraw Hill, 1963.

Shull, K. *Physics of Polymer Surfaces and Interfaces*; ed. I. Sanchez, Butterworth-Heinimann and Manning, 1992.

Steiner, U. et.al. *Makromol. Chem. Macromol. Symp.* **45** 283-288 (1991).

Strazielle, C. and H. Benoit *Macromolecules* **8** 203 (1975).

Taunton, H.J., C. Toprakcioglu, L.J. Fetters, and J. Klein *Nature* **332** (21) 712 (1988).

Turos, B. et.al. *A. Nucl. Inst. Meth.* B4, **92** (1984).

Whitlow, S.J., R.P. Wool, *Macromolecules.* **22** 2648-2652 (1989).

Whitmore, M.D. and J. Noolandi *Macromolecules* **23** 3321 (1990).

Wijmans, C.M., J.M.H.M. Scheutjens, and E.B. Zhulina *Macromolecules* **25** 2657 (1992).

Ye, M. Ph.D. thesis, Univ. of Massachusetts (1990).

Ye, M,. R.S. Stein, R.J. Composto *Macromolecules* **23** 1990.

Young, L.J. *Copolymerization Reactivity Ratios* in Chapter 2 in *Polymer Handbook* J. Brandrup and E.H. Immergut with W. McDowell, Eds. Wiley Interscience, NY, 1975.